Development of Highly Anti-Corrosive and Mechanically Improved Graphene-Based Polyurethane Nanocomposites for the Application of Pipeliners in Oil Sands Transportation

by

Jun Geun Um

A thesis

presented to the University of Waterloo

in fulfillment of the

thesis requirement for the degree of

Doctor of Philosophy

in

Chemical Engineering

Waterloo, Ontario, Canada, 2020

EXAMINING COMMITTEE MEMBERSHIP

The following served on the Examining Committee for this thesis. The decision of the Examining Committee is by majority vote.

External Examiner	Dr. Patrick Lee Assistance Professor
Supervisor(s)	Dr. Aiping Yu Associate Professor
Internal Member	Dr. Christine Moresoli Professor
Internal Member	Dr. Ali Elkamel Professor
Internal-external Member	Dr. Giovanni (John) Montesano Assistance Professor

AUTHOR'S DECLARATION

This thesis consists of material all of which I authored or co-authored: see Statement of Contributions included in the thesis. This is a true copy of the thesis, including any required final revisions, as accepted by my examiners.

I understand that my thesis may be made electronically available to the public.

STATEMENT OF CONTRIBUTIONS

This thesis is based on a combination of published work. Chapters are adapted from the following list of published work, with specific reference to the published work provided within the chapter.

Jun Geun Um, Yun-Seok Jun, Hesham Alhumade, Hariharan Krithivasan, Gregory Lui and Aiping Yu. “Investigation of the size effect of graphene nanoplatelets (GnPs) on the anti-corrosion performance of polyurethane/GnP composites”, *RSC Advances*, 2018, **8**, 17091–17100.

> I designed and carried out the experiments. Yun-Seok Jun, Hesham Alhumade, and Hariharan Krithivasan helped analyzed the data. Gregory Lui and Aiping Yu reviewed the manuscript.

Jun Geun Um, Yun-Seok Jun, Ali Elkamel, and Aiping Yu. “Engineering investigation for the size effect of graphene oxide derived from graphene nanoplatelets in polyurethane composites”, *The Canadian Journal of Chemical Engineering*, 2020, **1**, 1-13.

> I synthesized the materials and carried out the experiments. Yun-Seok Jun helped analyzed the data. Ali Elkamel, and Aiping Yu reviewed the manuscript.

Jun Geun Um, Saeed Habibpour, Yun-Seok Jun, Ali Elkamel, and Aiping Yu. “Development of π- π Interaction-induced Functionalized Graphene Oxide on Mechanical and Anticorrosive Properties of Reinforced Polyurethane Nanocomposites”, *ACS Industrial & Engineering Chemistry Research*, In press (DOI: 10.1021/acs.iecr.9b06755), 2020.

> I synthesized the materials and carried out the experiments. Saeed Habibpour and Yun-Seok Jun helped analyzed the data. Ali Elkamel, and Aiping Yu reviewed the manuscript.

ABSTRACT

In contemporary composite science, polymer nanocomposites are the promising functional materials in the research field. Among them, the nano-sized filler, graphene, supplements the flaws of polymeric materials with their exclusive mechanical, electrical, and gas barrier properties. Recently, the exceptional corrosion resistance of polymer/graphene nanocomposites provides high efficiency for metal surface protection. In particular, the metal pipes for the transportation of oil and gas are very vulnerable to corrosion in the industries. The protection layer of polymer/graphene nanocomposites effectively mitigates the corrosion on the metal pipe due to the plate-like structure of graphene impeding the diffusion of corrosive agents through the polymer matrix.

In this thesis, polyurethane (PU) nanocomposites incorporated with graphene were considered as the protective coating layer of pipeliners in oil sands transportation. Pipeliner is an essential segment for oil sands transportation, and PU is generally used for the pipeliners to protect pipe inside against corrosive oil sands slurry. However, there has been a need for the improvement of the anti-corrosion performance and mechanical properties of PU. This is because these properties are correlated to the management cost in oil and gas industries. At this point, PU/graphene nanocomposites enable a longer lifetime of pipeliners and higher transport rates of oil sands due to the excellent physical properties of graphene. In addition, graphene nanoplatelets (GnP), which means multiple-layer graphene, were used as fillers for more practical research. GnP is commercialized in the market and provides various size for the polymer nanocomposites. Therefore, three phases were conducted in this thesis for the development of the protective coating layer based on PU/GnP nanocomposites: (I) size effect of GnP in the PU nanocomposites on

mechanical and corrosion properties, (II) comparison of GnP and GO in the PU nanocomposites on mechanical and corrosion properties, and (III) effect of chemically functionalized graphene oxide (f-GO) in the PU nanocomposites on mechanical and corrosion properties.

In the first phase, the size effect of GnP influencing filler dispersion within the PU matrix was thoroughly investigated. 4 different sizes of GnP, specifically average diameter, were used for the first phase. They showed an average diameter from 100 μm to under 2 μm and were sufficient to compare their size. This study demonstrated that the GnP, with a small diameter significantly improved the anti-corrosion performance of the PU nanocomposites. Protection efficiency (P_{EF}), which is a parameter to quantify anti-corrosion performance, was increased up to 99.6 % by the PU nanocomposites with the small GnP from 97.5 % of the neat PU. This is because the small GnP indicated a more uniform dispersion within the PU matrix than other GnP. The uniform dispersion of the small GnP formed a complicated pathway in the PU/GnP nanocomposites to suppress the diffusion of corrosive agents. However, the small GnP was not effective to improve mechanical properties of PU nanocomposites. The interfacial adhesion between GnP and the PU matrix was insufficient to distribute external stresses to the composite inside. On the other hand, large GnP indicated to the improvement of tensile modulus of the PU nanocomposites. The high aspect ratio of the large GnP contributed to the improvement of the tensile modulus, which means elastic deformation in a small range of strain. In consequence, the size of GnP was a critical factor influencing the dispersion of GnP and the anti-corrosion performance of PU/GnP nanocomposites. However, the interfacial adhesion between GnP and the PU matrix needs to be improved to enhance mechanical properties.

In the second phase, GO was synthesized from GnP of the phase 1 to improve the interfacial adhesion between GnP and the PU matrix. GO has various hydrophilic functional groups, such as

hydroxyl (-OH), carbonyl (-C=O), and epoxy (-C-O-C-) groups. These functional groups could lead to the exfoliation (ie. delamination) of graphene layers and the formation of physical bonding with the PU matrix, such as hydrogen bonding. These effects contributed to the improvement of both mechanical properties and anti-corrosion in the PU/GO nanocomposites. However, GO was thermally more unstable than GnP due to the decomposition of the hydrophilic functional groups. Tensile modulus and hardness of PU/GO were increased up to 53 % and 40 % with the neat PU. In addition, PU/GO indicated 99.9 % of P_{EF} while the neat PU indicated 98.9 % of P_{EF}. In this study, large GO provided better mechanical properties and anti-corrosion in comparison to small GO in the PU nanocomposites. This result was attributed to formation of the hard-segment in the PU/GO nanocomposites. PU consists of the hard and soft segments and elasticity or hardness of PU depend on the size or amount of the hard segment. The hydrophilic functional groups on GO provides a nucleation site for the formation of the hard-segment. Thus, extremely high nucleation sites of the small GO resulted in a decrease of the hard-segment size. As a result, the hard segment size was not sufficient in the PU nanocomposites containing the small GO for appropriate mechanical properties Consequently, it was found that GO with large size eminently improved both mechanical and anti-corrosion properties of PU/GO. However, the thermal stability of GO needs to be improved for the pipeliner application because the oil sands slurry is hot (~80 °C).

In the third phase, f-GO was synthesized from GO of phase 2 using amine groups to improve the thermal stability of GO, maintaining high interfacial interaction among the PU matrix and fillers. Two different aliphatic amine groups (docecyl (DA) and *tert*-butyl amine groups(tBA)) and one aromatic group (2-naphthyl amine group (2NA)) were used to functionalize GO. DA and tBA groups were investigated for interaction with the polyol part of PU while the 2NA was for the one with the isocyanate part of PU. f-GO indicated higher thermal stability than GO because the amine

functional groups have stronger bonding with GO than the hydrophilic functional groups on GO. Among the PU/f-GO nanocomposites, PU/2NA-GO indicated the most improved mechanical properties and anti-corrosion performance. PU/2NA-GO showed 123 % and 49 % improvements in tensile modulus and hardness, respectively than the neat PU. P_{EF} of PU/2NA-GO was improved up to 99.9 % from 86.9 % of the neat PU. This improvement of PU/2NA-GO was attributed to π-π interaction between the PU matrix and 2NA, inducing overlapped aromatic groups, such as the 2NA and phenyl groups of isocyanate. It led to a synergetic effect on mechanical properties and anti-corrosion of the nanocomposite. In consequence, this study revealed that the aromatic component on GO led to π-π interaction with the PU matrix. This interaction contributed to both improvements in mechanical properties and anti-corrosion performance.

In conclusion, the results from the 3 phases have shown critical factors to design mechanically improved and highly anti-corrosive PU/GnP nanocomposites. GnP size was very important to decide the dispersion of the fillers. Functional groups on GO were crucial to improve the interfacial interaction between the PU matrix and graphene fillers. As a result, aromatic group, which is covalently bonded with f-GO, indicated the best performance in the PU nanocomposites due to π-π interaction. These studies in this thesis can be suitable for oil and gas industries. In particular, they can provide a practical insight into the development of PU pipeliners for the transportation of oil sand slurry.

ACKNOWLEDGEMENTS

First, I would like to thank my supervisor, Professor Aiping Yu, for providing me with an opportunity to carry out this study. She has always motivated me with consistent support and encouragements throughout my graduate studies. I also thank the Natural Sciences and Engineering Research Council of Canada (NSERC) and Ontario government for Ontario Early Research Award Program for providing financial support.

I would also like to thank my Ph.D. thesis examining committee, including Professor Christine Moresoli, Professor Ali Elkamel, and Professor Giovanni (John) Montesano from the University of Waterloo, and Professor Patrick Lee from the University of Toronto as my external examiner for their time and contributions during this important process.

I also would like to acknowledge my friends in Waterloo for their friendship and encouragement. Special thanks goes to Sung-Ho Park, Moon-Gyu Park, Se-Young Kim, Youngwook Kim and Yun-Seok Jun. Without them, my graduate studies in Waterloo would have not been enjoyable.

I deeply thank my wife, Myungok Park, for supporting and encouraging me over the program of my Ph.D. Her unconditional love and sacrifice made all of this possible. I would like to devote this thesis to her. I also thank my son, Hakseo, and my daughter, Yueun, who make my family enjoyable.

Lastly, my genuine gratitude goes to my parents without whom I would never have enjoyed so many opportunities. I also thank my parents-in-law for supporting me and letting their precious daughter begin a journey with me in Canada.

DEDICATION

This thesis is dedicated to beloved my family, Myungok Park, Hakseo Um,

and Yueun Um

my parents Jooheon Um, and Jinyang Lee

my siblings Hyowon Um, and Jungsik Um

my parents-in-law, Jangwoo Park and Hyunsook Choe

my brother-in-law Chunyong Park

TABLE OF CONTENTS

LIST OF FIGURES

LIST OF TABLES

LIST OF ABBREVIATIONS

2NA	2-Naphthylamine
AC	Alternating current
BP	Boiling point
CNT	Carbon nanotube
CV	Cyclic voltammetry
CVD	Chemical vapor deposition
DA	Dodecylamine
DC	Direct current
DMF	Dimethylformamide
DSC	Differential scanning calorimetry
EIS	Electrochemical impedance spectroscopy
FT-IR	Fourier-transform infrared
FWHM	Full width at half maximum
GnP	Graphene nanoplatelets
GO	Graphene oxide
HDI	Hexamethylene diisocyanate
MDI	Methylene diphenyl diisocyanate
MP	Melting point
MWCNT	Multi-walled carbon nanotubes
PCM	Planetary centrifugal mixer
PET	Polyethylene terephthalate

PMMA	Polymethyl methacrylate
PU	Polyurethane
PUE	Polyurethane elastomer
PVA	Polyvinyl alcohol
RGO	Reduced graphene oxide
SEM	Scanning electron microscope
tBA	tert-Butylamine
TEM	Transmission electron microscope
THF	Tetrahydrofuran
TGA	Thermo-gravimetric analysis
TPU	Thermoplastic polyurethane
UTM	Universal testing machine
XRD	X-ray diffraction

LIST OF SYMBOLS

A	Area
Å	Angstrom
b_a	Slope of anodic linear curve
b_c	Slope of cathodic linear curve
°C	Degree Celsius
C_{dl}	Double-layer capacitance
CPE	Constant phase element
E	Equivalent weight
E_{corr}	Corrosion potential
EW	Equivalent weight
I	Current
I_{corr}	Corrosion current
I_D	Intensity of D band
I_G	Intensity of G band
L_c	Crystallite size
L_a	Inter-defect distance
P_{EF}	Protection efficiency
R_{corr}	Corrosion rate
R_{ct}	Charge transfer resistance
R_p	Polarization resistance
R_s	Solution resistance

t	Sample thickness
T_m	Melting point
V	Voltage
W	Warburg diffusion
wt%	Weight fraction
Z’	Real impedance
Z”	Imaginary impedance
β	Full width at half maximum
θ	Diffraction angle
λ	Wavelength
ρ	Density
ω	Angular frequency

1. Introduction

1.1 Background

Polymer nanocomposites (PNCs) are generally defined as a polymer or copolymer including nanoparticles or nanofillers dispersed within the polymer matrix.[1] Since the first commercial PNC was invented by Toyota Group, the development of PNCs has been accelerated in material science.[2] Toyota invented a nylon 6/clay nanocomposite for the application of a timing belt cover in a car engine. Toyota applied the highly exfoliated clay structure with uniform dispersion in the nylon 6 matrix.[3] The nano-sized clay led to a thermally stable and mechanically reinforced effect in the nanocomposite. This nanocomposite was described as “Organic-Inorganic Hybrid” due to the nano-sized dispersed filler. It showed many potential applications to researchers in automotive, construction, and electronic areas.[2, 3] Initial studies for PNC had focused on the exfoliation of the layered fillers and modification of its surface compatible with a polymer matrix. Exfoliation means separating the layered fillers into an individual layer to maximize the surface area of the fillers.[4] Various polymers have been studied to fabricate the hybrid with the layered silicate fillers and several successful results have been reported.[4, 5] Recently, the electrical and thermal properties of nanocomposites are considered as critical factors to develop electronic devices.[6] Thus, carbon-based nanofillers, such as carbon nanotube (CNT), graphene, and multi-layered graphene, have been introduced to substitute the previous nanocomposites.[5, 6] Among the carbon-based fillers, graphene has been highly attracted to researchers because of its unique properties.

Graphene, a single sheet exfoliated from graphite, has shown a practical utility in polymer/graphene nanocomposites, especially for the application of electrical devices.[7] The

utility is feasible due to the multi-functional properties of graphene, such as exceptional mechanical, electrical, thermal, and gas barrier properties. For this reason, graphene has been attributed to the dramatic improvement in the inherent properties of polymers as a form of a nanocomposite.[8, 9] However, there are several challenges to maximize the performance of polymer/graphene nanocomposites. First, graphene needs to be exfoliated and dispersed uniformly within the polymer matrix. This challenge has been a critical issue for this research as same as polymer/clay nanocomposites. Graphene layers are strongly stacked by van der Waals force.[10] It is even very difficult to separate a single graphene layer and disperse it into the polymer matrix.[10] Second challenge is surface modification of graphene to be compatible with a polymer matrix. It is another crucial factor to design the polymer/graphene nanocomposites. This factor is directly associated with physical properties of the nanocomposites.[11] Thus, many researchers have focused on those two factors in terms of fabrication for the composites.[12]

Several approaches have been considered to produce the single layer of the graphene, such as chemical vapor deposition (CVD), epitaxial growth, and chemical oxidation of graphite.[13] The CVD is highly effective in gaining a single layer of the graphene. However, the CVD cannot produce a large amount of graphene at one time because the CVD is based on a gas-phase reaction. Single or few layers of graphene is formed on a substrate (e.g. copper) by this method.[14] Then, the graphene products are obtained by the separation from the substrate. For this reason, the production of a large amount of graphene through the CVD requires a huge reactor or numerous reactions.[14] Thus, this method is commonly used for a laboratory purpose but is not useful to a practical application.[13] Graphene oxide (GO) obtained from the chemical oxidation of graphite is the most practical method to produce the exfoliated graphene. This method can provide not only a large quantity of GO after the oxidation reaction but also hydrophilic functional groups such as

hydroxyl (-OH), epoxy (C-O-C), and carboxyl (-C=O) groups on the GO surface.[15] Besides, the hydrophilic functional groups on the GO surface can react with other functional groups (e.g. amine or isocyanate), and it enables the GO surface to be more compatible with a certain polymer matrix. Successful examples about the polymer/graphene nanocomposites are shown in Table 1.1.

Table 1.1. Successful examples about polymer/graphene nanocomposites[16-21]

Polymer	**Graphene filler**	**Fabrication**	**Improvement**
Polyvinylalcohol (PVA)	Graphite oxide	Solution casting	Mechanical properties Gas barrier properties
Polymethylmethacrylate (PMMA)	Reduced Graphite oxide	In situ polymerization	Electrical conductivity Thermal stability
Polyurethane (PU)	Graphite oxide	In situ polymerization	Mechanical properties Thermal stability
Polyurethane (PU)	Functionalized Graphite oxide	Solution casting	Dielectric properties Elasticity
Polyisobutylene (PIB)	Reduced Graphite oxide	Solution casting	Dielectric properties Gas barrier properties
Epoxy	Graphene nanoplatelets	Photopolymerization	Stiffness Surface hardness

In recent years, polymer/graphene nanocomposites have expanded their application to anti-corrosive coating for the protection of a metal substrate.[22] Corrosion is the most important and practical challenge in modern industries, particularly for oil and gas.[23] These industries have heavily considered this issue to protect a metal part from a strong corrosive environment.[24] For this reason, a strong and anti-corrosive polymer is generally used as a protective layer to mitigate corrosion.[25] However, the oil and gas industries have required the development of a more physically improved and higher anti-corrosive protective layer than the conventional layers. This

is because these improvements are associated with cost-effectiveness and maintenance of the protective layer.[26] In this situation, graphene nanoplatelets (GnP) can contribute to improving anti-corrosive performance and mechanical properties as a form of polymer nanocomposites. This is due to the fact that the two-dimensional graphene structure prevents the permeation of the corrosive agent through the polymer matrix.[27] Besides, GnP is highly resistant to an electrochemical reaction. (e.g. corrosion). Thus, GnP can provide a stable molecular barrier to suppress the diffusion of the corrosive agent, which includes an ion.[28] Based on these facts, graphene effectively protects a metal surface in the form of a polymer nanocomposite under a harsh corrosive condition.

In summary, graphene materials have emerged as the new nanofiller in the field of polymer nanocomposites based on their exceptional physical and chemical properties. Multi-layered graphene such as GnP is also useful to the application of the composites in terms of processing and cost. Various combinations of polymer/graphene or GnP nanocomposites have been studied, and their reinforcing effect has also been proven by the studies. Especially, the polymer/GnP nanocomposites can be effective in the application of metal protection due to its structural advantage and electrochemical stability. Thus, the polymer/GnP nanocomposites are highly suitable for the application of pipeliners in oil sands transportation. However, further exfoliation and surface modification of GnP are required to maximize mechanical and anti-corrosion properties of the nanocomposites. These facts are critical in the view of management and cost in oil and gas industries. Therefore, recent researches on polymer nanocomposites incorporated with graphene or GnP have been focused on these issues.

1.2 Study objectives and approach

The objective of this research is to develop highly anti-corrosive and mechanically improved polyurethane (PU) nanocomposites with various graphene nanoplatelets (GnP) and derived graphene oxide (GO) for the application of PU pipeliners in oil sands transportation. PU is typically used as the material for pipeliners due to its excellent physical properties. However, PU pipeliners are needed to further improve both mechanical and anti-corrosion properties in terms of cost-effectiveness and management. For practical research, the commercial PU was incorporated with GnP or GO to fabricate nanocomposites. Anti-corrosion performance and mechanical properties of the PU nanocomposites were mainly investigated to prove the performance as pipeliners. The study for these PU nanocomposites was conducted by three phases: (Phase I) the size effect of GnP in the PU nanocomposites on mechanical and anti-corrosion properties, (Phase II) the effect of GO in the PU nanocomposites on mechanical and anti-corrosion properties in comparison with GnP, and (Phase III) the effect of chemically functionalized GO (f-GO) in the PU nanocomposites on mechanical and anti-corrosion properties. The flowchart of this study is described in the Figure 1.1.

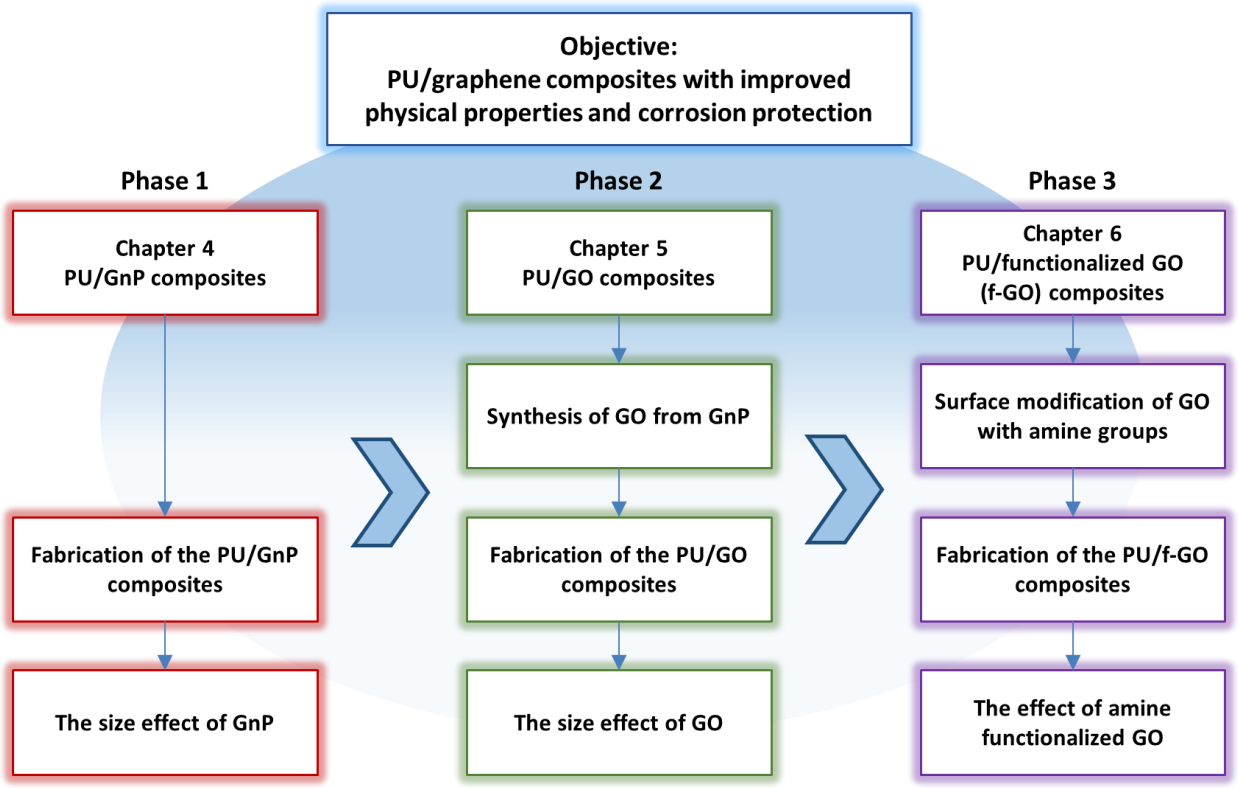

Figure 1.1. Flowchart of the studies in this thesis.

In phase 1, the main objective is to understand the correlation between the size of GnP and their dispersion in the PU matrix. In this study, 4 different types of commercial GnP were used as fillers. They have different average diameters from under 2 μm to 100 μm. In particular, the smallest size of GnP available in the market was under 2 μm in diameter while the largest one was 100um. Size differences of 4 GnP in this range were suitable to compare the size effect of GnP in the PU nanocomposites. Anti-corrosion performance and mechanical properties were investigated by the size of GnP in nanocomposites. Specifically, the PU/GnP nanocomposites were fabricated via planetary centrifugal mixing (PCM). The PU consists of resin and hardener containing methylene diphenyl diisocyanate (MDI) and polyol, respectively. The mixing ratio of MDI and polyol was 25 and 100 by weight. The PU/GnP nanocomposites were cast as a film (thickness: 300μm) on two

substrates, such as copper and polyethylene terephthalate (PET) plates. The copper plate with the cast film was used for corrosion properties, while the mechanical properties were measured by the cast film separated from a PET plate. Subsequently, the scanning electron microscope (SEM) was used to verify the size difference of the 4 GnP. X-ray diffraction (XRD) was used to analyze the structure of the 4 GnP. SEM was also used to observe the dispersion of the 4 GnP within the PU matrix. Lastly, a model for corrosion protection with the appropriate size of GnP in PU nanocomposites was established to account for the corrosion mitigation mechanism.

In the phase 2, the main goal is to investigate the effect of GO, which influences the dispersion of fillers and interfacial interaction between fillers and the PU matrix. For this study, 2 different sizes of GO were synthesized from the 2 GnP of phase 1 by modified Hummer's method. Functional groups and graphene structure of GO were investigated in comparison with GnP. Tetrahydrofuran (THF) was used to disperse GO, and then the PU matrix was mixed with GO. The PU/GO nanocomposites were cast on the same 2 substrates of phase 1. Fourier-transform infrared (FT-IR) spectroscopy was used to detect the hydrophilic functional groups on GO. Thermogravimetric analysis (TGA) was used to compare the thermal stabilities of GnP and GO. SEM was used to observe the morphologies of GO and their PU nanocomposites. The mechanical and anti-corrosion properties of the PU/GO nanocomposites were thoroughly investigated. In addition, the size effect of GO was also investigated on the same properties.

In the phase 3, the main objective is to synthesize more thermally stable f-GO than GO and investigate the effect of f-GO, which influences filler dispersion and interfacial interaction with the PU matrix by the type of f-GO. In this study, three different types of amine functional groups were used to functionalize GO. Docecyl amine (DA) and *tert*-butyl amine (tBA) were used to provide aliphatic chain on GO. 2-naphthyl amine (2NA) were used to provide aromatic group on

GO. According to several studies about f-GO, aliphatic and aromatic groups on f-GO contributed to mechanical properties of the PU nanocomposites.[29-32] However, the results from those two groups have not been compared. DA group was designed to form a chain entanglement with the PU matrix due to its long aliphatic chain. Short but branched aliphatic form of tBA group was expected to infiltrate more into the graphene interlayers than other groups. The aromatic group of 2NA was designed to form an interaction with the phenyl groups in the PU matrix. Specifically, f-GO was synthesized via chlorinated GO (Cl-GO) to promote the chemical reaction between amine groups and Cl-GO. The PU/f-GO nanocomposites were also fabricated by using THF, which is the same method illustrated in phase 2. FT-IR spectroscopy was used to prove the amine functionalization of f-GO. TGA was used to compare thermal stabilities of f-GO and GO. Morphologies of the 3 f-GO and PU/f-GO nanocomposites were observed using SEM. Mechanical and anti-corrosion properties of the nanocomposites were also investigated.

1.3 Thesis outline

This thesis consists of eight chapters organized as follows:

- Chapter 1 provides background information on this research, study objectives, and an outline of the thesis.
- Chapter 2 provides review of the characteristics of graphene fillers for the application of polymer nanocomposites, processing techniques employed in the thesis, and corrosion protection application.
- Chapter 3 describes characterization techniques for the materials deployed in this thesis, including physicochemical characterizations, determination of mechanical properties, and measurement of electrochemical corrosion testing.
- Chapter 4 presents the fabrication of polyurethane nanocomposites incorporated with four different sizes of graphene nanoplatelates (GnP). The impacts of GnP size on the anti-corrosion performance and mechanical properties of the nanocomposites are thoroughly investigated.
- Chapter 5 discusses the effect of GO in comparison with GnP in the PU nanocomposites on mechanical properties and anti-corrosion performance. The size effect of GO in the PU nanocomposites is also investigated.
- Chapter 6 describes chemically functionalized GO and their PU nanocomposites. Anti-corrosion performance and mechanical properties of the PU/f-GO nanocomposites are studied by the 3 different amine groups. Available interfacial interaction between f-GO and the PU matrix is also investigated.
- Chapter 7 presents the overall conclusions drawn from Chapter 4 to 6 and the recommendations for the follow-up study on practical application of the nanocomposites.

2. Literature Review

2.1 Polymer graphene nanocomposites

Based on the study of polymer nanocomposites, graphene has been positioned as a next important resource to utilize nanofillers, such as carbon nanotubes (CNT). Polymers can combine with graphene to enhance intrinsic properties; electrical, mechanical, and barrier in particular.[33] These improvements can even be achieved by a little amount of graphene due to its inherent properties, such as high surface area and superior physical properties. Graphene can also modify or functionalize its surface with different chemical groups to produce a high compatibility with various polymer matrices.[6] Nevertheless, graphene should be further exfoliated and dispersed uniformly within the polymer matrices to maximize the performance of the composites. In practice, graphene interlayers are stacked by van der Waals force, rendering the research of polymer/graphene composites as the challenging work.[8] Recently, multilayer graphene, such as graphene nanoplatelets (GnP), has received much attention in terms of a practical application of graphene to overcome this problem.[34, 35] In this thesis, GnP, its derived GO, and chemically functionalized GO were employed as main fillers, while polyurethane (PU) was used as the polymer matrix for the composites.

2.1.1 Graphene fillers

2.1.1.1 Graphene and graphene nanoplatelets

As explained in numerous literature, graphene is a single sheet consisting of carbon atoms as a form of a two-dimensional (2D) honeycomb structure which is considered to be the thinnest material in the world.[13] In general, various carbon materials can be derived from graphene as

described in Figure 2.1. The zero-dimensional (0D) fullerenes, one-dimensional (1D) CNT, and three-dimensional (3D) graphite can be formed by wrapping, rolling, and stacking 2D graphene, respectively.[36] Besides, researches have been attracted by exceptional physical properties of graphene; high Young's modulus of 1 TPa (100 times higher than steel), the high thermal conductivity of 5000 W/(m·K), and an electrical conductivity up to ~6000 S/cm.[37] In addition, graphene can provide excellent gas barrier property as a form of coating and polymer composite due to its plate-like structure and high surface area up to ~2630 m^2/g.[38] Based on these superior properties, graphene has been considered as an ideal material for polymer nanocomposites. Thus, a number of engineers and scientists have imagined that graphene can provide a multidisciplinary platform in the field of composites.

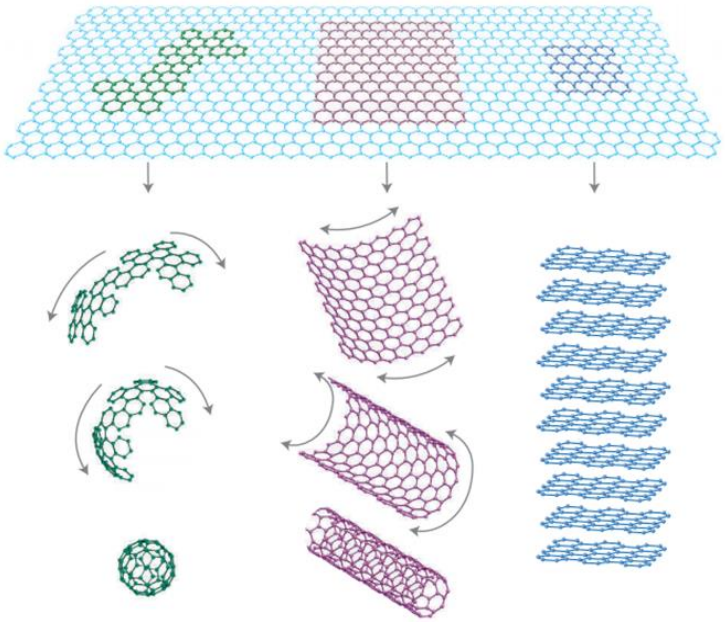

Figure 2.1. A schematic image of graphitic carbon allotropes derived from graphene; fullerene (zero-dimension), CNT (one-dimension), and graphite (three-dimension).

(**Copyright @ 2007 nature publishing group**).

Two approaches are generally available to produce graphene, including bottom-up and top-down

processes. The bottom-up process is based on chemical synthesis. Chemical vapor deposition (CVD) is a representative method that enables graphene production with high purity and low defect. However, this method cannot deploy a large scale of production due to a limited area of the synthesis. In other words, CVD is not appropriate for polymer nanocomposite studies which require a large scale synthesis of graphene.[14] On the other hand, the top-down process is based on the mechanical impact or liquid phase exfoliation of graphite. Thus, single layer graphene cannot be produced by this process while a few layered graphene sheets can be directly separated from graphite or graphite derivatives.[36] Consequently, the top-down process allows producing a large amount of multi-layer graphene (i.e. graphene nanoplatelets (GnP)), but it is insufficient to exfoliate the single layer graphene from graphite.[39] However, the GnP has lower structural stability than the graphene formed by CVD as a trade-off. Nevertheless, the GnP also effectively reinforces physical properties and gas barrier performance in its composites.[40, 41] In recent progress, GnP has received intensive attention in terms of a practical application of graphene due to its potential capability, providing low cost and mass production. Thus, GnP manufacturers have increased their production scale to be applicable in the field of polymer composites.[42] Besides, they can provide various grades of GnP products as a function of size or surface area. In this thesis, diverse sizes of commercial GnP manufactured by XG sciences (US) were used to fabricate polymer composites as well as synthesize different size of GO.

2.1.1.2 Graphene oxide and functionalized GO

Although GnP has been proposed a solution for graphene applications at the industrial scale, there are still some challenges need to be done in this research field. The most crucial challenge is further decrease of graphene layers to maximize the capacity of polymer/graphene composites. Mechanical cleavage of graphite has limitations to reduce the graphite layer due to the existence

of van der Waals force.[7] To overcome these limitations, a chemical method is required based on liquid phase. This method is usually conducted under high acidic conditions, including strong oxidants to generate oxygen-containing functional groups on the surface and edge of graphene sheets.[43] In general, GO is obtained through Hummer's method, which is a typical synthesis way. Concentrated sulfuric acid mixture containing potassium permanganate ($KMnO_4$) and sodium nitrate ($NaNO_3$) was commonly used to oxidize GnP or graphite powder. After the oxidization, hydrophilic functional groups, such as epoxide, hydroxyl, and carbonyl groups are generated on GO, leading the expansion of the interlayer distance of graphene sheet due to the intercalation of moisture with strong hydrogen bonding.[44] With the high affinity with moisture, GO can be uniformly dispersed in a hydrophilic solvent, such as acetone, tetrahydrofuran (THF), and even water. In the solution state, a few layers of exfoliated GO are presented by the hydrophilic functional groups in the solution, inducing the stable dispersion of GO. Aside from the empirical evidence, the concrete chemical structure of GO has been intensively discussed over the years, and various models have been proposed to explain the structural issue of GO. Among others, Lerf-Klinowski model in Figure 2.2 is widely used in contemporary graphene research.[15, 43] This model reveals that the epoxide and hydroxyl groups are closely linked to one another, and the edge of the GO layer is terminated from carboxylic acid groups.

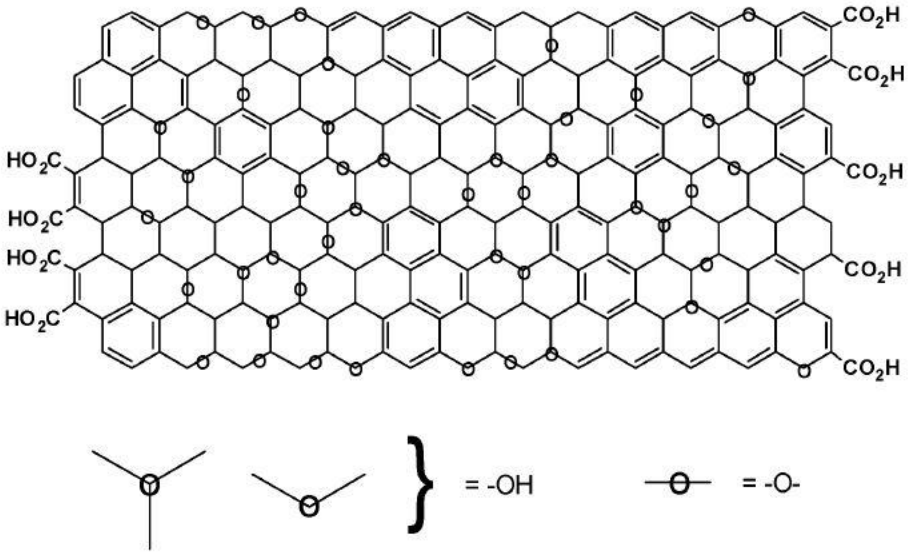

Figure 2.2. Lerf-Klinowski model regarding the presence or absence of carboxylic acids on the periphery of the basal plane of GO.

(**Copyright © 1998, American Chemical Society**)

These hydrophilic functionalities of GO render great compatibility with hydrophilic polymers, such as polyvinyl alcohol (PVA)[12] or water-dispersible polymeric colloidal particles.[45, 46] These hydrophilic polymer/GO composites revealed enhanced mechanical properties and gas barrier performance due to the uniform dispersion of GO as well as the interaction between the polymer matrix and GO. However, the hydrophilicity of GO confines its application to the polymer composites since it can provide only great miscibility with hydrophilic polymers or waterborne polymers. Thus, the surface of GO needs to be modified to expand its application to the various polymer matrices. Usually, the functionalization of GO can be taken place by a chemical reaction between hydroxyl or carbonyl groups on GO and reactive functional groups, such as isocyanate or amine groups. The isocyanate or amine-treated GO can be considerably exfoliated into organic solvents, such as dimethylformamide (DMF) and THF with a mild ultrasonication. In addition, the

functionalized GO (f-GO) enables greater interfacial interaction with polymer matrices than GO, because of the possibility to select an optimum functionalization agent to match with polymer matrices.[47] Herein, chlorinated GO (Cl-GO) intermediate can be utilized to increase the reactivity of the isocyanate or amine groups. Cl-GO is prepared by the reaction between carboxylic acid on GO and thionyl chloride ($SOCl_2$), providing high reactivity of acid chloride (COCl) with isocyanate and amine groups. The reaction mechanism of GO chlorination is shown in Figure 2.3.[48]

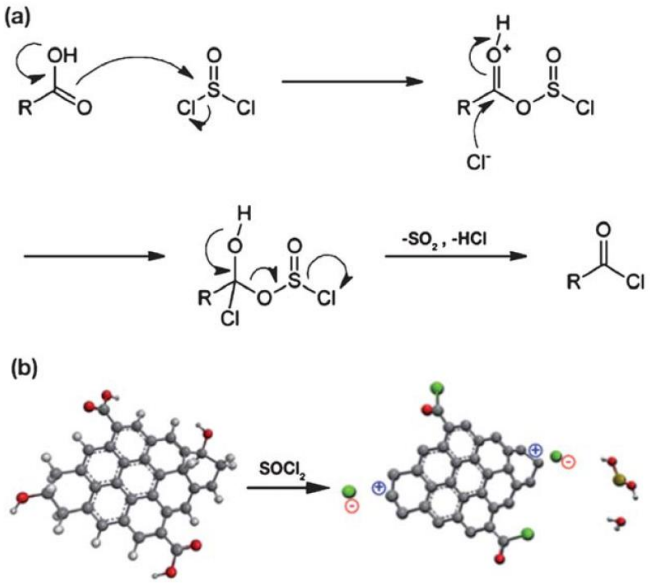

Figure 2.3. Schematic image for chlorination of GO (a): Proposed reaction mechanism in which a carboxylic acid is transformed to acyl chloride by $SOCl_2$ (R: aromatic or hydrocarbon groups); (b) visualization for the chlorination of GO.

Polymer composites, incorporated with the chemically modified GO, have been experimentally presented by past research groups. Particularly, f-GO is useful for solution-based processing, which is very attractive in a recent study. This is because this method can be used to a wide span

of applications from photonics, optoelectronic devices to polymer composites.[49] For this reason, solution-processable polymer composites with f-GO have been proposed as a novel material. Along this line, this thesis presents synthesis of f-GO with amine functional groups. Also, the design of solution-processable polyurethane composites incorporated with f-GO is provided.

2.1.2 Polymer matrix

2.1.2.1 Polyurethane

Polyurethanes (PU) are a wide class of polymeric materials, including the urethane group (-NCO-) in their structures. The urethane group (i.e. carbamate) is generally formed by the chemical reaction between isocyanate and hydroxyl groups. Isocyanate groups are basically very reactive due to their resonant structure which attracts electrons (i.e. electrophile). They can be converted into urethane groups quantitatively without by-products. Beside, polyol groups are capable of the controlling processability and physical properties of PU, but two or more functional groups (e.g. diol and diisocyanate) are required to polymerize PU. Specific properties of PU rely on the combination of the diisocyanates and diols due to the various type of isocyanate and diol derivatives. The chemical reaction among the isocyanate group, hydroxyl groups, and the polymeric structure of PU are shown in Figure 2.4.[50]

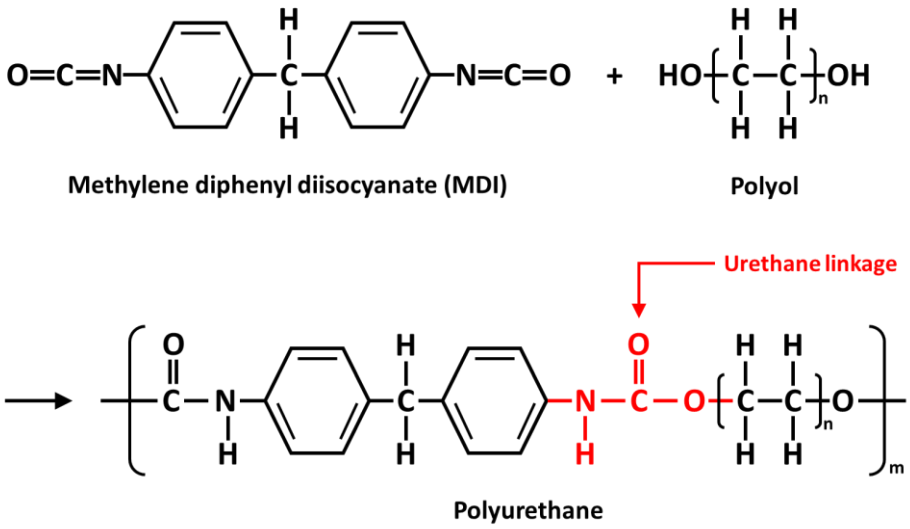

Figure 2.4. Schematic image of isocyanate, polyol, and polymerization of polyurethane.[50]

Among the various PU, polyurethane elastomers (PUE) are particularly important in an industrial scale because of the superior physical properties of PUE, such as high hardness, elasticity, and excellent chemical resistance. These strong physical properties are driven by unique structural characteristics. PUE has a two-phased polymeric structure consisting of hard and soft segments. The hard segment intervenes to the rigidity and strength of PUE and act as a physical crosslinking point within the matrix due to stiffer structure of diisocyanate moiety. The soft segment is associated with the polyol moiety. It contributes to the flexibility and elongation of PUE.[51] The schematic image of the polymeric structure of PUE is shown in Figure 2.5.

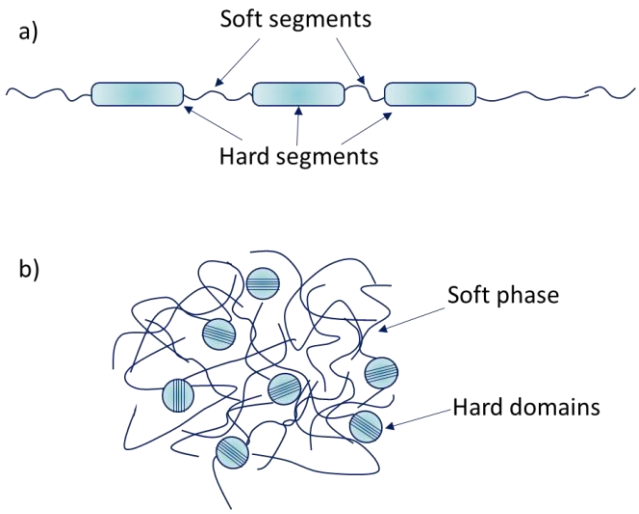

Figure 2.5. Schematic image of segmented polyurethane chain (a), and two-phase structure of the bulk polyurethane (b). [51]

Those structural properties provide high durability and toughness of PUE to be applicable for metal protection in a corrosive environment. Thus, PUE is very suitable for a pipeliner coating inside pipelines for oil sand transportation.[52] In general, hot water and bitumen in the oil sand slurry produce many corrosive agents, inducing the high temperature and corrosiveness. Also, the internal surface of the pipelines consists of carbon steel, inspiring the agents to accelerate the corrosion.[26] Herein, PUE can protect the inner surface of the pipe in the form of a pipeliner. This is a very effective form for protection due to the high mechanical and anti-corrosive properties. It is even greatly adhesive to carbon steel. Although the basic properties of PUE are suitable for the pipeliners the properties also depend on polymerization methods. PUE can be obtained by two basic polymerization methods, which are the one-step method and the prepolymer method. In the next session, the two methods will be discussed in detail.

2.1.2.1.1 One-step method

In the one-step method (i.e. polyaddition procedure), all reagents, such as polyol, diisocyanate, and chain extender are added at once on the initial stage of polymerization. This method is commonly very practical in terms of industrial production due to the simple reaction between diisocyanates and polyol components. For this reason, the polymerization process is basically fast, easy and reproducible. However, the diisocyanate and polyol reagents are usually incompatible at room temperatures, so the polymerization will take place on the interface between the two reagents. This incompatibility leads to a stoichiometric imbalance and structural heterogeneity within the PUE matrix. For this reason, this one-step method requires an appropriate mixing facility to minimize the incompatibility. Furthermore, high temperature that is slightly below the melting point can contribute to reducing the incompatibility of PUE during the mixing process. In the polymerization process of PUE, moisture is a critical factor to infer properties of the final PUE. The polyols are basically hygroscopic, inducing the moisture in the polyols to form bubbles through a chemical reaction with the diisocyanate. This phenomenon deteriorates PUE properties. Moreover, the unreacted diisocyanate, which is strongly associated with the contents of moisture, also affects the final PUE properties. For this reason, the reagents, such as diisocyanate and polyol, require appropriate packages to prevent moisture absorption. Nevertheless, diisocyanate and polyol would provide high productivity and cost efficiency of PUE owing to the easy processing. In this thesis, the one-step method is used as the main processing technique to fabricate the PU/graphene composites.[50, 51]

2.1.2.1.2 Prepolymer method

In the one-step method, moistures and unreacted diisocyanates were crucial factors to affect overall

properties of the final PUE. However, it is difficult to effectively prevent these issues because monomers of PUE are hydrophilic and PUE cannot be fully polymerized. Prepolymer method can be suggested to minimize the crucial issues of the one-step method. Prepolymers are generally defined as oligomers or resins (i.e. polymers), rather than monomers. In this method, PUE prepolymers are synthesized by the chemical reaction between diisocyanates and polyols. The synthesized PUE prepolymers are commonly high viscous liquid or solid at room temperature, because they have higher molecular weight than monomers. To complete the polymerization process of the PUE prepolymer, a chain extender such as 1,4-butanediol is required. The chain extender terminates the polymerization process of the PUE prepolymer by chemical reaction with isocyanate groups on the end of PUE prepolymer chains. For this reason, the prepolymer method is less susceptible to moisture than the one-step method because of the fewer diisocyanate. Therefore, a stronger PUE can be obtained by the prepolymer method due to the low moisture and unreacted diisocyanates contents. Challenges for the prepolymer method are a high material cost and a complicated production facility. PUE prepolymers are more expensive than the monomers of the one-shot method because of because of the prepolymerization process. Besides, this method requires a preheating facility to melt the PUE prepolymers before casting. Therefore, industries, which necessitate high quality of PUE, consider the prepolymer method. However, in the lab scale, this system is not recommended due to the reasons explained in this session.[51, 53, 54] For this reason, the one-step method is used to fabricate the polymer/graphene nanocomposites in this thesis, Nevertheless, the prepolymer method would be also considered for more practical application of the nanocomposites in further research.

2.1.3 Processing techniques for polymer nanocomposites

Polymer processing is generally one of the essential parts determining the properties of polymer

products. The mechanical and thermal properties of polymers that are associated with polymer structure can be influenced by various processing conditions. Also, properties of polymer nanocomposites incorporated with nanofillers can be influenced by the processing conditions. Distribution or orientation of the nanofillers is strongly associated with the processing conditions and the properties of the nanocomposites are attributed to the resulted nanofillers. For this reason, processing conditions should be carefully selected by the characteristics of polymers and nanofillers.[55]

In addition, equipment used in the processing crucially influences the final properties of polymers and their nanocomposites. Many polymer processing techniques are successfully used to produce various products in the marketplace. Polymer extrusion and injection molding are the most representative techniques for conventional polymer production because of their great productivity and cost-effectiveness. However, these processing techniques are more suitable to produce thermoplastic materials than thermoset materials. In general, thermoset polymers are suitable for the coating process since thermoset polymers are commonly in liquid form before the process, inhibiting the repetition after their solidification. For this reason, spray, centrifugal coating, and die-casting processes are generally utilized for the thermoset polymers. such as epoxy and polyurethane.[56]

Moreover, compounding or mixing is another important processing factor, especially for polymer nanocomposites. The properties of the polymer nanocomposites significantly depend on the dispersion of nanofillers. The dispersion is determined on the stage of the mixing process. Electrical, thermal, and anti-corrosive properties are synonymously related to the dispersion of nanofillers, because those properties are based on nanofiller networks. Therefore, the compounding or mixing process for the nanofiller dispersion is particularly important in

polymer/graphene nanocomposites. However, graphene requires additional treatment, such as oxidation or functionalization, for uniform dispersion within a polymer matrix because graphene is difficult to be retained as a single layer during the processing. For this reason, certain equipment, such as ultrasonication machine or centrifugal planetary mixer, would be effective for graphene dispersion into the polymer matrix. Therefore, a specific processing design is essential for the successful fabrication of polymer/graphene nanocomposites.[56]

2.1.3.1 PU coating process for protection of metal surface

PU has been used to a broad range of applications such as coatings, foams, and moldings due to the excellent physical and chemical properties. PU can offer not only good bonding properties with metal but also highly anti-corrosive performance. Thus, PU is particularly suitable for metal protection, such as steel pipes. In order to form a protection layer on a metal surface, a coating process using a liquid precursor is essential. This is because the coating process can uniformly cover the metal surface and minimize space between the protection layer. In the next session, anti-corrosive coating process will be presented along with understanding the definition and mechanism of metal corrosion.

2.2 Metal corrosion

Corrosion, generally known as rust, is a destruction of a metal substrate by a chemical or electrochemical reaction, which means transferring electrons. This phenomenon naturally occurs for most metals, because they intend to return to their original oxide form. Metal products in the commercial market are produced by the huge energy on natural minerals. Those pure metals are unstable in nature, inducing the conversion to their original form. In addition, this conversion (i.e. corrosion) is a basically irreversible reaction. The reaction can even be accelerated by

environmental factors, such as moisture and temperature. Therefore, corrosion has been a very important industrial issue because it is associated with a lifetime of metal products.[57]

In general, corrosion has had a negative impact on many areas of industry, especially transportation, construction, and manufacturing. In particular, corrosion has been an important issue in the oil and gas industries. In these industries, the enormous cost loss can be occurred by the corrosion at an astronomical scale. Among various segments of the oil and gas industries, pipelines for the transportation of oil slurry, which are up to dozens of km in length, are thoroughly exposed to corrosive circumstances, providing the high cost of replacement. For this reason, a strategy regarding the prevention of corrosion on both internal and external surfaces of pipelines is an essential part of the view of the industry. Protective coatings and corrosion inhibitors are usually used as protective strategies for metals. However, there is an increasing demand for research on advanced anti-corrosion technology. In this regard, polymer nanocomposites incorporated with layered carbon nanomaterials, such as graphene and graphene nanoplatelets, have had attention since they can be applied directly to coating processes as well as to improve corrosion protection.[58, 59]

2.2.1 Corrosion theory

At the basic process of the metallic corrosion in an aqueous solution, the anodic oxidation of the metal and the cathodic reduction of oxidants occur in the solution. The basic process is shown in the formula below:[60]

$$M_M \rightarrow M_{aq}^{2+} + 2e_M^- \qquad \text{anodic oxidation} \qquad (2\text{-}1)$$

$$2Ox_{aq} + 2e_M^- \rightarrow 2Red + (e_{redox}^-)_{aq} \qquad \text{cathodic reduction} \qquad (2\text{-}2)$$

In this formula, M_M is a metal, M^{2+}_{aq} presents the hydrated metal ion in aqueous solution, and e^-_M presents the electron from the metal. Ox_{aq} presents an oxidant, Red is a reductant, and e^-_{redox} presents the redox electron from the reductants. The overall reaction can be simply described as follow:

$$M_M + 2Ox_{aq} \rightarrow M^{2+}_{aq} + 2Red(e^-_{redox})_{aq} \quad (2\text{-}3)$$

These reactions are carried out by charge-transfer processes across the interface between the surface of metal and solution. Thus, the reactions depend on the interfacial potential corresponding to the electrode potential of metal. In practice, the cathodic process is occurred by the reduction of hydrogen ions or reduction of oxygen molecules in the solution. This reduction is based on electron transfer processes on the interface between the metal and solution, while the anodic oxidation is due to the ion transfer processes of the dissolution of metal. The formula and Figure 2.6 shown below indicates the corrosion process on a steel surface in the aqueous solution in a real environment.[61]

$$Fe \rightarrow Fe^{2+} + 2e^- \quad (2\text{-}4)$$

$$O_2 + 2H_2O + 4e^- \rightarrow 4OH^- \quad (2\text{-}5)$$

$$2Fe + O_2 + 2H_2O \rightarrow 2Fe(OH)_2 \quad (2\text{-}6)$$

$$4Fe(OH)_2 + O_2 \rightarrow 2H_2O + 2Fe_2O_3 \cdot H_2O \quad (2\text{-}7)$$

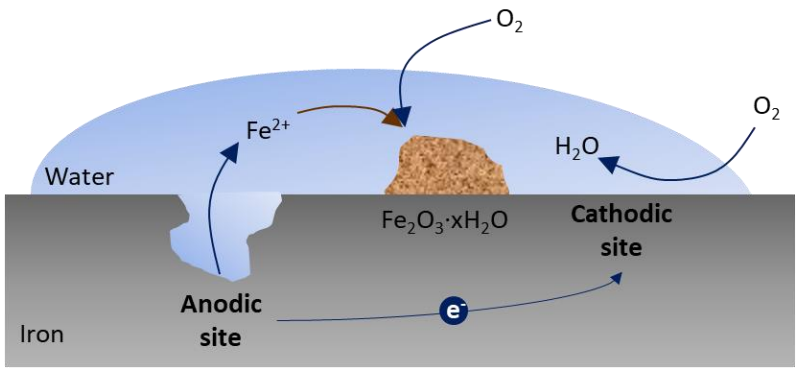

Figure 2.6. A schematic image for a corrosion process of a metal surface.

Where the free electrons (ne^-) from the iron reduce the dissolved oxygen and then form a hydroxide. Subsequently, the hydroxide transforms to an iron hydroxide ($Fe(OH)_2$), and then iron oxide hydrate ($Fe_2O_3 \cdot H_2O$), known as rust, is formed by additional oxygen supply. Therefore, in order to prevent metal ionization, it is critical to minimize the contact of water and oxygen with the metal and to inhibit the movement of ions and electrons.[61]

2.2.2 Protective coating for corrosion

Protective coating technology is the most commonly used way to protect the metal surface from a corrosive agent. Various coatings can be utilized for the protection, such as organic coatings (e.g. paints or plastic liners), metallic coatings, and nonmetallic inorganic coatings (e.g. ceramics or glasses). These techniques require multifunctional performance, which provides not only corrosion inhibition but also excellent mechanical property and adhesion of the metal surface. Thus, they can be used individually or combined for the protection purpose. There are three basic mechanisms of coatings or liners to inhibit corrosion:[62]

- Barrier protection

- Chemical inhibition
- Galvanic (sacrificial) protection

Barrier protection literally means the physical isolation of the metal substrate from the corrosive agent by coatings or liners. Chemical inhibition refers to the addition of inhibitive pigments to coating layers. The inhibitive pigments are chemical substances that can build a layer on the metal surface at a molecular level, served as a protection layer. This technique is typically useful to improve anti-corrosive performance of the protective paint layer. Galvanic protection presents forming an additional layer on the metal substrate using more active metal. This technique is commonly used to a galvanize steel consisting of a thin layer of zinc on the steel substrate. In this case, the steel substrate corresponds to the cathodic site, thus, the zinc layer will be at the anodic site. Among the protection methods, the barrier protection by organic coatings or liners using polymeric materials is beneficial in terms of maintenance and cost-effectiveness. This is because polymeric coating materials are basically anti-corrosive, easily processable, replaceable, and inexpensive. In addition, there are various polymers that can be selected to be applicable to specific corrosion protection applications. Table 2.1 indicates representative polymeric coating materials for corrosion inhibition.

Table 2.1. Representative polymeric coating materials for corrosion inhibition[58, 62]

Polymers	Advantages	Limitations	Applications
Epoxy	• Good chemical and weather resistance. • Excellent adhesion to steel and concrete.	• Harder and less flexible than other polymers. • Intolerant of moisture during application. • Long curing time (7 days)	• Widely used in maintenance coatings and tank linings.
Chlorinated rubber	• Fire resistant, odorless, tasteless, and nontoxic. • Low moisture permeability and excellent resistance to water. • Good chemical and abrasion resistance. • Quick drying with excellent adhesion to concrete and steel.	• Dissolved in strong solvents. • Degraded by heat (95 °C) and ultraviolet light. • Poor processability for coating.	• Concrete and masonry paints, swimming pool coatings, and marine finishes. • More common in Europe as an industrial coating
Fluoropolymer	• Hard, smooth, tough, flexible coatings with good color retention and high heat resistance. • Very good moisture and weathering resistance.	• Poor adhesion to many surfaces. specialized primers require. • Expensive cost. • Unavailable to apply thick coating. • Temperature resistance 260 °C.	• Coil-coating for exterior metal, wall and roof sheets. • Vessel liners, duct and fan coatings, and nonstick cookware.
Silicone	• High temperature resistance: 540 °C. • Excellent moisture, heat, and chemical resistance. • High gloss.	• High temperature curing require at 325 °C. • Unavailable to apply thick coating. • Expensive cost. • Adhesion problems possible.	• Exterior coatings for metal chimney, hot pipe, duct, and fan coatings.
Polyurethane	• Excellent adhesion, hardness, abrasion, and chemical resistance. • Fast cure, even at temperature below freezing. • Thick coating available.	• Humidity sensitivity concerns. • Darkening upon ultraviolet light radiation (sunlight).	• Widely used for many exterior structures in corrosive environments. • Relatively expensive but extremely durable.

Epoxy and polyurethane (PU) are widely used as protective layers because of their excellent chemical resistance, durability, and relatively low cost. In particular, PU is mechanically tough and highly anti-corrosive due to the unique structure of the polymer. In addition, the coating is suitable for PU processing, because of the liquid form of the PU pre-cursor. For this reason, pipeliners consisting of PU are applied to protect the interior surfaces of steel pipes laid on oil-sand transportation. These pipeliners extend the lifetime of the steel pipes, requiring only the periodic replacement for maintenance. The pipeliners are usually achieved by a centrifugal coating or casting technique. Centrifugal casting utilizes centrifugal forces, which are generated from the rotating pipe in a fast speed. The centrifugal forces move PU precursor to the inner surface of pipes and trapped air to the outside of coating layers. For this reason, the pipeliners formed by this technique indicate a thick but uniform thickness and few defects on the liners. Figure 2.7 presents the schematic image of the centrifugal casting method.

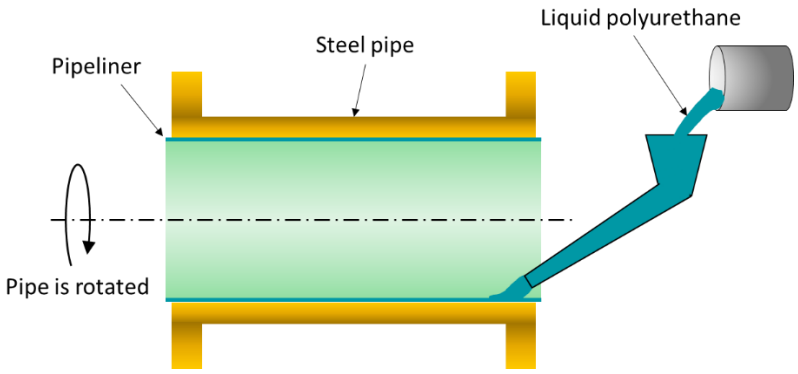

Figure 2.7. Schematic illustration of centrifugal casting method for the PU pipeliner.[63]

Nevertheless, PU is a sensitive polymeric material against moisture and this weakness of moisture can cause a problem known as a cold-wall effect that occurs on the interface between the pipeliner and the interior surface of the pipe. Moistures and ions can reach the metal surface through the cold-wall effect, rendering the corrosion to occur. In order to prevent the cold-wall effect of PU, many studies have been carried out, and PU composites incorporated with graphene or graphene nanoplatelets have been studied as a breakthrough for this problem.[62, 63]

2.2.3 Cold wall effect

The cold wall effect is commonly known as water vapor permeation, which was driven by a large temperature difference between inside and outside of pipes through the coating layer to the steel substrate. The water vapor passed through the layer results in the oxidation of the steel substrate. This effect can generally occur in a temperature difference above 38 °C. Thus, the hot slurry, such as oil-sand slurry, leads to significant cold wall effect, especially in winter. The cold wall effect is described in Figure 2.8.

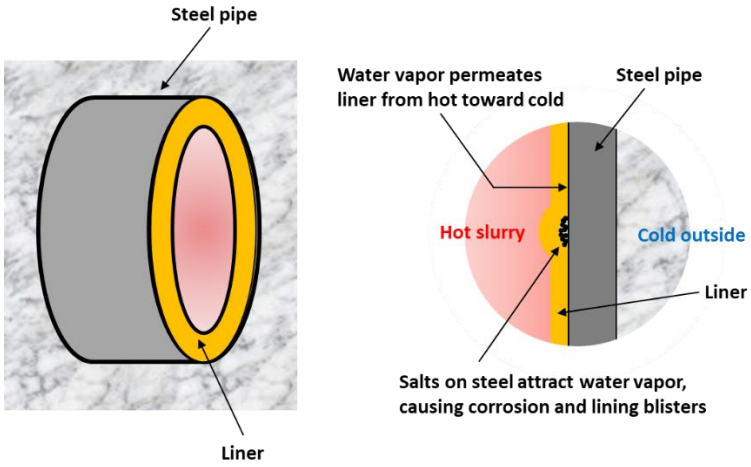

Figure 2.8. Schematic illustration of the cold wall effect in a pipeliner.[64]

Reducing the temperature difference between the exterior and interior can be a fundamental solution to prevent the cold wall effect. However, it is very difficult to control this factor because of a seasonal effect. Thus, increasing the liner thickness or additional insulation layer has been proposed as a substitute solution. Nevertheless, another problem, such as the decrease of pipe diameter or the increase of material cost, still exists on this issue. For this reason, a new idea would be required to overcome the cold wall effect of PU liner. Thus, graphene or graphene nanoplatelets have been studied as a filler to mitigate the effect in the PU liner.[64, 65]

2.3 Application areas

Graphene-based materials can be applied in various research fields due to their excellent mechanical, thermal, and electrical properties. In the field of polymer composites, much effort has been conducted in the development of electrically and thermally conductive polymer composites. For example, electrically conductive polymer/graphene nanocomposites can be applied to electromagnetic interference (EMI) shielding, electrostatic dissipation (ESD), bipolar plates for proton-exchange membrane fuel cell (PEMFC), and so on. In addition, thermally conductive

nanocomposites can be applied to heat-sensitive applications instead of metals and ceramics. However, this thesis will focus on the corrosion protection of graphene in the polymer/graphene composites and discuss the industrially useful applications.

2.3.1 Pipeliners for carbon steel pipes of oil-sand transportation

For at least 50 years, oil sand industries have been invested by energy companies and the government. As a result, the volume of the infrastructure of oil sand industries has expanded enormously as well as the development of the region that has deposits. In this industry, corrosion is a destructive phenomenon that causes a serious threat to the pipeline operation and ultimately the economy. The corrosive slurry, which flows in the pipe, includes acids, sand, and bitumen. They can break down the pipe's inner wall. Besides, environmental factors, such as temperature and weather, can accelerate the corrosion.[52] Therefore, a growing number of studies have been devoted to various approaches to inhibit or mitigate corrosion. The pipeliner method on the pipe wall is a common anti-corrosion method currently on the market. Inorganic pipeliners such as plating and sputtering are not cost-effective due to the high price of the raw material as well as the intricate formation of the liner. Conversely, the price of an organic liner, which is representative of polymers, especially PU, is relatively low. The organic liner can even be formed in a pipeline in a simple way.[63] These advantages have motivated companies dealing with hydro-transport of oil sands to expand using this technique. However, the mechanical properties of PU pipeliner are insufficient to fully protect the pipe against large slurry. Furthermore, the cold-wall effect regarding spot corrosion on the interface between the pipe and the liner can occur since PU is sensitive to moisture.[57] Therefore, the oil sand industries are looking for alternative materials that can prevent corrosion, withstand strong friction, and reduce expenditures. Graphene materials can be a candidate to solve this problem in a simple way to form the PU composites. Graphene-

based materials are proven material to reinforce the intrinsic properties of polymers because of their high mechanical and barrier properties. In addition, PU for the pipeliners contains a liquid precursor. Thus, the graphene-based materials can be directly mixed into the precursor, leading the dispersion into a PU matrix.[28] Based on these advantages of the graphene-based materials, many efforts regarding anti-corrosion performance using the PU composites have been carried out in the view of the industry.

2.3.2 Anti-corrosive paint

From a practical point of view, anti-corrosive paint can be a more practical application to use graphene materials for corrosion mitigation. Corrosion-resistant paints basically protect the metal surface from moisture, rain, oxygen in the air, and sunlight exposure. The anti-corrosive paints suppress the corrosion by preventing the direct contact of air and moisture to the metal. The anti-corrosive paint typically includes corrosion-resistant components, such as lead chromate, zinc chromate, zinc oxide, and so on. Especially, zinc-based materials are very well known anti-corrosive pigments. They are generally applied in the paint industry. However, the zinc-based inorganic materials are not compatible with polymeric materials, which are the main materials of paint. Thus, the inorganic materials can be migrated from the paint to the surface and can be exposed to the air.[66] This is a critical issue that is associated with human health. Thus, alternative materials have been constantly explored. Among the candidates to substitute the zinc-based materials, graphene-based materials show excellent splitting capacity and plasticity, chemical, and thermal resistance. The graphene-based materials are particularly useful in color paints as a pigment because of their high light stability against ultraviolet radiation from sunlight. This advantage is due to the exceptional barrier properties, which are attributed to the lamellar structures of graphene-based materials. In addition, graphene materials can be modified by other functional

groups. This modification contributes to improving the compatibility between the graphene materials and the paints. Therefore, the anti-corrosive paints, including graphene materials, can prevent the migration of the graphene pigments. These advantages of graphene materials are very important in the paint industry and a key role in the application of anti-corrosive paint.[66, 67]

3. Characterization Techniques

3.1 Physicochemical characterization

3.1.1 Scanning electron microscopy (SEM)

Scanning electron microscopy (SEM) is one of the most important characterization technique to observe the morphology of a material in the micro and nano-scale. The resolution of SEM has recently reached a considerable level due to its technological development. SEM can be equipped with various accessories that can provide information on local chemistry and crystallography. Thus, SEM is an essential part of modern research fields. SEM employs an electron beam emitted from an electron gun. An electron-optical lens system enables SEM to focus on the surface of a target specimen. The electron beam interacts with the specimen and then a couple of emission signal is generated by the interaction. Subsequently, images would be derived by a transformation of the signals. The emission signals have an extremely small wavelength. Thus, SEM allows observing micro- or nano-structured materials. A schematic overview of the SEM principle is shown in Figure 3.1.

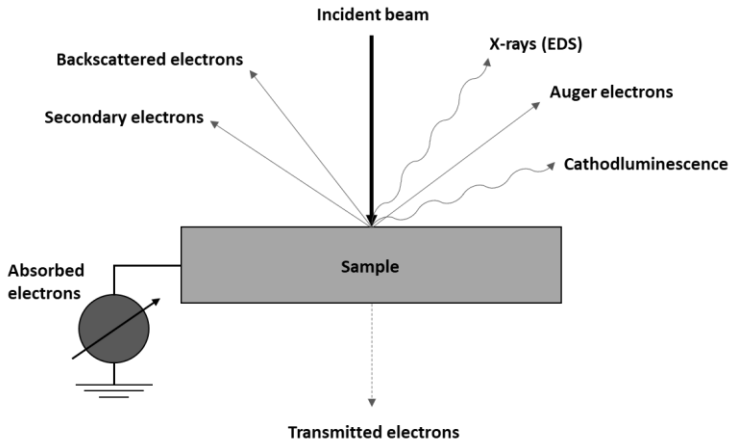

Figure 3.1. Schematic illustration of possible emission signals created by the incident electron beam in SEM.[68]

The most frequently detected signals are backscattered electrons in high-energy, secondary electrons in low-energy, and X-rays, while Auger electrons and cathode luminescence are less common signals. Therefore, the final images are provided by the conversion processing of the two frequently detected electrons such as backscattered and secondary electrons.[68]

3.1.2 Transmission electron microscopy (TEM)

Transmission electron microscopy (TEM) is a similar microscopy technique to SEM. This technique also utilizes an electron beam and serves direct morphology of samples. However, TEM detects the beam of electrons that is transmitted through a specimen, rather than SEM. For this reason, the specimen of TEM is usually an ultrathin film less than 100 nm thickness or a suspension on a grid. The electrons, which are transmitted through the samples, interact with the specimen and then an image is formed by the interaction. Therefore, TEM is capable of investigation about internal morphologies of the specimen.

3.1.3 X-ray diffraction (XRD)

X-ray diffraction (XRD) is a powerful nondestructive technique and provides useful information about the crystal structure of materials. A diffraction pattern is produced by the interaction between the x-rays and a sample. XRD shows diffraction angles corresponding with specific crystal planes of the sample. XRD would scan samples over a range of angles and then the diffracted x-ray beam at specific angles is detected by a goniometer. The diffraction angle is associated with the intrinsic crystal structure of samples and this result is derived by Bragg's law as follows:

$$2d \sin \theta = n \lambda \quad (3\text{-}1)$$

where n is the order of reflection (any integer), λ presents the wavelength of the x-rays, d presents the characteristic spacing between the crystal planes of a given specimen, and θ represents the angle between the incident x-ray and reflecting on lattice plane, respectively. Thus, amorphous materials cannot produce a specific XRD pattern. This is because there is no ordered crystal plane in the amorphous materials that can produce diffraction patterns. XRD data obtained by the diffraction pattern can be compared with the standard line patterns (i.e. theoretical diffraction pattern provided by Powder Diffraction File database). Therefore, XRD analysis can be reliable due to the comparison with the standard patterns. In summary, the XRD technique can provide information about crystalline structure in a given material with high reliability.[69]

3.1.4 Raman spectroscopy

Raman spectroscopy is based on the inelastic scattering of monochromic light that means the frequency change of the light by interaction with a sample. The inelastic scattering is attributed to the phenomena about the emission (Stokes process) or absorption (anti-Stokes process) of phonons in the light. The emitted or scattered light leads to an energy shift of the incident light by the

frequency change. This shift can be converted to Raman spectra in wavenumber (cm^{-1}), providing information regarding vibrational, rotational and other low frequent transitions in molecules. Therefore, Raman spectroscopy provides a nondestructive and noncontact characterization method similar to XRD with a fast scan rate. In addition, Raman spectroscopy is very sensitive to the structure of sp^2 carbons. For this reason, Raman is widely used to analyze structural properties (e.g. disorder and defect) of carbonaceous materials such as graphene and CNT.[70] In particular, Raman spectroscopy provides useful information to estimate defects or disorder of graphene structure. This fact is characterized by two remarkable peaks at around 1340 and 1506 cm^{-1} in the Raman spectra of graphene. G band is associated with the peak of 1506 cm^{-1} and due to the motion of 2 sp^2 carbon atoms (i.e. E_{2g} vibration). D band is associated with the peak of 1340 cm^{-1} and attributed to defects in the graphite material such as edge defects, bond-angle or length disorder, and vacancies etc. The intensity ratio of D band and G band (I_D/I_G) provide a relative disorder status of graphene materials. Thus, higher ratio I_D/I_G of presents more defects of the graphene materials.[71] Raman spectra of graphite, GO, and reduced GO (rGO) are shown in Figure 3.2.

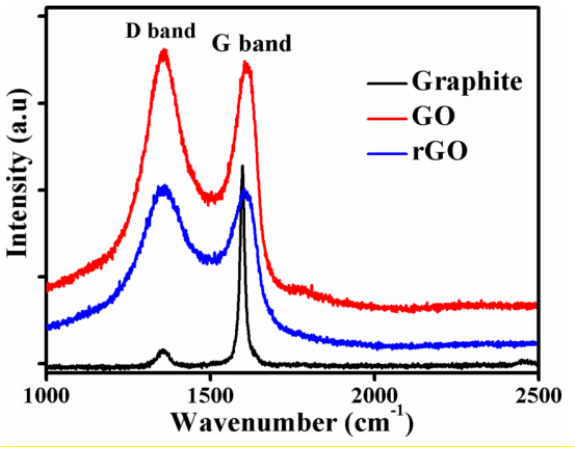

Figure 3.2. Examples of Raman spectra for graphite, graphene oxide (GO), and reduced graphene oxide (rGO).[72]

In Figure 3.2, graphite indicates a stronger G band than GO and rGO while strong and broad D band is shown in GO and rGO spectra. Thus, the I_D/I_G of GO and rGO increases to 1.03 and 0.93 from 0.7 of graphite. This means that defects of GO were increased by the oxidization process and these defects still remained on rGO after the reduction process. These facts allow estimating the integrity of the graphene structure. Therefore, Raman spectroscopy has been utilized as a standardized method for analyzing graphene materials.

3.1.5 Differential scanning calorimetry (DSC)

Differential scanning calorimetry (DSC) is a thermo-analytical technique, detecting heat flow difference between a sample pan and a reference pan. The sample pan includes a small amount of specimen and the reference pan is empty. Each pan is positioned on an individual sample base inside of DSC. The sample and reference pans are linearly heated by the equipment to maintain the same temperature of the two pans. Electrical power, increasing or maintaining temperature for both pans, corresponds with the heat flow. DSC precisely detects the heat flow and then converts the difference to a curve of heat flux as a function of temperature. DSC provides information about a thermal effect in a given material such as melting, crystallization, phase change, and even chemical reaction. DSC is particularly useful to measure heat capacity. Thus, it is widely used to determine the glass transition temperature of polymeric materials. Therefore, this technique has become an essential part in terms of thermal analysis for materials.[73]

3.1.6 Thermogravimetric analysis (TGA)

Thermogravimetric analysis (TGA) is another type of thermal analysis similar to DSC. TGA focuses on the mass change of a sample in a range of temperature or time under the desired environment. A precise microbalance is embedded in TGA. The mass of the sample is continuously

measured by the balance with increasing temperature under the air or inert gas atmosphere. Thus, TGA provides information in regards to thermal stability, chemical reaction, and residual contents of materials. For this reason, TGA is widely used to observe decomposition patterns and degradation kinetics of materials. Besides, it is capable of estimating the composition of a material. In particular, differential thermogravimetric analyses (DTG) obtained from TGA data provides a kinetic information regarding the degradation of materials. Therefore, TGA is useful to determine a temperature range of decomposition for polymeric materials. This is because a study about the degradation behavior of polymers is associated with the application of their final products.[73]

3.1.7 Fourier-transform infrared spectroscopy (FT-IR)

Fourier-transform infrared spectroscopy (FT-IR) is a chemical analytical technique. FT-IR is usually utilized to identify organic materials. FT-IR is based on the measurement of infrared (IR) absorption by a sample at a specific wavelength. The obtained spectrum from IR absorption provides information about molecular components and structures of a sample. Chemical functional groups in organic materials usually adsorb IR radiation at a specific wavenumber range. This is because the molecular motion of the functional groups, such as stretching and bending, has a frequency corresponding with a wavelength of IR radiation. For instance, the stretching band of carbonyl group (C=O) is shown at around 1700 cm^{-1} and the stretching band of ether group (C-O-C) appears at around 1100 cm^{-1}. In addition, FT-IR provides a wide spectral range that facilitates to characterize various chemical functional groups in the organic materials.

The FT-IR spectrum is commonly produced by an interferometer, which can convert from a broadband IR to a single-beam IR spectrum. Fourier transformation (mathematical method) is used for this technique. FT-IR spectra are represented as plots of intensity versus wavenumber (in cm^{-}

[1]) by this method. Herein, the wavenumber presents the reciprocal of the wavelength. The intensity of the FT-IR spectrum is shown as absorbance (A.U) or transmittance (%), respectively. As mentioned above, FT-IR is very useful to identify chemical functional groups while it is qualitative analysis. Thus, FT-IR is not used for quantitative measurements, such as concentration or intensity comparison among the chemical functional groups. Nevertheless, FT-IR is essential to the chemical analysis of a given material with fast and reliable performance.[74]

3.2 Mechanical property characterization

3.2.1 Tensile properties

Tensile properties are typically representative of mechanical properties of a material. Tensile testing is a fundamental technique for material science and engineering. Tensile testing is carried out by controlling the strain of a specific specimen until failure and then strain-stress curve is obtained by processing the strain and stress data on the specimen. A typical strain-stress curve for polymeric materials is shown in Figure 3.3.

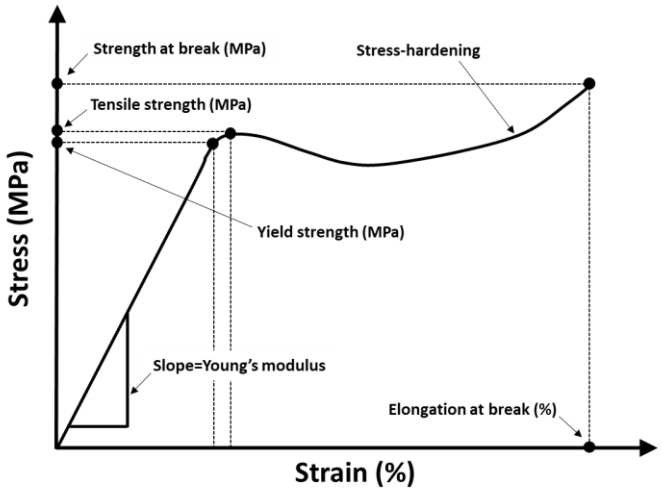

Figure 3.3. Schematic image of a typical stress-strain curve for polymeric materials.[75]

Properties, such as tensile strength, elongation at break, and strength at break, can be directly measured by the testing. Other properties, such as Young's (elastic) modulus, yield strength, and strain-hardening characteristics, can be determined after the testing. The Young's modulus is representative of the stiffness of materials. This parameter is determined by the initial linear slope of the strain-stress curve. The strain-hardening occurs above a certain strain and means a strengthening effect of materials. This parameter is driven by dislocation movements of the material. In particular, the strain-hardening effect in polymeric materials is driven by the orientation of polymer chains. The tensile strength presents the maximum tensile stress before failure. The elongation at break presents the maximum strain until the specimen is ruptured and this parameter is related to the ductility of the material. The strength at break represents the stress, which required to draw a specimen up to the elongation at break. Tensile testing for polymeric materials is performed by the universal testing machine (UTM) based on ASTM D638-14 "Standard Test Method for Tensile Properties of Plastics". The uniaxial direction is the most commonly selected for tensile testing. Specific specimens, according to ASTM above, is used to compare the mechanical characteristics of materials.[76]

3.2.2 Hardness

Hardness is another one of important mechanical properties. This property represents the resistance of localized plastic deformation by a certain external impact, such as mechanical indentation or abrasion. Hardness is dependent on elasticity, stiffness, strength, toughness, and viscoelasticity of materials. Hardness provides a relative comparison among specimen and there is a couple of standards for testing hardness. In general, the indentation method is widely used to measure the hardness of samples. This method is achieved by a constant compression on a sample surface using

a sharp object. Rockwell, Vickers, Shore, and Brinell are provided as common indentation hardness scales. Among the scales, the Shore scale is suitable for measuring the hardness of polymeric materials, especially for elastomers or rubbers. The Shore hardness is performed by Shore durometer that is rapid and easy to measure the hardness of the specimen. ASTM D2240 is provided as the standard for Shore durometer and this standard has a total of 12 scales depending on the type of indenter. Type of Shore A and D is the most common scale for polymeric materials; the A scale is suitable for soft polymers, while the D scale is suitable for hard polymers.[77, 78] A schematic image about the Shore durometer is shown in Figure 3.4.

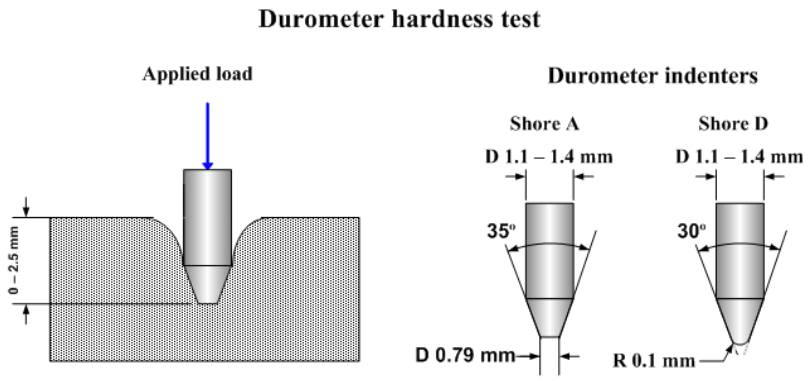

Figure 3.4. Schematic image for hardness measurement using durometer and the types of durometer indenters.

(**Open source, No copyright**)

In addition, the hardness, which is carried out on elastomers, correlates with Young's modulus of the elastomers. The correlation is given by the equation 3-2 determined by the Shore durometer and tensile testing.[79]

$$\mathrm{E(MPa)} = \frac{0.0981 \cdot (56 + 7.66s)}{0.137505 \cdot (254 - 2.54s)} \tag{3-2}$$

Where s presents Shore hardness. Although this equation is derived from the semi-empirical method it is useful for understanding the correlation between the hardness and Young's modulus of elastic materials. In particular, hardness measurement is suitable for quality control in an industrial production due to the test convenience and reliability. Besides, the mutual conversion of Young's modulus and the hardness is also valuable for academic research.

3.3 Electrochemical corrosion testing

As explained in the previous chapter, all corrosion phenomenon is a chemical or electrochemical process regarding oxidation and reduction reaction. Thus, electrochemical experiments are required for detecting a flow of electron (i.e. current) by the corrosion reaction. These experiments are carefully carried out under a certain environment because the reaction is dependent on the testing circumstances. In other words, parameters for the electrochemical experimental system are precisely controlled to characterize the corrosion property of materials. In practice, a polarization cell is widely used for the corrosion testing. This cell includes three electrodes, such as a reference electrode (RE), a counter electrode(s) (CE), and a working electrode (WE). This system is generally working with an electronic device that is called a potentiostat. The three electrodes are placed in an electrolyte that is usually a solution state under controlled temperature. Voltage (i.e. electrochemical potential) is applied on each electrode in the solution and then the system detects a current in regards to oxidation and reduction reactions.[80] A schematic image of the polarization cell for the corrosion testing is shown in Figure 3.5.

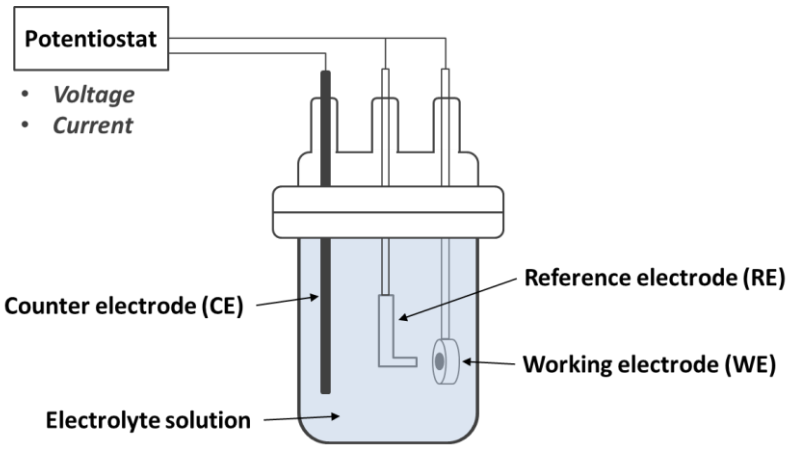

Figure 3.5. Schematic illustration of the polarization cell system for electrochemical testing.

Potentiodynamic experiment is commonly used to evaluate the corrosion performance of the materials. In this experiment, the potential is scanned in the predetermined range, the current is constantly measured. This potentiodynamic scan of potential is referred to as cyclic voltammetry or reverse polarization.

In addition, electrochemical impedance spectroscopy (EIS) is performed by the polarization cell. In particular, EIS is useful for measuring the anti-corrosion performance of a protective coating layer. EIS experiment also utilizes the three electrodes system for corrosion testing. However, its result is explained in a different way using impedance as a function of frequency. Besides, EIS provides an equivalent circuit model to systematically explain the corrosion circumstance. In the next session, cyclic voltammetry and EIS will be discussed in detail, as main techniques for evaluating the anti-corrosion performance of a material.[80]

3.3.1 Cyclic voltammetry (CV)

Cyclic voltammetry (CV) is one of the most common potentiodynamic experiments (i.e. potentiodynamic polarization) and very useful for evaluating corrosion of a material. CV is

performed by cycling the potential on working electrode (WE) in a predetermined range. The resulting current is continuously measured as a function of potential during the cycling process. The potential of WE is linearly increased and then varied in opposite potential by a constant time rate. These cycles of potential are repeated as a couple of times as desired. A potentiodynamic polarization curve is obtained by plotting the current versus WE's potential.[80] Tafel plot is typically used to analyze the potentiodynamic polarization curve. Parameters regarding the corrosion property of materials are extracted from the plot. Tafel analysis is based on direct current (DC) technique that uses a large potential. Thus, this technique produces a large current as a response to the potential. However, the relationship between the current and the potential is non-linear. For this reason, a semi-log plot, which is called Tafel plot, is used in the current axis. The typical Tafel plot is shown in Figure 3.6.

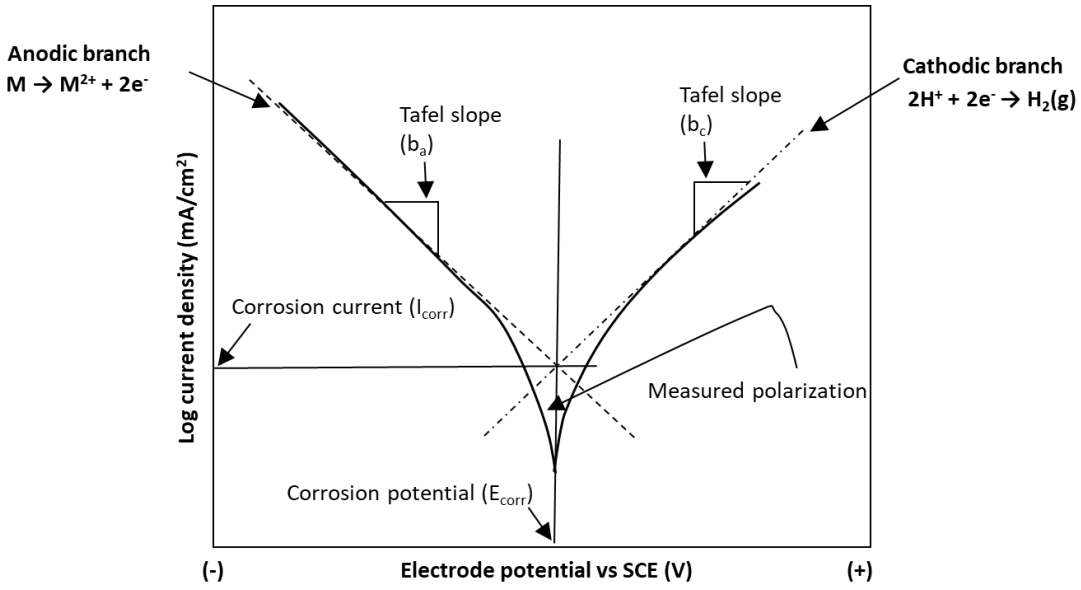

Figure 3.6. Image of typical Tafel plot.[81]

The Tafel plot consists of an anodic branch corresponded with oxidation, and a cathodic branch corresponded with reduction. Each branch includes a linear extrapolated curve, and the crossing

point of each extrapolated curve provides the corrosion current (I_{corr}) at the corrosion potential (E_{corr}). These two parameters are used to evaluate the anti-corrosion performance of the materials. The slopes of the anodic (b_a) and cathodic (b_c) linear curve present the Tafel coefficients. Those coefficients are utilized to determine linear polarization resistance (R_p) based on Stern-Geary equation as shown below.[82]

$$R_p = \frac{b_a \cdot b_c}{2.303 \cdot I_{corr} \cdot (b_a + b_c)} \quad (3\text{-}3)$$

R_p is provided as another parameter to quantitatively compare the anti-corrosion performance. In summary, CV provides various parameters regarding the anti-corrosion performance due to Tafel analysis. They are very useful to evaluate the corrosion properties of the materials. Nevertheless, CV has challenges, such as the low corrosion rate and the low electric conductivity of the electrolyte. Besides, it can be ineffective to measure the corrosion at WE covered with a thick protective layer. For this reason, electrochemical impedance spectroscopy is usually used to complement the CV technique.

3.3.2 Electrochemical Impedance Spectroscopy (EIS)

Electrochemical impedance spectroscopy (EIS) measurement is based on alternating current (AC) technique, rather than CV. EIS provides reliable results in regards to the anti-corrosion performance of the materials. In particular, this technique is useful for measuring the anti-corrosion performance of a protective layer on WE. Thus, EIS is used to evaluate the corrosion property, individually or accompanied by CV. EIS is performed by the application of AC and then the frequency of AC is varied in a predetermined range. Thus, EIS measurement is dependent on the AC frequency. For this reason, the results of EIS are indicated as resistance and capacitance

properties.[80] Nyquist and Bode plots are predominantly used to analyze the EIS results. The Nyquist plot is more commonly used to evaluate the corrosion property than Bode plot. This is because the Nyquist plot is effective to measure the corrosion that is occurred on a surface of a material. Furthermore, an equivalent circuit model is provided to facilitate the analysis of the plot. Parameters regarding the corrosion properties are extracted from the circuit model. Nyquist plot is plotted by two parts, such as the imaginary impedance (Z") and the real impedance (Z').[83] A typical Nyquist plot and the corresponded equivalent circuit are shown in Figure 3.7.

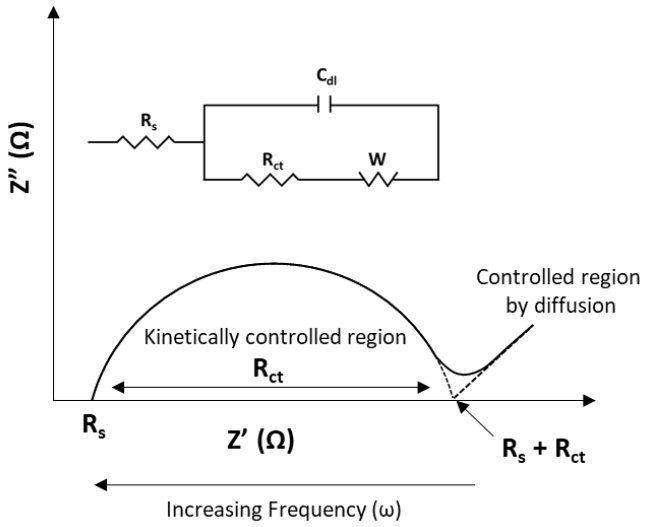

Figure 3.7. Typical Nyquist plot and the corresponded equivalent circuit model.[81]

In Figure 3.7, R_s presents solution resistance, R_{ct} presents the charge transfer resistance, C_{dl} presents the double-layer capacitance, W presents the Warburg diffusion, and ω presents the angular frequency. Among the values, R_{ct} is associated with the corrosion resistance of materials. Thus, it is important to gain the semi-circular curve for the precise analysis of the Nyquist plot. In addition, various equivalent circuit models can be applied to the Nyquist plots according to corrosion circumstances. In summary, EIS is another useful technique for the evaluation of the

corrosion property. In particular, EIS provides a precise measurement for the surface corrosion of a protective coating layer. This is because EIS is highly sensitive to the surface change. Thus, EIS is widely used to compare the corrosion property of the materials, accompanied by CV.

4. The investigation of size effect of graphene nano-platelet (GnP) on anti-corrosion performance of polyurethane/GnP nanocomposites

This chapter is reprinted in adapted form from the article below with permission from RSC.

Jun Geun Um, Yun-Seok Jun, Hesham Alhumade, Hariharan Krithivasan, Gregory Lui and Aiping Yu, "Investigation of the size effect of graphene nanoplatelets (GnPs) on the anti-corrosion performance of polyurethane/GnP composites", *RSC Adv.*, 2018, 8, 17091.

4.1 Introduction

Corrosion, commonly known as rusting, is defined as a chemical or electrochemical reaction between a metal substrate and a corrosive agent such as oxygen or moisture.[84-88] Corrosion mitigation is critical in modern industries owing to the high cost of maintenance and replacement of parts.[89-92] Organic coatings are the most common method for protecting metal surfaces from a corrosive environment.[93-95] Among diverse organic materials, polymer coatings are widely used as a protective layer to prevent corrosion because they provide not only high anti-corrosion performance but also excellent adhesion to metal substrates.[96-99] For instance, polyurethane (PU) and epoxy are commonly used coating materials as the protective layer on metal substrates.[98-104] PU has especially attracted many researchers because of its exceptional mechanical property as well as an excellent adhesion to the metal.[50, 105, 106] PU is based on the reaction between the isocyanate (-NCO) group and a polyol including hydroxyl groups (-OH), where the isocyanate group and polyol comprise a hard segment and soft segment respectively.[107] Due to the segmented structure, PU has high strength and elongation. For this reason, PU has been

applied to various fields and industries such as construction, oil and gas industry, automotive, and health care owing to its broad versatility. However, PU has inferior abrasion resistance and gas permeability relative to metal, both of which are necessary for use in harsh conditions such as the transportation of oil sands.[105-108] To overcome this problem, numerous researchers have studied a polymer nanocomposite incorporating various nanofillers, such as a layered silicate, carbon nanotubes (CNT), graphene, and graphene nanoplatelets (GnP) to improve such properties.[37, 109] Among them, nanocomposites integrated with graphene and GnP are recently emerging as a new breakthrough.[37, 110, 111]

Graphene is a two-dimensional one atomic layer platelet structure that consists of sp^2-bonded carbon atoms.[112] Many researchers have focused on nano-carbon materials since the advent of graphene due to its outstanding mechanical (Elastic modulus: 1 TPa)[113], thermal (Thermal conductivity: 5000 W/(m·K)) and electrical (Electrical conductivity: 6,000 S/cm) properties.[114, 115] Specifically, a number of researchers have incorporated graphene into polymer nanocomposites for improved barrier properties due to its excellent impermeability.[116] However, several challenges such as the uniformity of graphene dispersion and its high manufacturing cost, prevent the widespread use of graphene for the polymer nanocomposite.[117] For this reason, graphene nanoplatelet (GnP) have gained great interest as the next ideal filler for the polymer nanocomposite.[117-120]

GnP consists of 10 to 60 graphene layers and can be produced in a relatively easier and more economical way than single layer graphene.[117, 118] Furthermore, a higher degree of dispersion of GnP within the composite can be achieved in comparison to graphene.[121] This advantage of GnP holds promise to minimize gas permeability which is directly related to the improvement of anti-corrosion performance.[38, 122] and the tensile modulus of the composites. For instance,

Pinto et al.[123] reported that poly(lactic acid) (PLA) nanocomposites incorporated with GnP and graphene oxide (GO) reduced gas permeability by 65% and 60%, respectively, with a loading of 0.6 wt%. King et al.[124] This revealed that the tensile modulus of epoxy/GnP nanocomposites gradually increased with GnP contents up to 6 wt%. Although GnP has a large attraction as previously mentioned, it has not been studied sufficiently in the research field of a polymer/GnP composite at this point in time. Therefore, further study of GnP is needed to improve an inherent, inferior polymer property such as gas permeability and this study is expected to contribute more practical polymer nanocomposites including GnP based on relatively easier commercialization of GnP than the single graphene.[120]

In this study, commercial PU and GnP were used to fabricate PU/GnP nanocomposites. The prepared nanocomposites were coated on a copper (Cu) substrate as a protective layer against a corrosive media. In addition, four grades of GnP with different sizes were compounded with PU via the planetary centrifugal mixer (PCM). The nanocomposites were analyzed regarding various properties including mechanical and electrochemical properties. Herein, this study specifically focused on the corrosion behavior of the PU/GnP nanocomposites on the Cu substrate in a fixed content of GnP (1 wt%) and investigated the size effect of GnP on the corrosion resistance in a corrosive media. The existence of GnP improved the anti-corrosion performance of the PU/GnP nanocomposites and the smaller size of GnP led to the improvement of the performance of the nanocomposites. However, mechanical properties of the nanocomposites were partially improved, and this result was related to the interfacial property between GnP and the polymer matrix. Furthermore, an appropriate model to correspond with the results of this study was proposed.

4.2 Experimental

4.2.1 Materials

RenCast 6401, commercialized highly flexible and abrasion resistant PU purchased from Huntsman (US), was used as a matrix material for the PU/GnP composites. RenCast 6401 is composed of the resin (6401-1, viscosity: 50 cP) including 4,4'-Methylene diphenyl diisocyanate (MDI) with triethyl phosphate and the hardener (6401-2, viscosity: 1,300 cP) including oxyalkylene polymer (i.e. polyol) with 1,4 butanediol as a chain extender. The mixing ratio of resin and hardener was 25:100 by mass. The four grades of GnP from XG science (US), which are also commercialized, were used as the filler for this study. The grades of GnP used were xGnP H100, M25, M5, and C750, and were distinguished by the average diameter corresponding with a size and surface area of GnP. According to the technical report from XG science, H100 grade has an approximate diameter of 150 μm and a typical surface area of 50 to 80 m^2/g. The average diameters of M25 and M5 are 25 and 5 μm, respectively, with typical surface areas of approximately 120 m^2/g and 150 m^2/g, respectively. C750 has the smallest diameter under 2 μm with the average surface area of approximately 750 m^2/g. The density of all grades is 2.2 g/cm^3. The basic physical properties of the commercial GnP are summarized in Table 4.1.

Table 4.1. Technical information of commercial GnP in this study given by manufacturer

Grade	Diameter (Avg. μm)	Surface Area (m^2/g)	Density (g/cm^3)
xGNP H100	150	50~80	2.2
xGNP M25	25	~120	2.2
xGNP M5	5	~150	2.2
xGNP C750	< 2	~750	2.2

4.2.2 Preparation of samples

The four different grades of GnP (Grade H100, M25, M5, and C750) were dried in a vacuum oven at 80 °C for 16 hours to remove moisture and then were dispersed in the hardener at 1 wt% mass loading [50 mg] using PCM (YS-2E, China) for 40 minutes. The resin was added to the mixture of the hardener and GnP with a resin:hardener ratio of 25:100 by mass, with the mixture being mixed for 10 minutes. The final mixtures were cast on clean polyethylene terephthalate (PET) substrates (thickness: 100 μm) and polished Cu substrate (thickness: 30 μm). A 300 μm film was cast using an adjustable film applicator (GARDCO, width: 76 mm). The film was then procured at room temperature for 2 hours to form a skin layer and cured completely in a vacuum oven at 40 °C for 16 hours. The cured film on the PET substrate was peeled off for mechanical testing whereas the film on the Cu substrate remained intact and was used directly for electrochemical measurements. The process of the sample preparation is schematically illustrated in Figure 4.1.

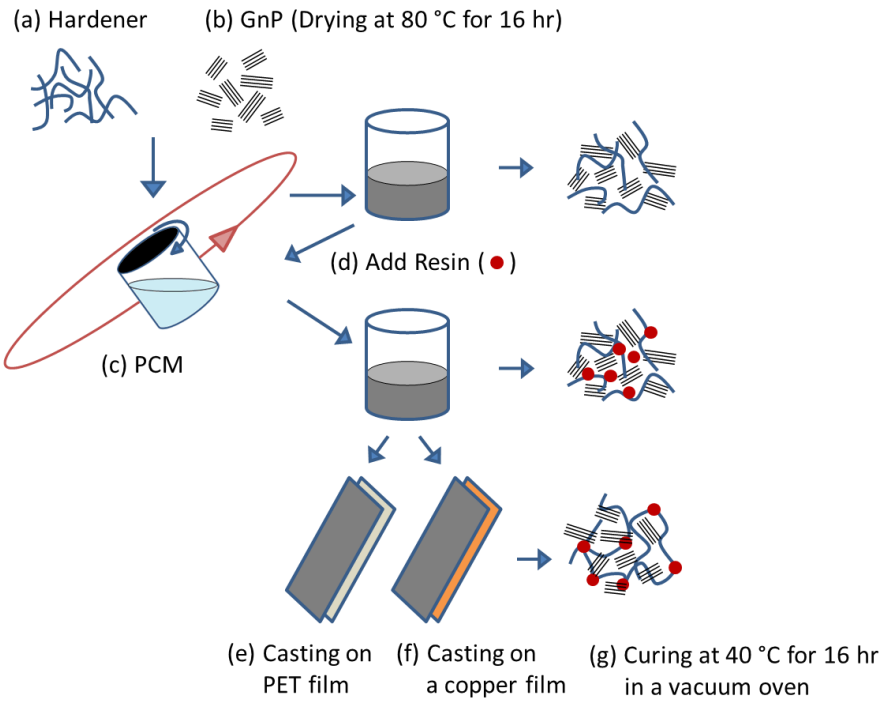

Figure 4.1. A schematic illustration for the fabrication of PU/GnP nanocomposites and casting on PET and Cu substrates.

4.2.3 Characterizations

4.2.3.1 Structure and morphology

Samples were characterized by XRD (Rigaku, Miniflex 600) using Cu-Kα radiation (λ = 1.54184 nm). The samples were scanned from 2θ = 1° to 80° at a rate of 1 °/min. The acquired spectra were used to calculate the crystallite size (τ) of GnP, based on the Debye-Scherrer equation (equation 4-1)[125]:

$$\tau = \frac{K\lambda}{\beta \cos\theta} \tag{4-1}$$

where β is the full width at half maximum (FWHM, radian), λ is the radiation wavelength used for measurement, K is the shape constant of 0.947 and θ is the diffraction angle. The relative size of

the GnP was obtained from the calculations and compared with the reported values of each grade of GnP.

The morphology of GnP and PU/GnP nanocomposites was characterized by the SEM (Zeiss Leo 1550). A cross-sectional sample of the PU/GnP nanocomposites for SEM was prepared by cryogenic rupture using liquid nitrogen, with samples being gold-sputtered prior to imaging.

4.2.3.2 Electrochemical properties

Electrochemical properties of PU/GnP nanocomposites were measured using the standard corrosion cell consisting of a circular Teflon sample holder in a double-jacketed glass cell (1L). The corrosion cell contained a three-electrode system that consisted of a coated or uncoated Cu disk specimen (Area: 1 cm^2) assigned as a working electrode (WE), two graphite rods as a counter electrode (CE), and an Ag/AgCl electrode as a reference electrode (RE). Figure 4.2 illustrates the Cu specimens, including the pristine Cu and the coated Cu with the PU/GnP nanocomposites. The film on the Cu showed a different color depending on the grade of GnP. The PU/GnP film containing H100 showed the sporadic dispersion of GnP owing to the large size of H100, while the PU/GnP containing M5 and C750 showed relatively uniform dispersions of GnP.

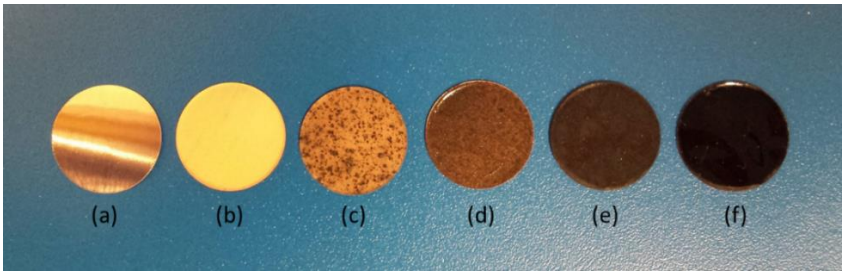

Figure 4.2. Specimen images of PU/GnP samples for electrochemical measurement: (a) Cu disk (bare), (b) PU (pristine) on Cu, (c) PU/H100 on Cu, (d) PU/M25 on Cu, (e) PU/M5 on Cu, and (f) PU/C750 on Cu. (GnP loading for all nanocomposites: 1 wt%).

Deionized water cleaned the corrosion sample and dried before mounting the sample holder. The double-jacketed glass cell was filled with 3.5 wt% NaCl electrolyte solution at room temperature. The electrochemical analysis was conducted using the VSP-300 workstation (Uniscan instrument Ltd., Claix, France), where each measurement was repeated five times for a reproducibility. Measurement data was analyzed using EC-Lab software (Bio-Logic).

The WE was stabilized for 3-4 hours to minimize the fluctuation of the potential before performing the measurement, followed by electrochemical impedance spectroscopy (EIS) or cyclic voltammetry (CV). EIS was conducted in a frequency range from 100 kHz to 200 Hz to obtain Nyquist and Bode plots. CV was conducted to obtain Tafel polarization curves by scanning at a rate of 20 mV/min in the potential range from -500 mV to 500 mV. The Tafel plot was used to determine the corrosion current (I_{corr}) by extrapolating the linear portion of the anodic and cathodic curves using the EC-Lab software.

The corrosion rate (R_{corr}), in units of mils per year (MPY) was determined by the following equation 4-2 as described in the ASTM standard G102:[126]

$$R_{corr} = \frac{0.13 \times I_{corr} \times EW}{A \times \rho} \tag{4-2}$$

where EW is the equivalent weight of a copper (31.7 g), ρ is the density of the copper (8.97 g/cm^3), and A is the surface area of the sample (1 cm^2).

4.2.3.3 Mechanical properties

Mechanical properties of PU/GnP nanocomposites were characterized by universal testing machine (UTM) eXpert 7603 (Load cell: 4.4 kN, ADMET, USA) at room temperature at a crosshead rate of 100 mm/min. Five samples, fabricated with a length of 75 mm, a thickness of

300 μm, and a parallel length of 30 mm, were measured based on ASTM D638. Tensile modulus was calculated by the initial linear slope of the entire stress-strain curve, tensile strength corresponded with the maximum strength, and elongation at the break was determined by strain at sample fracture.

4.3 Results and Discussion

4.3.1 Morphology and structure of GnP

SEM images of the four different grades of pristine GnP are illustrated in Figure 4.3 under the identical magnification for the exact comparison of GnP size. The images reveal that the diameter of each GnP matches the reported average diameter from the manufacturer, while the actual size distribution of the samples is broad in appearance. Nevertheless, the SEM images show the distinct differences in size, especially for the average diameter between the four grades of GnP.

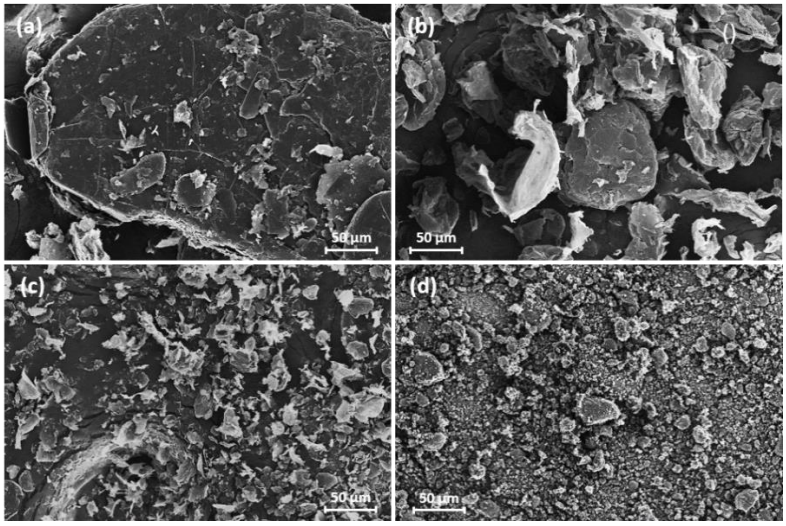

Figure 4.3. SEM images for different grades of GnP: (a) xGnP H100, (b) xGnP M25, (c) xGnP M5, and (d) xGnP C750.

An XRD spectrum of each GnP is presented in Figure 4.4, and the calculated parameters of the GnP from the XRD spectra are summarized in Table 4.2. The three grades of GnP (excluding C750) show a comparable XRD spectrum in terms of the position and breadth of the peak ($2\theta = 26°$). The d-spacing, or interlayer distance between graphene sheets, was calculated to be 3.35 ~ 3.38 Å for the three grades using Bragg's equation. The number of graphene layers, indicative of the crystallite size of the GnP, was calculated as 62 (H100), 56 (M25), and 58 (M5), respectively. On the other hand, C750 shows a relatively broad spectrum and low intensity when compared to the other three grades of GnP, and the number of layers calculated to be 13. For this reason, the aspect ratio, defined as the ratio of the average diameter (D) and the thickness of GnP (L), is not proportional to the diameter of GnP, especially for C750 and M5. The reason being that the number of layers for C750 is considerably lower than M5 but the difference of diameter between C750 and M5 is not relatively significant. Additionally, the bulk density of C750 was considerably larger than the other grades of GnP. Due to the higher bulk density and less number of layers of C750, a greater number of particles can be dispersed in a unit volume at the same sample weight of GnP. Therefore, it can be assumed that a higher degree of dispersion is relatively achievable with C750 compared with other grades of GnP.

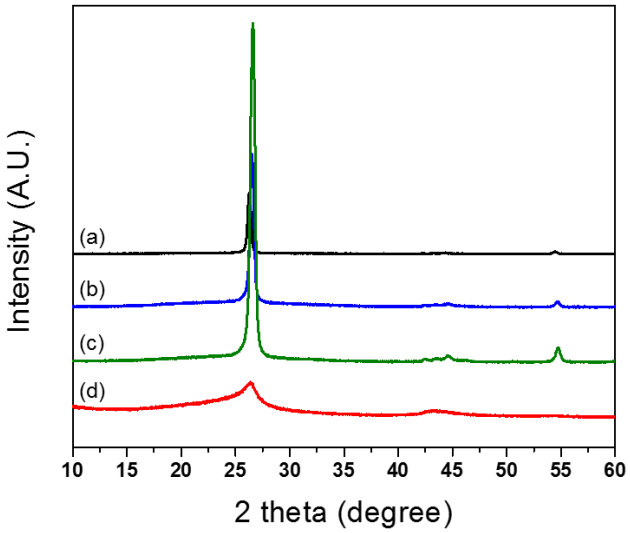

Figure 4.4. XRD spectrum for the four commercial grades of GnP: (a) xGnP H100, (b) xGnP M25, (c) xGnP M5, and (d) xGnP C750.

Table 4.2. Parameters extracted from XRD spectrum

Grade	FWHM (rad, × 10^{-3})	d-spacing (Å)	Number of graphene layers	Aspect ratio (D/L)
H-100	6.76	3.38	62	4032.3
M-25	7.54	3.36	56	1116.1
M-5	7.31	3.35	58	215.5
C-750	33.12	3.37	13	384.6

4.3.2 Electrochemical properties

Cyclic Voltammetry (CV) is widely used to quantify the anti-corrosion performance of a coated or uncoated metal substrate. In general, a Tafel polarization curve can be obtained by CV measurement, with the curve providing a value to quantify the anti-corrosion performance of a material. The Tafel polarization curve is described by the relationship between a potential and

current, allowing the anti-corrosion performance of the material to be evaluated by the values. For instance, higher potential and lower current value correspond with high anti-corrosion performance. Figure 4.5 illustrates Tafel plots for bare Cu and the Cu coated with PU and the PU/GnP nanocomposites.

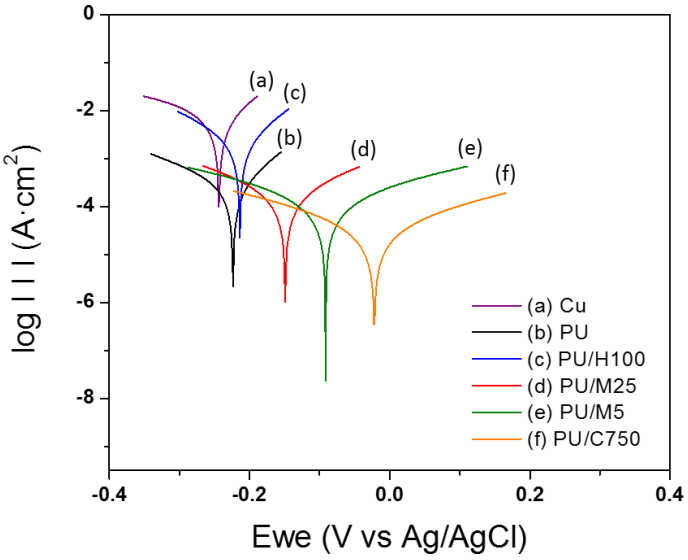

Figure 4.5. Tafel plots for (a) Cu (bare), (b) PU (pristine) on Cu, (c) PU/H100 on Cu, (d) PU/M25 on Cu, (e) PU/M5 on Cu, and (f) PU/C750 on Cu. (GnP loading: 1 wt%).

The plots reveal that PU/GnP including the smaller diameter of GnP shifts the polarization curve to the direction of a larger potential and a smaller current. This means that the smaller diameter of GnP in the nanocomposites improves the anti-corrosion performance of PU/GnP. In addition, the Tafel plot provides significant parameters such as corrosion potential (E_{corr}) and corrosion current (I_{corr}) to quantify the anti-corrosion performance of the composites. The parameters are determined by the point of intersection between extrapolated cathodic and anodic curves. Furthermore, R_p, polarization resistance is calculated by using the Stern-Geary equation (equation 3-3 in chapter 3).[111] In this equation, a smaller R_p value represents a higher anti-corrosion performance due to

the value of lower I_{corr}. All calculated parameters are shown in Table 4.3.

Table 4.3. Electrochemical parameters from potentiodynamic measurements.

Samples	E_{corr} (mV vs. Ag/AgCl)	I_{corr} ($\mu A/cm^2$)	b_a (mV/dec)	b_c (mV/dec)	R_p ($\Omega \cdot cm^2$)	R_{corr} (MPY)	P_{EF} (%)
Cu	-243.5	6.37	113.1	99.9	3.6	5.71	-
PU	-223.6	0.31	99.5	132.8	79.2	0.14	97.5
PU/H100	-213.8	2.47	103.7	146.3	10.7	1.13	80.3
PU/M25	-149.0	0.24	214.3	235.4	199.6	0.11	98.1
PU/M5	-91.6	0.12	354.7	356.2	389.8	0.09	98.4
PU/C750	-22.0	0.05	388.3	384.4	1747.5	0.02	99.6

The results show that as the size of GnP decreases, E_{corr} increases while I_{corr} decreases. This means that the smaller diameter of GnP requires a higher corrosion potential to corrode the Cu substrate, but a lower current is detected in the potentiodynamic electrochemical system. However, it should be noted that the I_{corr} value of PU/H100 (2.47 $\mu A/cm^2$) is higher than the pristine PU (0.31 $\mu A/cm^2$), resulting in a lower R_p value (10.7 $\Omega \cdot cm^2$) and a higher R_{corr} (1.13 MPY). This unexpected variation is likely due to the thickness of the PU/H100 layer on the Cu substrate. For instance, Qi et al. reported that the lower thickness of the film led to a higher corrosion current with an unchanged corrosion potential.[28] However, PU/H100 was cast on the Cu substrate with the same thickness as the pristine PU (300 μm). For this reason, it can be assumed that there is another reason behind the cause of the reduction of the thickness of the cast film such as a crevice on the film surface.

One description for the reason is that large agglomerates of H100 on the surface of the cast film,

which had the appearance of the black dot, are able to be considered. The average diameter of H100 was revealed to be 150 μm by SEM observation, thus, the entire size of the agglomerate is larger than at least 150 μm. On the other hand, the cast film has a thickness of around 300 μm, and, as a result, it can be assumed that some agglomerates can build a crack or crevice on the cast film and the defects on the film are able to have an effect by decreasing I_{corr}. This is because the black dots can provide a pathway at which a corrosive agent is easy to permeate into the film inside. Essentially, this phenomenon can result in decreasing the permeation rate of the agent same as reducing the thickness of the cast film. This issue will be discussed in further detail in the section of SEM.

The protection efficiency (P_{EF})[111] obtained from the Tafel plot is also widely used as a metric to evaluate the anti-corrosion performance of a protective layer on a metal substrate and is given by equation 4-4:

$$P_{EF}[\%] = \left(1 - \frac{I_{corr}}{I^{\circ}_{corr}}\right) \times 100 \tag{4-4}$$

where I°_{corr} represents the corrosion current of the pristine PU. Table 4.3 also illustrates that P_{EF} increases by incorporating smaller diameters of GnP in the PU/GnP layer, indicating that the anti-corrosion performance of PU/GnP is enhanced with smaller sizes of GnP. However, the P_{EF} value of the PU/H100 nanocomposite is lower than that of the pristine PU due to its relatively higher I_{corr} value.

Further, EIS was also used to quantify the anti-corrosive performance. Firstly, EIS measurement requires an appropriate equivalent circuit model to be built up in order to match an acquired impedance data. Equivalent circuit models for bare Cu and film-coated Cu substrate are suggested

in Figure 4.6,[126]

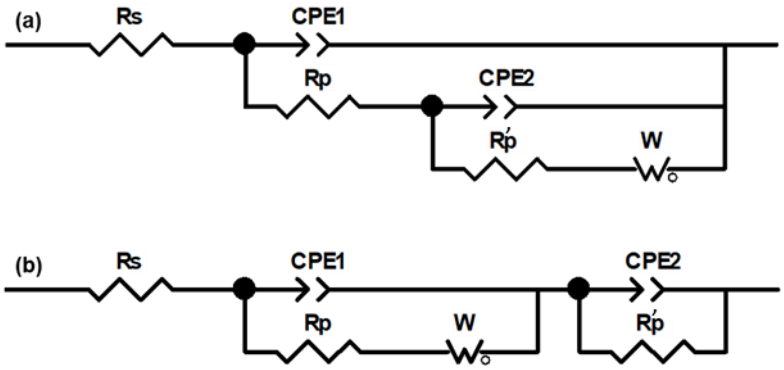

Figure 4.6. Equivalent circuit model for matching with the electrochemical impedance data: (a) bare Cu and (b) film coated Cu substrate in NaCl solution (3.5 wt%).

where R_s is the solution resistance, R_p is the polarization resistance of a coating layer associated with the charge-transfer resistance, CPE1 and CPE2 are the constant phase elements, R'_p is another polarization resistance, and W is the Warburg diffusion. Figure 4.7 illustrates the Nyquist plots for bare Cu substrate and PU/GnP on Cu.

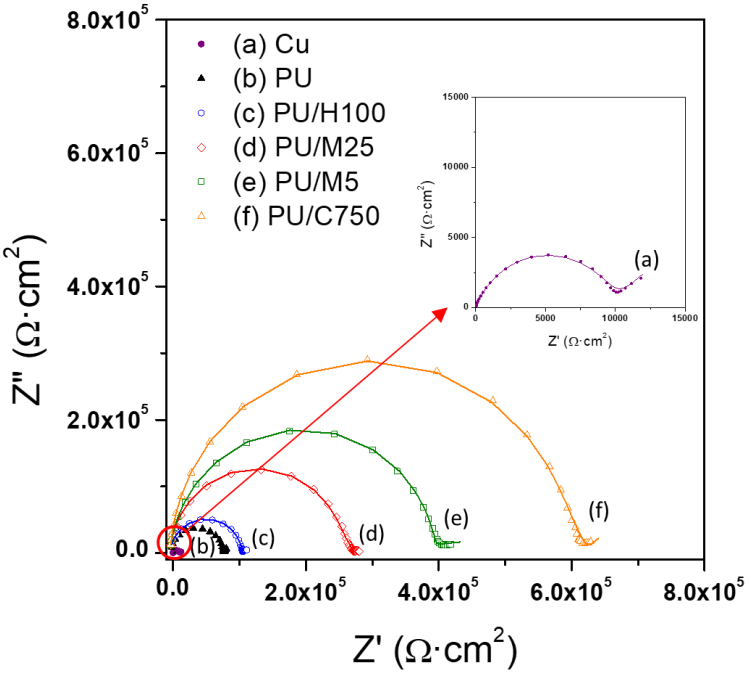

Figure 4.7. Nyquist plots (dotted lines: measured data, solid lines: fitting model) for (a) Cu (bare), (b) PU (pristine) on Cu, (c) PU/H100 on Cu, (d) PU/M25 on Cu, (e) PU/M5 on Cu, and (f) PU/C750 on Cu (GnP loading for all samples: 1 wt%).

In Figure 4.7, the dotted line represents the measured EIS data and the solid line represents fitting results with the equivalent circuit model, with the two lines being well fitted with each other.[126] The point of interest in these Nyquist plots is the diameter of the semicircle. In general, a larger semicircle diameter corresponds with a higher resistance, which is inversely proportional to I_{corr}, indicating high anti-corrosion performance.[107] In Figure 4.7, the EIS spectrum of the bare Cu substrate shows the typical curve,[127] with the semicircle size at the low-frequency end being 10.2 kΩ·cm^2. The pristine PU on Cu shows a larger semicircle as the value of 77.8 kΩ·cm^2 than the bare Cu, meaning that the anti-corrosion performance of the Cu substrate is improved by the PU layer alone. However, the PU/GnP composites show much larger semicircles than the pristine PU and, thus GnP highly contributes to the improvement of the anti-corrosion performance of the

composites. Furthermore, PU/GnP with the smaller size of GnP shows the larger diameter of the semicircle in the Nyquist plot, causing the semicircle diameter of the PU/GnP composites to increase from 104.8 kΩ·cm^2 to 616.6 kΩ·cm^2 by a decrease of GnP size. However, the semicircle diameter of PU/H100 is almost similar to that of the pristine PU, which is in line with the CV measurement.

Specific values consisting of the equivalent circuit in Figure 4.6 are shown in Table 4.4 based on fitting the equivalent circuit model with the acquired EIS data. Among the specific values, protection efficiency (P'_{EF}) can be also calculated from R_p, which represents the polarization resistance of the coating layer as follows in equation 4-5:[127]

$$P'_{EF}(\%) = \left(1 - \frac{R_p^{\circ}}{R_p}\right) \times 100 \tag{4-5}$$

where R°_p is the polarization resistance of the Cu substrate. The P'_{EF} value of the pristine PU is 88.1%, and the value increases under the existence of GnP, with an even smaller diameter of GnP in the composites showing a higher P'_{EF} of up to 98.7%. These results are in accordance with the results from potentiodynamic measurement (Cyclic Voltammetry) in Table 4.3. As a result, the two tendencies from EIS and CV show that GnP plays a significant role in reducing a corrosion of the composites and that a smaller diameter of GnP can be more effective to prevent the corrosion.

Table 4.4. Equivalent circuit parameters fitting with the acquired data from EIS measurements

Samples	R_s ($\Omega \cdot cm^2$)	R_p ($\Omega \cdot cm^2$)	CPE1 ($\Omega^{-1} \cdot S^{n1} \cdot cm^{-2}$)	n1	R'_p ($\Omega \cdot cm^2$)	CPE2 ($\Omega^{-1} \cdot S^{n2} \cdot cm^2$)	n2	W ($\Omega^{-1} \cdot S^{n1} \cdot cm^{-2}$)	P'_{EF} (%)
Cu	7.3E+01	8.5E+03	9.55E-06	0.97	2.6E+02	3.9E-03	0.50	8.5E+00	
PU	6.6E+01	7.2E+04	1.01E-10	1.00	1.0E+03	1.0E-09	0.94	3.1E+01	88.1
PU/H100	8.3E+01	9.3E+04	1.30E-10	0.96	1.9E+02	2.1E-10	0.91	4.1E+00	90.8
PU/M25	8.7E+01	3.2E+05	2.92E-10	0.90	5.6E+02	8.5E-09	0.37	1.3E+02	97.3
PU/M5	8.3E+01	4.1E+05	2.02E-10	0.91	8.6E+03	2.3E-10	0.52	2.4E+02	97.9
PU/C750	1.5E+02	6.5E+05	1.88E-10	0.92	1.7E+04	2.6E-10	0.20	1.0E+03	98.7

To supplement the Nyquist plot, Bode plot was also used to compare the anti-corrosion performance of the PU/GnP composites. Figure 4.8 illustrates the Bode plot (a) and phase plot (b) for the bare Cu and PU/GnP on Cu. In Figure 4.8 (a), the Z' value (real part of impedance) at the lowest frequency represents the anti-corrosion performance. Thus, the larger value of Z' leads to a smaller I_{corr} and a higher performance. The Bode plot shows the distinct tendency for smaller sizes of GnP in the composite to produce higher Z' values at the lowest frequency.[107, 126] PU/H100 shows a slightly lower Z' value (5.09 $\Omega.cm^2$) than the pristine PU (5.14 $\Omega.cm^2$), however, the Z' value difference between PU/H100 and the pristine PU is not large enough to discuss as the difference of the anti-corrosion performance of them. As a result, the Bode plot also confirms that the addition of H100 does not contribute significantly to improving the anti-corrosion performance of the composite rather than the pristine PU.

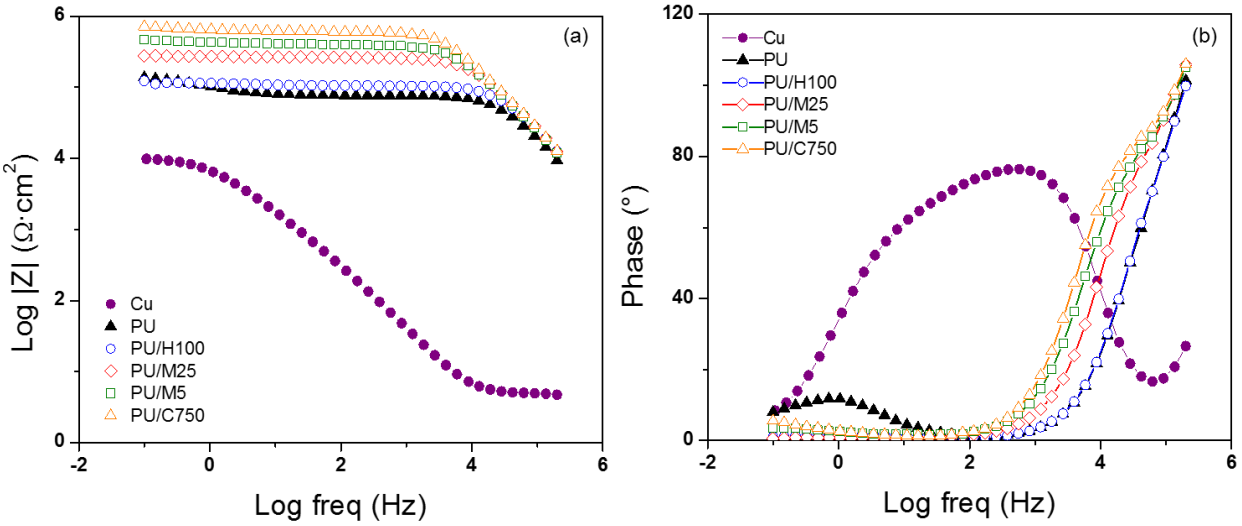

Figure 4.8. Bode (a) and phase (b) plots for pristine Cu, pristine PU, PU/H100, PU/M25, PU/M5, and PU/C750 on Cu (GnP loading for all samples: 1 wt%).

As a result, the anti-corrosion performance of the composites is definitely improved by decreasing GnP size, whereas H100, the largest size of GnP, does not follow this trend. It is assumed that these results are related to the phenomenon due to a large particle which is coagulated by H100 as mentioned above.

4.3.3 Mechanical properties of PU/GnP composites

Figure 4.9 (a) presents the stress-strain curves of the pristine PU and the PU/GnP nanocomposites with a GnP loading of 1 wt%. The tensile modulus of the pristine PU corresponds with 0.85 MPa from the initial linear slope of the curve. On the other hand, the PU nanocomposites with 1 wt% of GnP show a slightly steeper initial slope than the slope of the pristine PU which means that a stiffness of PU/GnP nanocomposites is higher than the neat PU. However, tensile strength and elongation at the break decrease for all nanocomposites including GnP in this figure. Tensile modulus comparison of the PU/GnP nanocomposites in 1 wt% is shown in Figure 4.9 (b).

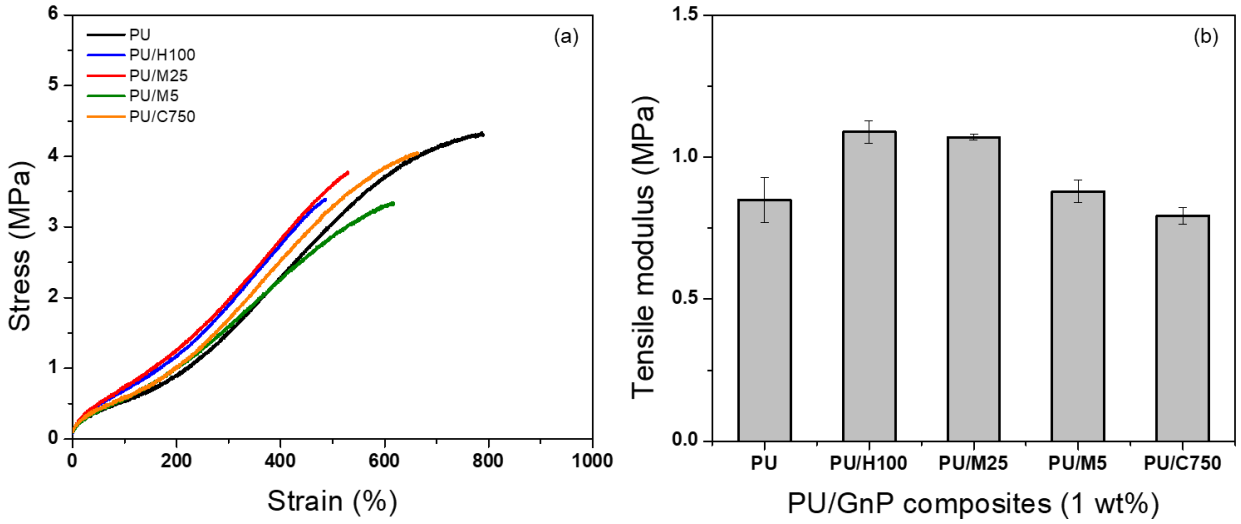

Figure 4.9. Strain-Stress (SS) curves of the PU/GnP nanocomposites at (a) 1 wt% GnP loading and (b) comparison of tensile modulus for the 1 wt% composites of PU/GnP. (The error bars in Figure 4.9 (b) present standard deviations (n=5)).

In Figure 4.9 (b), PU/H100 has the highest tensile modulus, but PU/C750 has the lowest value. This means that tensile modulus of PU/GnP is likely to be proportional to the diameter of GnP. In addition to the comparison, specific values of mechanical properties for the 1 wt% nanocomposites are shown in Table 4.5, respectively. As briefly mentioned above, tensile strength and elongation at break of the PU/GnP nanocomposites show relatively lower values than the pristine PU which means that the existence of GnP causes reduction of the elongation of the composites and the elongation associates with the tensile strength. This is a general tendency in terms of a polymer nanocomposite including an inorganic filler and it can be explained by an interfacial adhesion theory and the dispersion or an agglomerate of GnP as other studies.[118-120, 128] It is assumed that, if the interfacial adhesion between the PU matrix and the surface of GnP is insufficient, external stress will not uniformly transfer throughout the whole nanocomposite. Herein, van der Waals force between the GnP layers can suppress the stress transfer in the nanocomposite as

well.[35, 129] In addition, inferior dispersion on the agglomerate of GnP can cause a defect in the nanocomposite. For this reason, a lack of strong interfacial adhesion and dispersion or aggregates of GnP often result in early rupture of the tensile specimen during the extension process. To improve the interfacial interaction between PU and GnP, numerous researchers have suggested a chemical treatment of the surface of GnP.[130, 131] However, this study primarily focuses on the effect of GnP size in the PU/GnP nanocomposites. Thus, functionalization of GnP will be studied in the future for improvement of mechanical properties of PU/GnP.

Therefore, in this study, it can be summarized that tensile strength and elongation at the break of PU/GnP are not improved by adding GnP due to the deficient interfacial adhesion between PU and GnP. However, tensile modulus which occurs in the small range of extension is partially improved by the addition of GnP.

Table 4.5. Mechanical properties of PU/GnP nanocomposites

Samples	Contents of GnP (wt%)	Tensile Modulus (MPa)	Tensile Strength (MPa)	Elongation at break (%)
Neat PU	-	0.85 ± 0.08	4.3 ± 0.3	926
PU/H100	1	1.09 ± 0.04	3.1 ± 0.3	494
PU/M25	1	1.07 ± 0.01	3.6 ± 0.2	530
PU/M5	1	0.88 ± 0.04	3.2 ± 0.2	624
PU/C750	1	0.79 ± 0.03	4.1 ± 0.1	782

4.3.4 Morphology of PU/GnP nanocomposites

Figure 4.10 shows the cross-sectional morphology of PU/GnP nanocomposites with a loading of 1 wt% using SEM. Each type of GnP is readily dispersed in PU and shows their intrinsic size. In

Figure 4.10a, the thickness of H100 seems to be particularly thicker than other GnPs. This phenomenon seems to be due to the inferior dispersion and aggregation of H100 compared to other nanocomposites. For instance, PU/M25 nanocomposite in Figure 4.10b seems to show relatively better dispersion and less agglomeration of GnP than PU/H100 though M25 is the second largest GnP. On the other hand, the small GnPs, such as M5 and C750, are not only well dispersed within the polymer matrix but also the detached layers within GnP are not observed. Based on this observation, it can be assumed that the larger size of GnP is difficult to be well dispersed into the polymer matrix and is easy to be aggregated each other. Thus, the larger GnP, such as H100, occupies a larger domain in the polymer matrix. Therefore, a smaller number of GnP particles are distributed in the composites under the same loading of GnP. This dispersion regarding the large GnP, which has a greater number of graphene layers such as H100 and M25, can influence to reduce mechanical properties and anti-corrosion performance of the nanocomposite. Furthermore, Figure 4.11 reveals that PU/H100 shows a void between the PU matrix and GnP near the surface of the film. This void should be caused by the inferior dispersion and aggregation of H100. The void can allow a corrosive agent to diffuse into PU/H100 nanocomposite from the surface easily. For this reason, large H100 particles or agglomerates are likely to reduce the anti-corrosion performance of the PU/GnP layer because as the corrosive agents pass through the voids, the path length for the corrosive agent is reduced. However, PU/M5 and PU/C750 show a uniform dispersion of GnP in the PU matrix without voids. Therefore, small GnPs are likely to provide a relatively more efficient pathway which can suppress the penetration of corrosive agents than large GnPs. Furthermore, the voids generated due to large GnPs can also reduce the mechanical properties of PU/GnP since the strength of interfacial adhesion is proportional to the contact area among PU and GnP. As a result, the PU/H100 nanocomposite shows the lowest value of elongation

at the break among the composites. Figure 4.12 depicts a schematic mechanism for the size effect of GnP with regards to the anti-corrosion performance of PU/GnP. This figure suggests that the smaller GnPs (i.e. smaller average diameter) are well-dispersed within the composites and provide more effective pathway to prevent diffusion of the corrosive agent. Thus, the time taken for the corrosive agent to reach the Cu substrate is extended.

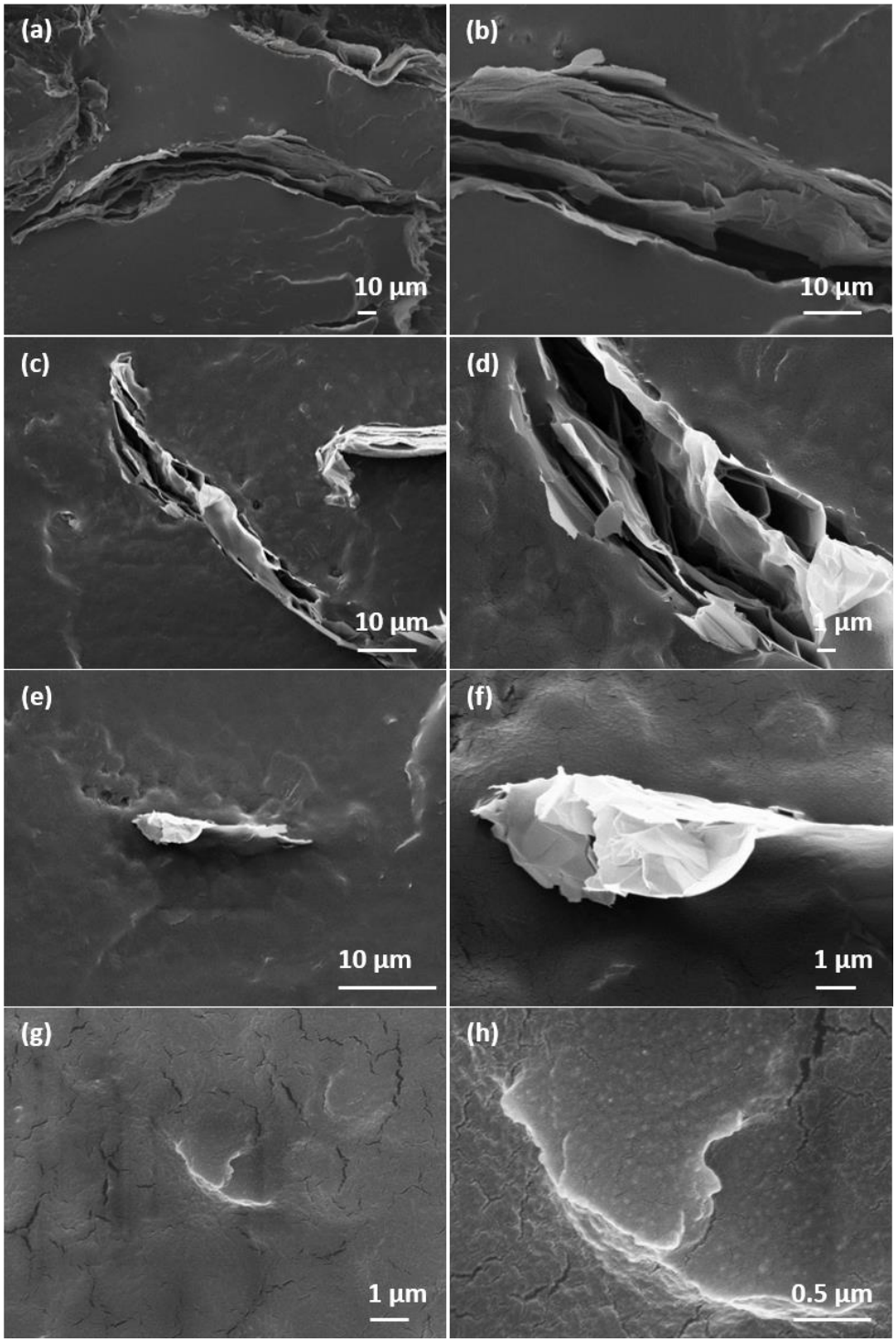

Figure 4.10. Cross-sectional SEM images for the PU/GnP nanocomposites (1 wt% GnP loading, (a)~(d): Low magnification, (e)~(f): High magnification): (a) and (e) PU/H100, (b) and (f) PU/M25, (c) and (g) PU/M5, and (d) and (h) PU/C750.

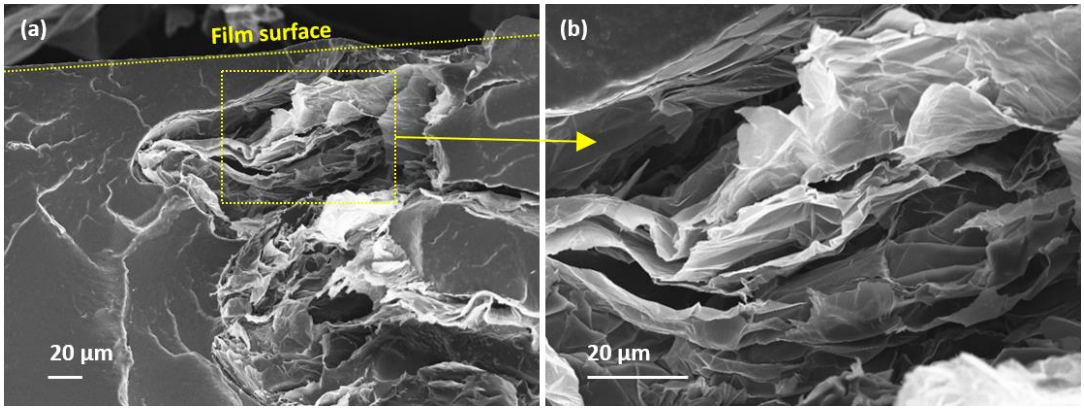

Figure 4.11. Cross-sectional SEM images for the surface of the PU/H100 nanocomposite.

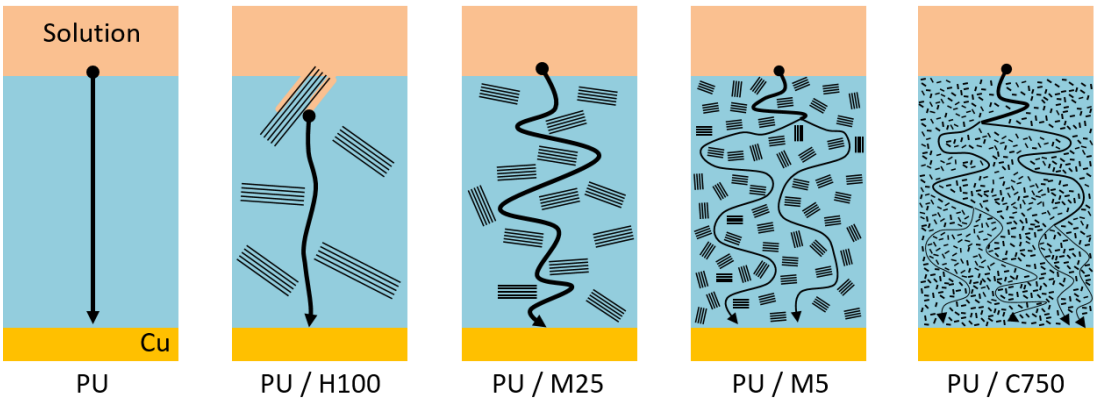

Figure 4.12. Schematic model for the permeation of the corrosive agent (•) passing through the coating layer of the PU nanocomposite containing 1 wt% GnP.

4.4 Conclusion

Four different commercial GnP (H100, M25, M5, and C750) were used to fabricate PU/GnP composites. The four GnP had the average diameter from under 2 μm to 100 μm, and this difference of the diameter provided the distinct size comparison of GnP in the PU/GnP nanocomposites. Electrochemical, mechanical, and morphological properties of nanocomposites were thoroughly investigated by the average diameter of the four GnP. The anti-corrosion performance against the

corrosive agents was improved by the incorporation of GnP into the PU matrix, and this effect could be amplified with the smaller size of GnP. Specifically, the PU/C750 nanocomposite, which has the smallest diameter of GnP, indicated the highest E_{corr} of -22.0 mV and the lowest I_{corr} of 0.05 μA/cm^2. Protection efficiency (P_{EF}) of PU/C750 increased up to 99.6 % from 97.5 % of the neat PU. This improvement can be explained by that C750 more uniformly dispersed within the PU matrix than other GnP. The uniform dispersion of C750 resulted in forming a complicated pathway in the PU/GnP nanocomposites to suppress the diffusion of corrosive agents. Whereas, PU/H100 nanocomposite indicated lower P_{EF} of 80.3 % than the neat PU. The large H100 led to a surface failure due to a coagulation of H100 and this failure resulted in a decrease of P_{EF} value of the nanocomposite. These phenomena were supported by the morphological properties of the nanocomposites. In mechanical properties, the PU/H100 nanocomposites, which has the largest diameter of GnP, indicated the improved tensile modulus up to 28 % than the neat PU. However, the small GnP, such as M5 and C750, were not effective to improve the overall mechanical properties of the PU nanocomposites. It seems that the high aspect ratio of H100 (e.g. 4032.3) only contributed to improving the tensile modulus, which is a small range deformation of the nanocomposites. Nevertheless, the insufficient interfacial adhesion between GnP and the PU matrix resulted in decreasing the overall mechanical properties of the PU/GnP nanocomposites. In chapter 5, graphene oxide (GO), which has hydrophilic functional groups, will be investigated to increase the interfacial interaction between graphene and the PU matrix due to hydrophilic functional groups on graphene. In addition, mechanical and anti-corrosion properties of the PU/GO composites will be compared with the PU/GnP composites.

5. Engineering investigation for the size effect of graphene oxide derived from graphene nanoplatelets in polyurethane nanocomposites

This chapter is reprinted form from the article below. Permission was obtained from Wiley.

Jun Geun Um, Yun-Seok Jun, Ali Elkamel, and Aiping Yu. “Engineering investigation for the size effect of graphene oxide derived from graphene nanoplatelets in polyurethane nanocomposites”, *The Canadian Journal of Chemical Engineering*, 2020. 1, 1.

In chapter 4, four different commercial of GnP were used to fabricate the PU nanocomposites via planetary centrifugal mixing. Anti-corrosion performance and mechanical properties of the nanocomposites were thoroughly investigated. The average diameter of GnP was crucial to the anti-corrosion performance of the nanocomposites. The PU nanocomposite containing the small GnP (C750) with diameter of under 2 μm, protected the metal surface from corrosive agents more effective than the one with the large GnP (H100) around 100 μm diameter. This improvement of PU/C750 was attributed to the uniform dispersion of C750 in the PU matrix, and the dispersion built a complicated pathway to suppress the diffusion of the corrosive agents. The tensile modulus of PU/C750 was not improved while PU/H100 indicated enhancement compared to other nanocomposites due to the high aspect ratio. However, the overall mechanical properties of the PU/GnP nanocomposites were not improved due to the insufficient interfacial adhesion between GnP and the PU matrix. This is because PU polymer chain and the graphene surface are not compatible. The surface of GnP might need to be modified as being compatible with the PU matrix in order to improve the mechanical properties of nanocomposites. This is because external stress would be more uniformly distributed by the interfacial interaction between GnP and the PU matrix.

The overall mechanical properties of PU/GnP could be enhanced by this effect. In this chapter, graphene oxide (GO) will be derived from GnP in chapter 4 to improve the interfacial interaction. GO has many hydrophilic functional groups such as hydroxyl (-OH), carboxylic (-COO), and epoxy (C-O-C). These functional groups would form a physical interfacial interaction with the PU matrix such as hydrogen boning. For this objective, two different GO were synthesized from the two GnP in chapter 4, which have two different diameters of 25 μm and under 2 μm, respectively. In this chapter, the mechanical properties and anti-corrosion performance of PU/GO nanocomposites were thoroughly investigated in comparison to the PU/GnP nanocomposites.

5.1 Introduction

In the field of polymer nanocomposites, graphene has been studied as one of the most appealing fillers to reinforce deficient characteristics of polymeric materials, such as mechanical and gas barrier properties.[3, 37, 132-137] Graphene possesses many favorable characteristics such as remarkable mechanical strength and high thermoelectric conductivity, and these have led to its use in numerous applications within the field of polymer nanocomposites such as electronic devices, sensors, energy storage, and protection coating area.[107, 110, 118, 128, 138-140] In addition, the high surface area of graphene has proved that the properties of the nanocomposites have the potential to be maximized when graphene fillers are uniformly dispersed in the polymer matrix.[141-144] Meaningful achievements with regards to the reinforcement effect of graphene in polymer nanocomposites have been reported by several researchers. For instance, Jun et al.[145] reported that polypropylene (PP) incorporated with various sizes of graphene nanoplatelets (GnP) showed highly enhanced thermal stability in the nanocomposite. The report explained this effect was due to the small size of the fillers contributing to the uniform distribution within the matrix and prevent the aggregation of GnP (up to 20 wt%). In another study, Rafiee et al.[141] reported

that graphene platelets in epoxy nanocomposites improved the elastic modulus and tensile strength of the nanocomposite by 31% and 40%, respectively, while showing a 53% increase in fracture toughness.

The main challenge in the fabrication of graphene nanocomposites lies in the dispersion of graphene into the polymer matrix. This is due to the fact that graphene easily binds with itself to form a layered structure by van der Waals forces.[3, 133, 134, 136, 146] Layered graphene usually consists of a few layers to as many as several dozen layers of graphene and therefore the structure is not easy to delaminate by shear force caused by polymer processing. Moreover, the GnP's van der Waals forces are stronger than the interaction between GnP and the polymer matrix, and this results in the agglomeration of the fillers and the formation of independent phases of GnP within the polymer matrix.[147, 148]

Alternatively, graphene oxide (GO) has been used for manipulating the uniform dispersion of graphene into a polymer matrix. GO is an oxidized form of graphene, and thus it includes massive oxygen functional groups such as epoxides, alcohols, ketones, carbonyl, and carboxylic groups on the plane and edge of the graphene sheet.[3, 31, 37, 132, 133, 136, 149] For the synthesis of GO, the Hummers' method is generally used to oxidize graphene; however, an improved Hummers' method suggested by J. M. Tour is widely used to achieve the greater oxidized GO than the typically synthesized GO.[150] Unfortunately, the strong hydrophilicity of GO can be a challenge in preparing polymer composites involving the exfoliated layers of GO.[151] Due to the hydrophilicity, GO can build a uniform suspension state in water or hydrophilic organic solvents such as dimethylformamide (DMF) or tetrahydrofuran (THF).[152] The dispersion uniformity of GO in these solvents can allow structural compatibility with a hydrophilic polymer without the agglomeration of the filler. For instance, Zhao et al.[153] reported that the mechanical properties

of poly(vinyl alcohol) (PVA) were significantly improved by the incorporation of GO. The nanocomposites had a tensile strength improvement of 150% and 10 times higher elastic modulus than the pristine PVA at a GO content of 1.8 vol%. In addition, Putz et al.[154] showed the uniform dispersion of GO in hydrophobic poly(methyl methacrylate) (PMMA); they overcame the incompatibility between GO and PMMA using the hydrophilic solvent DMF. In this case, the PMMA/GO nanocomposites indicated limited improvement in the mechanical properties; however, it showcased the feasibility of using the hydrophilic solvent to compound the hydrophobic polymer with GO. In that regard, the strong hydrophilicity of GO has the advantage of enhancing the overall properties of the nanocomposites in a hydrophilic polymer; however, hydrophilic solvents such as water are still required to fabricate the nanocomposite.

In this study, we present a comparison of GO and GnP in polyurethane (PU) nanocomposites and the size effect of GO on the mechanical property and anti-corrosion performance. Two different sizes of GnP were used for GO synthesis; the grade of xGnP M25 (M25) had 25 μm of average diameter, while the grade of xGnP C750 (C750) had under 2 μm of average diameter. They are both available on the commercial market. In addition, a commercial PU was used for more practical research. Two different sizes of GO were synthesized by the improved Hummers' method; GO-M25 was from M25 and GO-C750 was from C750. The low content of GO (0.1 wt%-0.5 wt%) within the nanocomposites were selected to design an efficient filler content for mechanically and electrochemically enhanced nanocomposites. The PU nanocomposites were fabricated via GO dispersion in THF and their mechanical property, anti-corrosion performance, and morphological property were characterized by various analyzing methods.

5.2 Experimental

5.2.1 Materials

The two types of GnP purchased from XG science (US) were used to form graphene oxide. In this study, xGnP M25 (M25) and xGnP C750 (C750) grades were chosen to compare the size effect in polymer composites. According to the technical data from the manufacturer, the average diameters of M25 and C750 were 25 μm and under 2 μm, respectively, and the surface areas of M25 and C750 were ~ 120 m^2/g and 750 m^2/g, respectively. The densities of the two grades were the same as 2.2 g/cm^3. Commercial PU, Rencast 6401 (Huntsman, US) was used as the matrix polymer. Rencast 6401 is widely used as the material in the field requiring the highly flexible and anti-abrasive properties. Rencast 6401 comprises two liquids, resin and hardener. The main component of the resin is *4,4'*-Methylene diphenyl diisocyanate (MDI) and the hardener includes oxyalkylene polymer (ie, polyol) and 1,4 butanediol as a chain extender. Based on the data from the manufacturer, the mixing ratio of the resin and hardener was 25:100 by mass.

5.2.2 Preparation of GO and PU Composites

Graphene oxide (GO) from the two types of GnP was prepared by the improved Hummers' method using a mixture of sulphuric acid and phosphoric acid at a volume ratio of 9:1. Synthesized GnP and GO were dried in a vacuum oven at 25 °C for three days to remove moisture. The dried GnP and GO were dispersed in 10 mL of tetrahydrofuran (THF) at 0.013 g and 0.065 g, respectively, using ultra-sonication for 1 hour. 10 g of hardener was added to the THF solution and then the mixture was mixed for 18 minutes using a planetary centrifugal mixer (PCM). After mixing, the mixture was left in a convection oven at 50°C for 2 days, and then was left in a vacuum oven for 1 day at RT to remove THF completely. The mixture removing THF was mixed for 2 minutes with

the resin in the ratio mentioned above using PCM. The final mixture was cast on a clean glass petri dish (diameter: 135 mm) as well as a polished Cu substrate at a thickness of 300 µm. To build a solid surface layer, the cast film was pre-cured at RT for 6 hours and the pre-cured film was fully cured for 24 hours in vacuum oven at 50°C. The final PU nanocomposite after curing was removed from the glass dish for mechanical testing, and the cast film on the Cu substrate was subjected to electrochemical testing. The process of sample preparation is schematically illustrated in Figure 5.1.

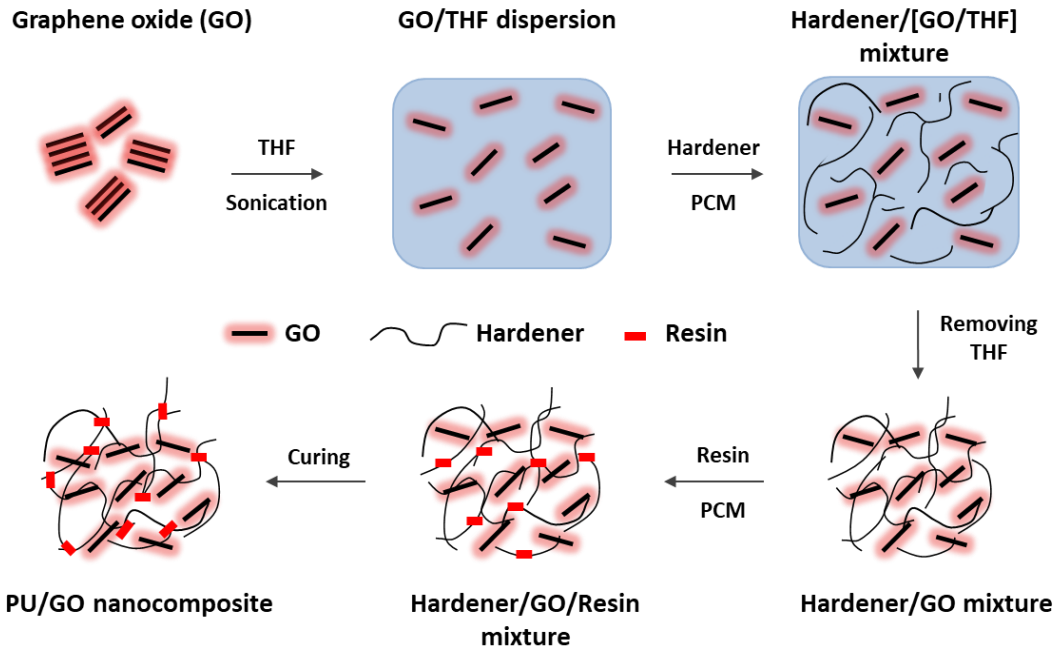

Figure 5.1. Schematic image for the preparation of PU/GO nanocomposites.

5.2.3 Characterization

5.2.3.1 Structure, chemical composition, and morphology characterization

FT-IR (Nicolet 6300, Thermo-Fisher) was used to characterize functional groups on the GO. The samples for FT-IR were prepared by pressing fine potassium bromide (KBr) powders with a small

amount of GnP and GO particles. KBr fine powders were obtained by grinding after drying the powders for2 days at 120°C in a vacuum oven. Each pellet was scanned from 4000 to 400 cm^{-1} under a nitrogen atmosphere. X-ray diffraction (XRD, Rigaku, Miniflex 600) using Cu-Kα radiation (λ = 1.54184 nm) was performed to analyze the structure of the GnP, GO, and nanocomposite samples. The samples were scanned from 2θ = 1 to 80° at Raman spectroscopy (SENTERRA, Bruker) equipped with a microscope was additionally performed to analyze the structural integrity of the GnP and GO using 532 nm of 20 mW He–Ne laser. The morphologies of the GnP, GO, and nanocomposites were observed by scanning electron microscopy (SEM, Zeiss, Leo 1550). Gold sputtering was performed to observe the cross-sectional area of the nanocomposite samples prepared by cryogenic rupture using liquid nitrogen. Transmission electron microscopy (TEM, JEOL 2010F) was used to verify the average diameter of GO.

5.2.3.2 Mechanical properties characterization

The mechanical properties of the PU/GnP nanocomposites were characterized using a universal testing machine (UTM, 4.4 kN load-cell, eXpert 7603, ADMET, USA) as the crosshead rate of 100 mm/min at 25 ℃. Five specimens, fabricated based on ASTM D638, Type V, were measured for each sample. The Type V specimen has an overall length of 63.5 mm, overall width of 9.53 mm, gauge length of 7.62 mm, and a narrow section width of 3.18 mm. Therefore, the tensile modulus was determined by the linear slope of the initial stress-strain curve and the tensile strength corresponded with the maximum strength. In addition, the elongation at break was obtained by the strain at the sample fracture. Hardness was determined using a shore durometer based on the scale D. Five points were measured on the surface of the nanocomposites.

5.2.3.3 Electrochemical properties characterization

The anti-corrosion performance of the nanocomposites was evaluated using the electrochemical corrosion cell for a flat specimen in a double-jacketed glass cell (300 mL). A three-electrode system including the saturated calomel reference electrode was used to measure the corrosion resistance of the nanocomposites. Electrochemical measurements were gathered in a 3.5 wt% NaCl electrolyte solution at RT. The samples were washed by deionized water and dried before mounting to the cell. Cyclic voltammetry (CV) was performed to obtain the corrosion potential and current from the Tafel plot under the conditions of a 20 mV/min scan rate and a potential range of -500 mV-500 mV. Electrochemical impedance measurement (EIS) was performed to obtain the Nyquist plot within a frequency range of100 kHz-200 Hz. From the potentiodynamic measurement, the corrosion rate (R_{corr}) was obtained by the equation 4-2 in the chapter 4 which is based on ASTM standard G102.

5.2.3.4 Thermal properties characterization

Thermogravimetric analysis (TGA, Q500, TA instrument) was used to analyze the thermal stability of the GnP, GO, and the PU nanocomposites. TGA was performed at a rate of 10°C/min up to 800°C under nitrogen with a flow rate of 50 mL/min.

5.3 Results and Discussion

5.3.1 Analysis of GO

Figure 5.2 presents the FT-IR spectra of the two different types of GnP and GO. No functional groups were detected in the GnP samples, while functional groups were identified in the GO samples at 3420 cm^{-1}, 1720 cm^{-1}-1740 cm^{-1}, 1590 cm^{-1}-1620 cm^{-1}, and 1250 cm^{-1} regarding –OH,

C = O, C = C, and C-O stretching vibrations respectively.[150] Therefore, the GO indicated distinct peaks regarding the hydrophilic functionalities on FT-IR spectra in comparison with GnP. In addition, the overall FT-IR spectra of GO-M25 and GO-C750 were similar to each other; however, GO-C750 showed more distinct peaks at 1100 cm^{-1}-1430 cm^{-1} than GO-M25. The peaks are related to C-O stretching vibrations (1220 cm^{-1}) and –OH bending vibrations (1047 cm^{-1}) in the synthesized GO.[71] This is because GO-C750 has a small size, which means higher surface area and more edges than GO-M25 on the GO plane. For this reason, higher oxidized groups were formed on the GO-C750 than the GO-M25 during the oxidization process. In addition, the functionalities of GO led to a uniform dispersion in a hydrophilic solvent such as water or THF. The water dispersion state of the GnP and GO is shown in Figure A.1 in Appendix A.

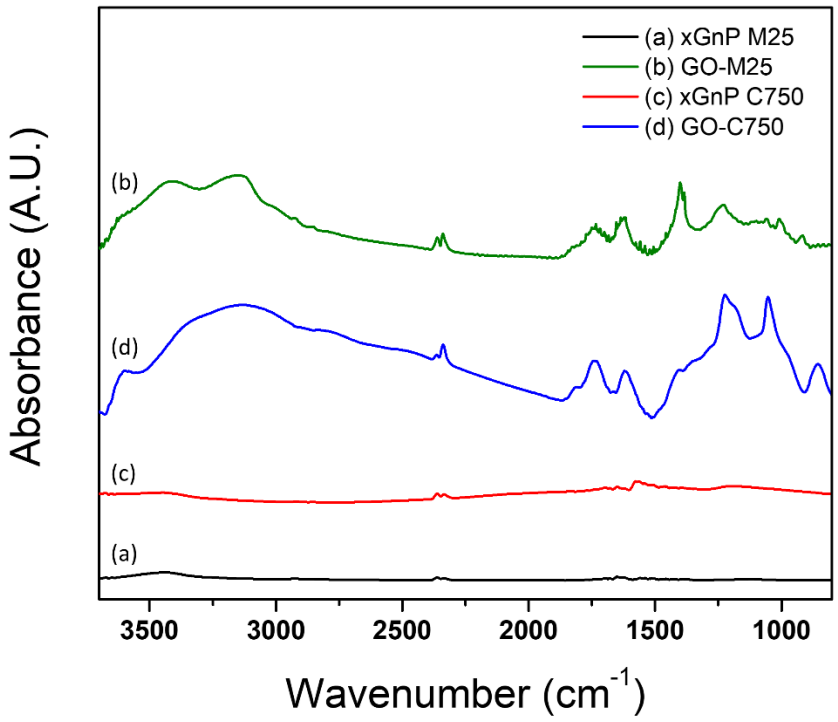

Figure 5.2. FT-IR spectra for two different types of GnP and GO.

The XRD spectra of all of the samples are presented in Figure 5.3a. The spectra of the GO clearly

showed a different pattern from the original GnP. The two types of GnP, M25 and C750, had comparable diffraction peaks at $2\theta = 26.41$ and 26.32°, respectively, while C750 showed a broader peak than M25. In general, the peak broadening effect is related to the lattice distortion in graphene stacking order due to mild oxidation.[71] According to the manufacturer, M25 and C750 were produced by different methods; therefore, the difference in the XRD spectra between the two GnPs can be attributed to the fabrication method. The diffraction peaks from the oxidation of GO-M25 and GO-C750 decreased to $2\theta = 9.24$ and 8.52°, respectively. Furthermore, the interlayer distance (ie, d-spacing) of the graphene layers was obtained by the Bragg's equation, and the crystallite sizes (L_c) of the GnP and GO were obtained based on the Debye-Scherrer equation.[110] Therefore, the number of graphene layers was estimated by the two parameters (eg. number of graphene layers = crystallite sizes (L_c) / interlayer distance (d-spacing)). The interlayer distance of GnP was calculated to be 0.337 nm for M25 and 0.338 nm for C750, while GO-M25 and GO-C750 had values of 0.924 and 0.852 nm, respectively. Consequently, M25 and C750 indicated around 67 and 14 graphene layers, while GO-M25 and GO-C750 indicated around 12 and 8 graphene layers, respectively. The results determined that the oxidation process of GnP resulted in an increase in the interlayer distance of GO and a decrease in the number of GO layers. However, it seems that the oxidation influence of the GO-C750 is not high relative to GO-M25 because C750 already had a lower number of graphene layers than the M25 before the oxidization process. This implies the fabrication process for C750 led to more defects of C750 than M25. Therefore, C750 indicated the low number of graphene layers as well as the small size of graphene.

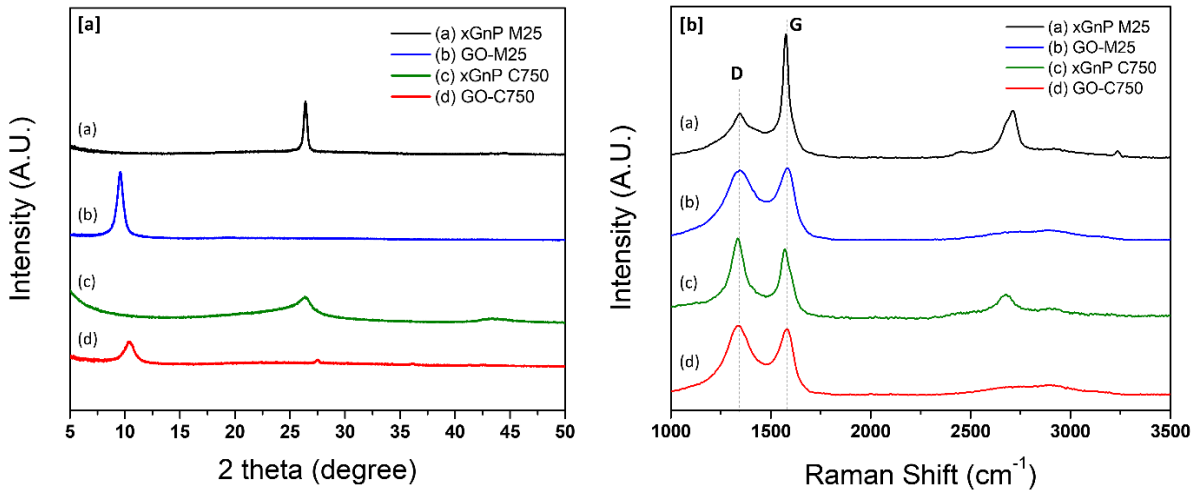

Figure 5.3. XRD [a] and Raman [b] spectra for the two different types of GnP and GO.

Raman spectroscopy was used to analyze the structural integrity of GnP and GO, and Figure 5.3b presents the Raman spectra of all of the samples. In order to compare the integrity of the GnP and GO, two important values were extracted from the Raman spectra; G band (I_G) at 1584 cm^{-1} represents the highly crystalline structure of graphene layers, while D band (I_D) at 1358 cm^{-1} is associated with the existence of defects in the graphene layers, especially for the edge of the graphene sheet. Therefore, the relative intensity ratio of the two bands (I_D/I_G) is widely used to determine the disorder degree of the samples. Furthermore, equation (5-1), Tuinstra and Koenig,[110] was used to estimate the inter-defect distance (L_a). This parameter enables a quantitative comparison of the number of defects in GnP and GO:

$$L_a = (2.4 \times 10^{-10})\lambda^4 \left(\frac{I_D}{I_G}\right)^{-1} \quad (5\text{-}1)$$

where λ is the wavelength of excitation laser (532 nm). The I_D/I_G ratio of M25 was 0.23 and the ratio of C750 was 1.24, while GO-M25 had a ratio of 0.97 and GO-C750 had a ratio of 1.06. These results about the I_D/I_G ratio revealed that the disorder degree of GO was increased by the

functionalities due to the oxidation process. The disorder degree of C750 was higher than M25, as mentioned above, and this result was due to the fabrication method to produce the C750. For this reason, the inter-defect distance of GO-C750 was 18.14 nm and this value was comparable to 15.5 nm of the C750, while the inter-defect distance of GO-M25 was 19.82 nm, and this value was significantly decreased from the 83.59 nm of M25. These findings indicated that the process of GO synthesis resulted in a higher number of defects on the graphene sheets than the original GnP. The defects were attributed to the hydrophilic functionalities on the graphene and they contributed to an increase in the inter-layer distance and decrease in the number of layers of GO. Nevertheless, the oxidization process was more effective on the large size GnP (M25) than the small size GnP (C750). The defects on the C750 are physically formed by the fabrication method, and thus FT-IR indicated no functional groups in the C750. As a result, the pre-formed defects contributed to a reduction in the number of graphene layers; however, this effect was not as significant as it was in the M25. In summary, the M25 lead to higher oxidized graphene structure than the C750 based on the higher structural integrity. Table 5.1 shows the parameters calculated from XRD and Raman spectra.

Table 5.1. Parameters extracted from XRD and Raman spectra

Samples	2θ (°)	d-spacing (Å)	FWHM (rad)	L_c (Å)	Number of graphene layers	I_D/I_G	L_a (nm)
xGnP M25	26.41	3.37	0.006 64	224.13	67	0.23	83.59
GO-M25	9.56	9.24	0.013 69	106.13	12	0.97	19.82
xGnP C750	26.32	3.38	0.031 08	47.84	14	1.24	15.50
GO-C750	10.38	8.52	0.021 53	67.55	8	1.06	18.14

The SEM images of all of the samples are shown in Figure 5.4. Figures 5.4a and 5.4d indicated the size difference between the two types of GnP. M25 indicated a flake-like morphology, while

C750 was a fine powder. Figures 5.4b and 5.4e indicated that the GO-M25 formed individual sheets, but the GO-C750 appeared to be an agglomerated structure. However, Figures 5.4c and 5.4f, in fact, showed that both types of GO are exfoliated sheets. When compared, the larger GO-M25 showed a more exfoliated structure than the GO-C750. This result revealed that the GO synthesis process successfully led to the exfoliation of each GnP; however, the small size of GO was easily agglomerated. Unfortunately, SEM imaging could not be used to estimate the diameter of the GO, and thus TEM was used to observe the diameter of the two GOs. The TEM images showed that the diameter of GO-M25 and GO-C750 were ~20 μm and 1 μm, respectively. The TEM results are described in Figure A.2 of Appendix A. In addition, the hydrophilic functionalities and high disorder degree of GO were associated with the thermal instability of GO.[150] The GnP and GO TGA results are also indicated in Figure A.3 of Appendix A.

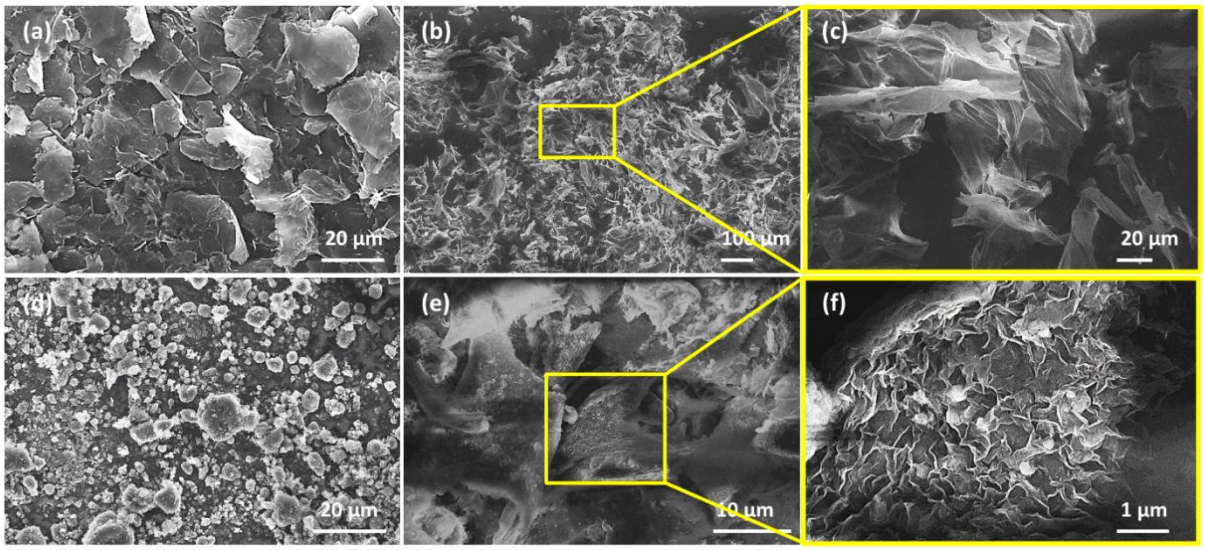

Figure 5.4. SEM images for the two different types of GnP and GO: (a) xGnP M25, (b) to (c) GO- M25, (d) xGnP C750, and (e) to (f) GO-C750.

5.3.2 Morphology of PU/GnP and PU/GO nanocomposites

Figure 5.5 represents the cross-sectional morphologies of the PU/GnP and PU/GO nanocomposites. In this figure, small cracks are shown on the surface of the cross-sectional images for all of the samples due to the electron beam of the SEM. The morphology of PU/M25 nanocomposite at 0.1 wt% was identical of the neat PU, while the PU/M25 nanocomposite at 0.5 wt% showed that M25 had a larger size. Conversely, the PU/GO-M25 nanocomposites indicated a more uniform dispersion of the fillers than the PU/M25 nanocomposites regardless of the content of the fillers. However, the PU/C750 nanocomposites showed a similar morphology to the neat PU at 0.5 wt% because of the small size. Accordingly, the morphologies of the PU/GO-C750 nanocomposites were almost identical to the neat PU. As a result, the GO contributed to the higher uniform dispersion of the fillers than GnP in the PU matrix due to the exfoliated structure and its affinity with the pristine PU.

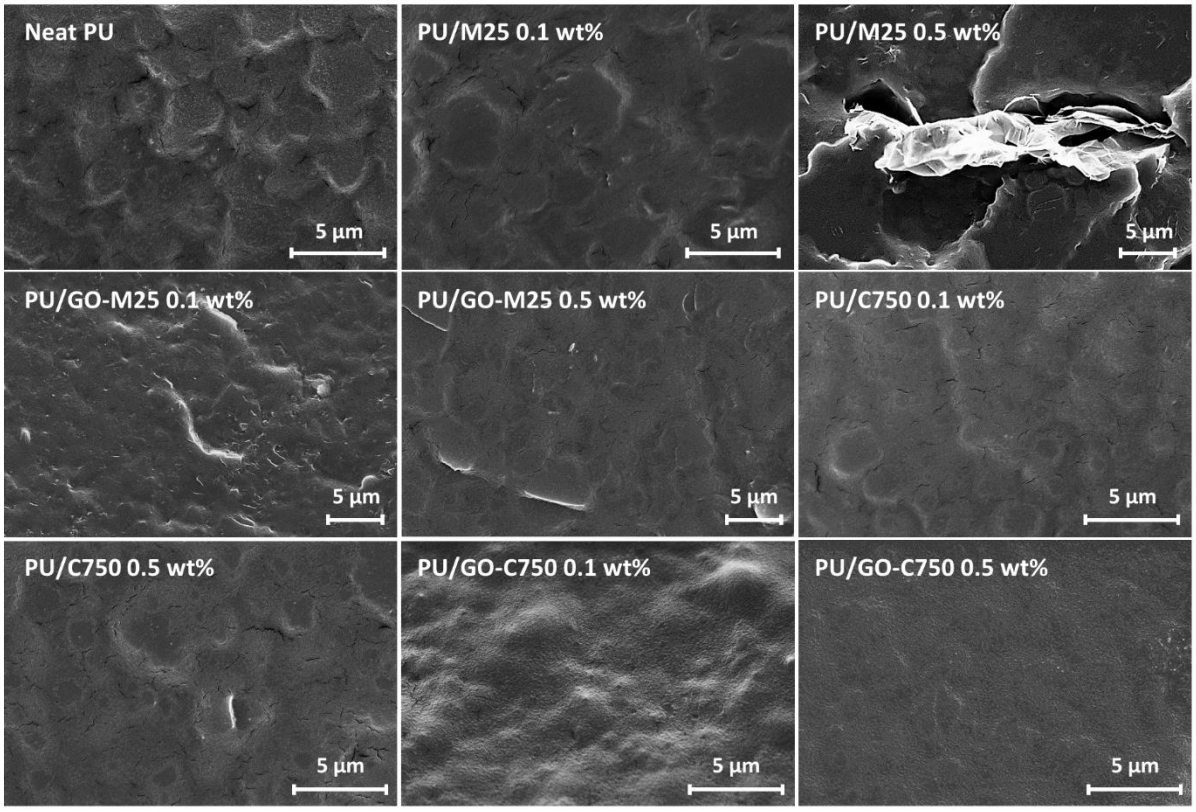

Figure 5.5. Cross-sectional SEM images for PU/GnP and PU/GO nanocomposites.

5.3.3 Mechanical properties of the nanocomposites

The stress-strain curves and the tensile modulus of the pristine PU and the composites are shown in Figure 5.6 a to b. The PU/M25 composites indicated a slightly improved tensile modulus by the increase in the M25 content, while the tensile strength and elongation at break were decreased by the increase in M25. Therefore, the tensile strength was associated with elongation at the break because the stress is proportional to the strain in an elastic material. Conversely, the PU/GO-M25 composites showed significant increases in tensile modulus with the increase in the GO-M25 contents, while the tensile strength and elongation at break showed lower values than the PU/M25 composites. As explained above, the elongation at break of the PU/GO-M25 composites was lower than the PU/M25 composites. The PU/C750 composites resulted in an enhanced tensile modulus

and elongation at break at 0.1 wt%; however, the tensile modulus and tensile strength of the PU/C750 at 0.5 wt% was not enhanced, while the elongation at break increased. Nevertheless, the PU/GO-C750 composites did not show elastic behaviour on the strain-stress curve regardless of the amount of GO-C750. In addition, the hardness of the neat PU and the PU composites indicated a similar tensile modulus as shown in Figure 5.6c. This result can be explained by a model regarding a correlation between hardness and tensile modulus that is suggested by several research groups.[77, 78] The representative correlation determined by the Shore durometer and tensile testing is shown in the equation 3-2 in chapter 3.2. The model indicated that the tensile modulus is associated with the stiffness of a material; therefore, the PU composites that have a high tensile modulus lead to improved hardness.

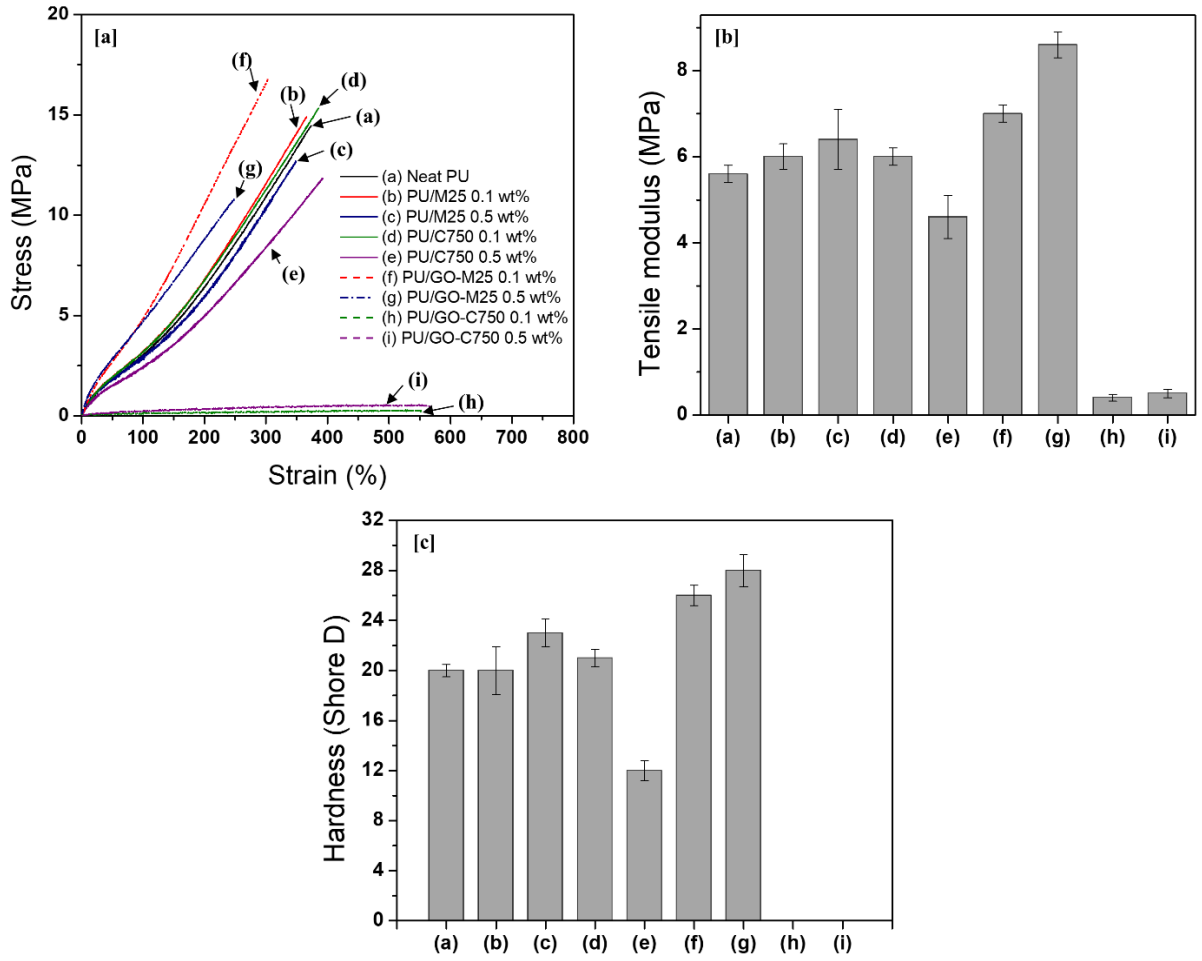

Figure 5.6. Strain-Stress curve [a] of the composites and comparison of tensile modulus [b] and hardness in Shore D [c]. (The error bars in Figure 5.6 (b) and (c) present standard deviations (n=5)).

A recent study was done by M. Razeghi et al.[155] reported that thermoplastic polyurethane (TPU) incorporated with GO, acid treated multi-wall carbon nanotube (MWCNT), and pristine clay showed a decrease in melting temperature (T_m) when compared to pristine TPU and TPU composites incorporated with non-polar nanoparticles such as GnP, non-treated MWCNT, and even reduced GO (RGO). They attributed this phenomenon to the fact that polar nanoparticles readily form smaller hard segments in the TPU matrix due to the increased number of nucleation

sites on their surfaces. For this reason, the small hard segment induced the lower T_m than other composites and pristine TPU. Consequently, the tensile modulus of the TPU composites, including polar nanoparticles, was decreased due to the smaller hard segments. In general, the content of the hard segments in PU considerably influences the tensile modulus of PU. For instance, B. Fernández-d'Arlas et al.[156] described that the elastic modulus of PU based on hexamethylene di-isocyanate (HDI) showed a dramatic increase in proportion to the number of hard segments. Unfortunately, these examples might not fully explain the difference of mechanical propertes between PU/GO-M25 and PU/GO-C750 because they were due to TPU. Nevertheless, these examples would be meaningful to this study because PU in this research also consists of hard and soft-segments the same as TPU.

In this study, PU/GO-M25 nanocomposites had an 53 % enhanced tensile modulus than the neat PU, while PU/GO-C750 nanocomposites did not show elasticity, even though both the GO-M25 and GO-C750 had hydrophilic or polar particles. It seems that the distinct elasticity between the two composites is due to the formation of hard segments in the PU matrix and the interaction between PU and GO The large size of GO-M25 has a lower surface area; therefore, there is a low number of hard segments but the size is large. For this reason, the tensile modulus of the PU/GO-M25 nanocomposites is increased due to the hard segments formed by the strong interaction between GO-M25 and PU. Conversely, the small size of GO-C750 has a high surface area, and therefore there is a high number of hard segments but the size is small. In summary, the higher surface area of GO-C750 can provide numerous sites for nucleation of the hard segment of PU. These many sites lead to smaller hard segments that result in a decrease in the tensile modulus. However, this discussion about GO-C750 is a qualitative explanation based on the previous studies of TPU. Therefore, further research would be required about the hard segment formation of PU on

the hydrophilic functional groups of GO. The mechanical properties of all of the samples are summarized in Table 5.2.

Table 5.2. Mechanical properties of PU/GNP and PU/GO nanocomposites (STD*: Standard deviation for 5 samples)

Samples	Filler contents (wt%)	Tensile modulus (MPa ± STD*)	Tensile strength (MPa ± STD*)	Elongation at break (%)	Hardness (Shore D ± STD*)
Neat PU	-	5.6 ± 0.2	15.0 ± 1.0	399	20 ± 0.5
PU/M25	0.1	6.0 ± 0.3	14.0 ± 2.0	386	20 ± 1.9
	0.5	6.4 ± 0.7	14.0 ± 1.6	349	23 ± 1.1
PU/C750	0.1	6.0 ± 0.2	15.0 ± 0.9	459	21 ± 0.7
	0.5	4.6 ± 0.5	10.0 ± 1.2	437	12 ± 0.8
PU/GO-M25	0.1	7.0 ± 0.2	9.0 ± 2.1	304	26 ± 0.8
	0.5	8.6 ± 0.3	9.0 ± 1.4	249	28 ± 1.3
PU/GO-C750	0.1	0.4 ± 0.1	0.3 ± 0.01	713	N/A
	0.5	0.5 ± 0.1	0.6 ± 0.02	620	N/A

5.3.4 Structure analysis of the PU nanocomposites

The XRD analysis of PU/GnP and PU/GO is shown in Figure 5.7. The XRD pattern of the pristine PU was indicated as a broad peak ($2\theta = 20°$), which corresponds with the amorphous phase, such as the soft segment in PU.[157] In Figure 5.7a, the PU/M25 nanocomposites showed the intrinsic peak of M25 at $2\theta = 26.4°$, and this peak increased with the content of M25. On the other hand, the XRD pattern of the PU/GO-M25 nanocomposites showed an identical pattern to the pristine PU regardless of the content of GO-M25. In Figure 5.7b, the intrinsic peak of C750 was not observed in the spectrum of the PU/C750 nanocomposites. This is because the XRD spectrum of

the C750 had a relatively lower intensity than the XRD pattern of PU at 2θ = 26.3° even in low loading. The PU/GO-C750 nanocomposites showed no significant peak in their XRD pattern, which was the same as the PU/GO-M25. Since both the PU/GO-C750 and PU/GO-M25 nanocomposites showed similar a XRD spectrum with no significant peaks, it is likely that both the GO-C750 and GO-M25 remained exfoliated within the PU matrix.

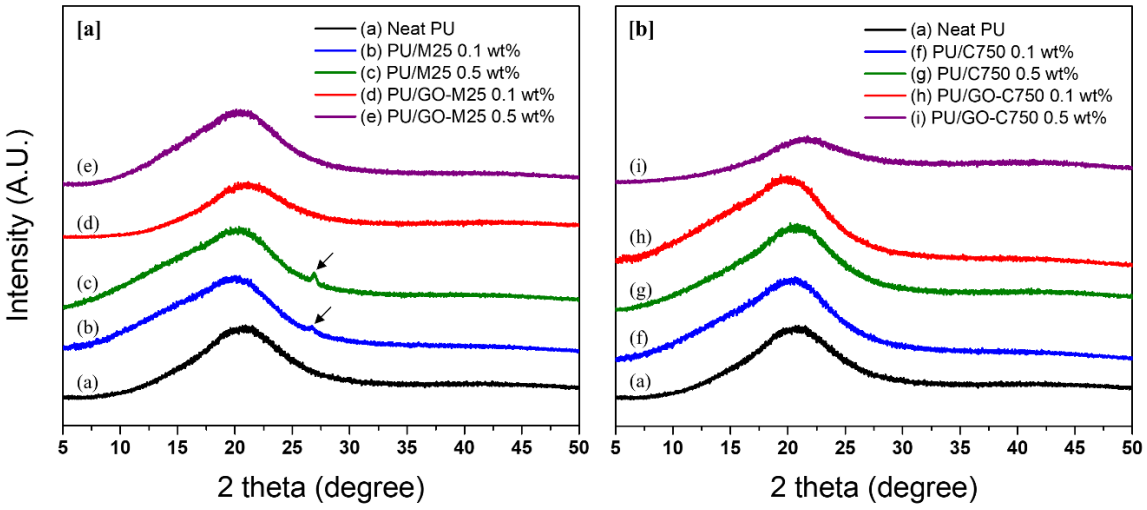

Figure 5.7. XRD spectra of the PU nanocomposites including the large size of GnP and GO [a] and the small size of GnP and GO [b].

5.3.5 Electrochemical properties of PU/GnP and PU/GO nanocomposites

Cyclic voltammetry (CV) is used to obtain the Tafel polarization curve, which quantifies the anti-corrosion performance of the PU/GnP and PU/GO composites. The Tafel plot provides the corrosion potential (E_{corr}) and corrosion current (I_{corr}), and these parameters enable a quantitative comparison between the anti-corrosion performance of a material. For instance, the enhancement of the anti-corrosion performance is associated with the tendency for an increase in the E_{corr} and a decrease in the I_{corr}.[158] The two parameters, E_{corr} and I_{corr}, are determined by the intersection point extrapolated cathodic and anodic curves in the Tafel slopes. The Tafel plots for PU/GnP and

PU/GO-M25 are shown in Figure 5.8 and the parameters extracted from the plots are summarized in Table 5.3. However, the Tafel plots of the PU/GO-C750 composites were not produced because they did not meet the mechanical property requirements due to the absence of elasticity.

The PU/M25 composites in Figure 5.8 indicate a slightly increased E_{corr} of -275.5 mV and decreased I_{corr} of 0.018 μA/cm^2 relative to the amount of M25 rather than the pristine PU (E_{corr}: -297.8 mV, I_{corr}: 0.127 μA/cm^2). On the other hand, PU/C750 composites showed better anti-corrosion performance (E_{corr}: -97.1 mV, I_{corr}: 0.002 μA/cm^2) than the PU/M25 composites. This is attributed to the fact that the smaller size of C750 is not only uniformly dispersed within the PU but also offers a high surface area. This effect considerably contributes to the construction of an efficient filler arrangement that suppresses the diffusion of a corrosive agent onto the Cu substrate.[158] For this reason, PU/GO-M25 composites show a higher E_{corr} of -63.7 mV and lower I_{corr} of 0.001 μA/cm^2 than the PU/C750 composites at the same fillers content. These results meant that the GO-M25 was more uniformly dispersed and exfoliated than the C750 in the PU matrix.

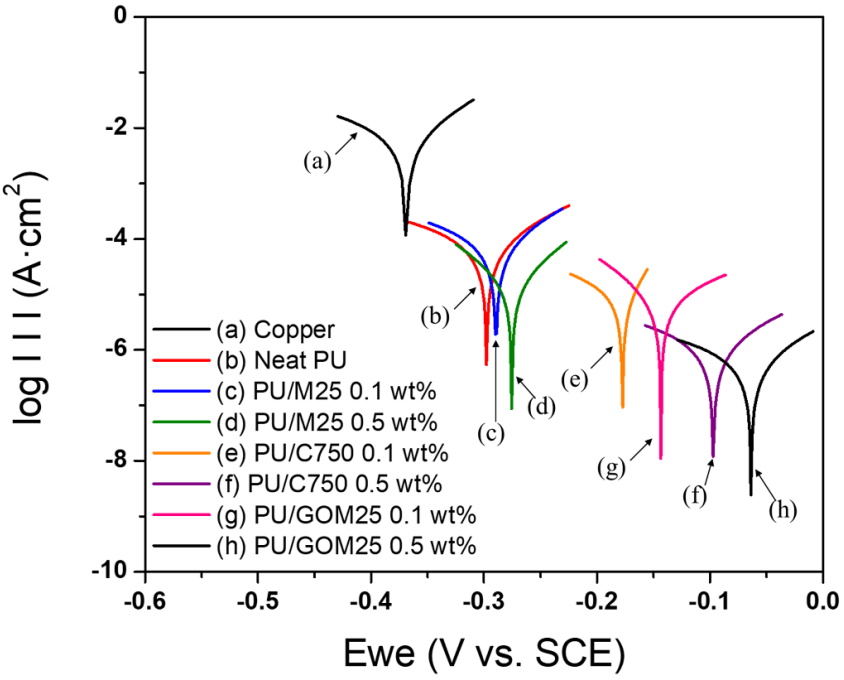

Figure 5.8. Tafel plots for the neat Cu substrate and the pristine PU, the PU/GnP composites, and the PU/GO composites.

Polarization resistance ($R_{p,Tafel}$) was another parameter used to compare anti-corrosion performance. $R_{p,\ Tafel}$ was calculated by using the Stern-Geary equation 5-2 same as equation 3-3 in the chapter 3.[159]

$$R_{p,Tafel} = \frac{b_a \times b_c}{2.303 \times (b_a + b_c) \times I_{corr}} \tag{5-2}$$

where b_a and b_c are constants representing the slopes of the anodic and cathodic curves in the Tafel plot. In addition, protection efficiency (P_{EF}) was also used to evaluate the anti-corrosion performance of a coated metal substrate, given by 5-3.[159]

$$P_{EF}\ [\%] = \left(1 - \frac{I_{corr}}{I^{\circ}_{corr}}\right) \times 100 \tag{5-3}$$

In Table 5.3, $R_{p,\ Tafel}$ of the PU/C750 composites was dramatically increased from 293.2 Ω·cm^2 to 21178.3 Ω·cm^2 in comparison to the pristine PU. On the other hand, the PU/GO-M25 composites had a greater $R_{p,\ Tafel}$ than PU/C750, up to 40 861.9 Ω·cm^2. Furthermore, the PU/GO-M25 composite showed a P_{EF} value that is close to 100%. Therefore, the important point in this study is that GO enables the greater uniform dispersion in the polymer matrix and contributes to enhancing the anti-corrosion performance as well as the mechanical properties. These results were supported by the cross-sectional morphologies of SEM.

Table 5.3. The parameters extracted from Tafel plots

Samples	Filler contents (wt%)	E_{corr} (mV vs. SCE)	I_{corr} (μA/cm^2)	b_a (mV/dec)	b_c (mV/dec)	$R_{p,Tafel}$ (Ω·cm^2)	R_{corr} (MPY)	P_{EF} (%)
Cu	-	-367.0	9.024	98.4	195.1	3.2	5.266	-
Neat PU	-	-297.8	0.127	130.1	251.8	293.3	0.074	98.99
PU/M25	0.1	-289.4	0.119	108.8	210.0	261.5	0.069	99.05
	0.5	-275.5	0.018	67.3	73.5	847.5	0.011	99.86
PU/C750	0.1	-177.5	0.011	42.3	128.7	1256.7	0.006	99.91
	0.5	-97.1	0.002	147.8	286.9	21,178.3	0.001	99.98
PU/GO-M25	0.1	-143.5	0.011	158.6	83.8	2164.4	0.006	99.91
	0.5	-63.7	0.001	136.6	302.5	40,861.9	0.001	99.99

To supplement the results from the Tafel plot, electrochemical impedance spectroscopy (EIS) was used to characterize the anti-corrosive performance. For the EIS measurement, an appropriate equivalent circuit model was required to match an acquired impedance data. Suggested equivalent circuit models for Cu and Cu substrate incorporated with a protective layer are shown in Figure 5.9.[126]

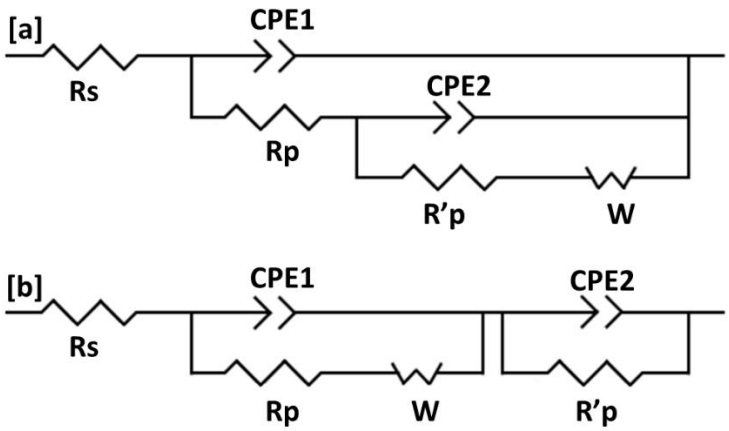

Figure 5.9. Equivalent circuit model: [a] neat Cu and [b] film coated Cu substrate.

In Figure 9, R_s presents the solution resistance, R_p presents the polarization resistance of the protective layer, CPE1 and CPE2 represent the constant phase elements, R'_p represents another polarization resistance, which relates to charge-transfer resistance, and W is the Warburg impedance. Figure 5.10 illustrates the Nyquist plots for the bare Cu substrate and the PU composites on Cu.

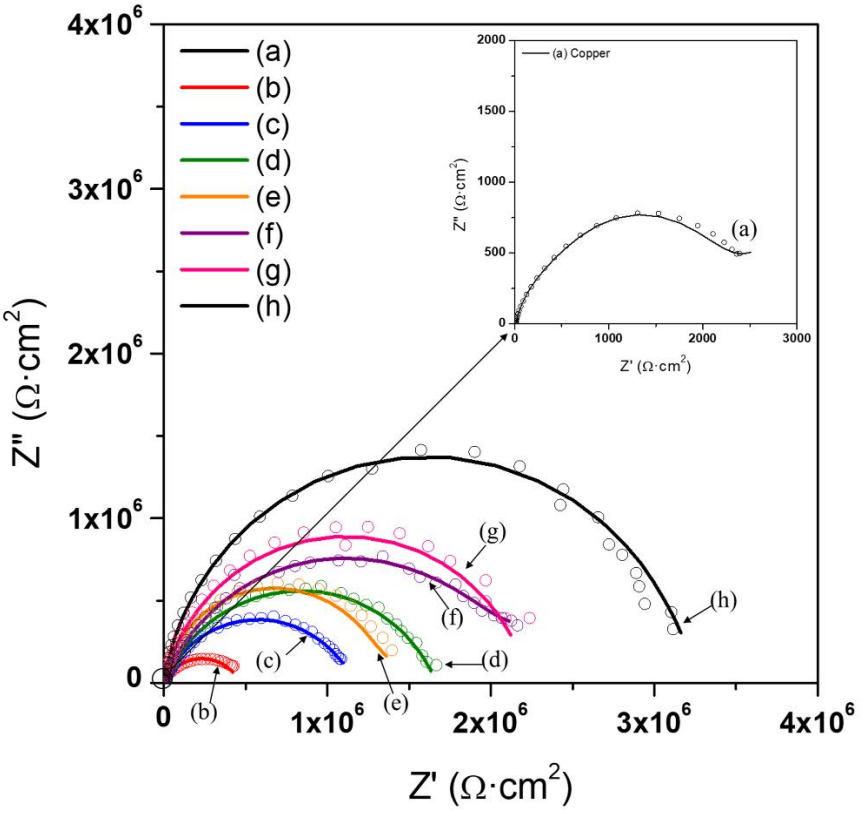

Figure 5.10. Nyquist plots (solid lines; fitting curve with the equivalent circuit, dotted lines: acquired data); (a) neat Cu, (b) pristine PU, (c) PU/M25 (0.1 wt%), (d) PU/ M25 (0.5 wt%), (e) PU/C750 (0.1 wt%), (f) PU/C750 (0.5 wt%), (g) PU/GO-M25 (0.1 wt%), and (h) PU/GO-M25 (0.5 wt%).

To analyze the anti-corrosion performance using the Nyquist plot, the diameter of the semicircle in the plot is considered to compare the performance. The diameter is associated with the R'_p in the equivalent circuit of Figure 5.9, and thus a higher resistance corresponds to a larger semicircle diameter. Therefore, polarization resistance is converted to anti-corrosion performance. In Figure 5.10, the Cu substrate represented the typical curve in the Nyquist plots and the semicircle diameter showed 1,336 $k\Omega \cdot cm^2$.[126] On the other hand, the pristine PU on Cu had R'_p of 465,924 $k\Omega \cdot cm^2$, which means that the PU has a greater anti-corrosion performance than Cu substrate In the case of

PU/M25 composites, the results indicated higher R'_p than PU at a value of 1,044,000 $k\Omega \cdot cm^2$ at 0.1 wt%; however, the R'_p raised to 2,019,000 $k\Omega \cdot cm^2$ at 0.5 wt%. Furthermore, PU/C750 composites showed a higher R'_p than PU/M25 at a value of 1,252,000 $k\Omega \cdot cm^2$ at 0.1 wt% and 3,209,000 $k\Omega \cdot cm^2$ at 0.5 wt%. The PU/GO-M25 composites indicated a greater R'_p than PU/C750 in the same content of fillers. Each R'_p of the composites increased to 2,230,000 $k\Omega \cdot cm^2$ at 0.1 wt% and 9,628,000 $k\Omega \cdot cm^2$ at 0.5 wt%. As a result, the results of the Nyquist plot were in accordance with the results of the Tefal plot. As explained above, the anti-corrosion performance of the composites strongly depends on the dispersion uniformity of a filler. For this reason, GO is favourable for uniform dispersion in the PU matrix and the obtained dispersion is capable of preventing the diffusion of the corrosive agent efficiently. The small sized GnP was also efficient for protection; however, the exfoliated form of GO contributed to achieving a much higher anti-corrosion performance. The parameters regarding the equivalent circuit extracted from the Nyquist plot are summarized in Table 5.4.

Table 5.4. Equivalent circuit parameters fitting with the acquired data from Nyquist plots

Samples	Filler contents (wt%)	Rs ($\Omega \cdot cm^2$)	Rp ($\Omega \cdot cm^2$)	CPE1 ($\Omega^{-1} \cdot S^{n1} \cdot cm^{-2}$)	n1	R'p ($\Omega \cdot cm^2$)	CPE2 ($\Omega^{-1} \cdot S^{n2} \cdot cm^2$)	n2	W ($\Omega^{-1} \cdot S^{n1} \cdot cm^{-2}$)
Cu	-	12.38	9.47E+02	2.33E-05	0.82	1.37E+03	6.14E-05	0.77	2.7E+02
Neat PU	-	11.92	1.28E+03	1.28E-09	0.86	4.66E+05	2.04E-07	0.72	1.6E+03
PU/M25	0.1	12.17	4.31E+04	9.08E-07	0.53	1.04E+06	2.18E-08	0.76	5.9E+03
	0.5	12.03	2.93E+04	9.16E-09	0.44	2.02E+06	9.64E-09	0.78	1.7E+04
PU/C750	0.1	12.08	1.02E+05	1.44E-06	0.14	1.25E+06	2.85E-10	0.91	7.4E+04
	0.5	11.96	1.54E+05	7.77E-07	0.80	3.21E+06	6.23E-10	0.90	3.4E+04
PU/GO-M25	0.1	12.23	3.09E+05	1.29E-09	0.61	2.23E+06	4.31E-10	0.86	6.6E+03
	0.5	12.14	5.55E+05	7.49E-10	0.88	9.63E+06	2.05E-09	0.84	7.7E+04

5.4 Conclusion

In this study, two different GO (GO-M25 and GO-C750) were successfully synthesized from two different sizes of commercial GnP (M25 (Avg. diameter: 25 μm), C750(Avg. diameter: under 2 μm)). The GO-M25 indicated higher oxidation efficiency than the small sized GO-C750. This is because the original GnP, M25 and C750, had different graphene structure due to a different production method. PU nanocomposites were fabricated using THF to disperse the GO solution in the polymer matrix. PU/GO-M25 nanocomposites showed 34 % improvement on the tensile modulus in comparison to the PU/M25 nanocomposites. Conversely, the PU/GO-C750 nanocomposites showed non-elastic behavior in comparison to the PU/C750 nanocomposites. The improvement of the PU/GO-M25 was attributed to the uniform dispersion of the fillers confirmed by SEM and the strong interaction between PU and GO-M25, such as hydrogen bonding. Whereas, PU/GO-C750 did not indicate the tensile modulus in mechanical properties. This result can be explained by that the size of the hard segment in PU/GO-C750 was insufficient to showing elastic behavior of the nanocomposite. This is because many hydrophilic functional groups on GO-C750 could provide numerous nucleation sites for forming the hard segments of PU. This fact could be confirmed by previous studies regarding the TPU nanocomposite containing acid treated MWCNT. Nevertheless, this effect requires further research to confirming the correlation between the functional groups of GO and the hard segment in PU. In the anti-corrosion performance, the PU/GO-M25 nanocomposite showed a higher performance than PU/M25 nanocomposites. This improvement in PU/GO-M25 can be attributed to the uniform dispersion of the fillers and the interaction between the PU and fillers. The XRD results showed the uniform dispersion of GO in the PU matrix. Besides, the morphologies of the PU/GO composites supported the XRD results. However, the low thermal stability of GO needs to be improved to apply the PU/GO

nanocomposites to pipeliners in oil sands transportation because of the hot oil sands slurry (~80 °C). In chapter 6, a chemical functionalization of GO will be investigated to improve the thermal stability with maintaining high interfacial interaction between GO and the PU matrix.

6. Development of π- π Interaction-Induced Functionalized Graphene Oxide on Mechanical and Anticorrosive Properties of Reinforced Polyurethane Nanocomposites

This chapter is reprinted form from the article below. Permission will be obtained from ACS.

Jun Geun Um, Saeed Habibpour, Yun-Seok Jun, Ali Elkamel, and Aiping Yu. "Development of π- π Interaction-induced Functionalized Graphene Oxide on Mechanical and Anticorrosive Properties of Reinforced Polyurethane Nanocomposites", *ACS Industrial & Engineering Chemistry Research,* In press (DOI: 10.1021/acs.iecr.9b06755), 2020.

In chapter 5, the PU nanocomposites containing two different sizes of GO were fabricated. GO had various hydrophilic functional groups and they led to reducing the number of graphene layers. The PU/GO nanocomposites showed a better dispersion in the PU matrix than GnP due to the functional groups. In particular, large size GO resulted in both improvements of mechanical and anti-corrosive properties of the PU nanocomposites. These improvements are associated with the dispersion of fillers and interfacial interaction between the PU matrix and GO, such as hydrogen bonding. However, the small size of GO was not effective to reinforce the physical properties of the nanocomposites. It seems that the small size GO reduced the size of the hard segments in the PU nanocomposites and then this effect resulted in a decrease of mechanical properties of the nanocomposites. Nevertheless, this discussion requires further research to confirm this effect. Although GO contributed to improving both mechanical and anti-corrosion properties of PU/GO the hydrophilic functional groups of GO were vulnerable to decompose at high temperatures. This drawback of GO can cause a failure of the PU/GO nanocomposites under harsh conditions. For example, PU pipeliners for oil sands transportation are generally operated at high temperatures

(~80 °C) because of the hot oil sands slurry.[52, 63, 64] At this point, the PU/GO nanocomposites are not sufficient as applying to pipeliners due to the low thermal stability of GO. Therefore, chemical modification of GO can be considered as a breakthrough for improving the thermal stability of GO by maintaining the interfacial interaction between GO and the PU matrix. In this chapter, amine functionalized GO (f-GO) has been studied to improve the challenge of GO. 3 different types of amine groups have been investigated for the objectives of this study. Amine groups are highly reactive with carboxylic acid groups of GO and amide groups can be formed by the chemical reaction between the amine and carboxylic acid groups. 2 aliphatic (Dodecyl ($C_{12}H_{27}N$) and *tert*-butyl ($C_4H_{11}N$) amine groups) and one aromatic (2-naphthyl ($C_{10}H_9N$)) amine groups are used for f-GO. The dodecyl amine group is designed to forming a chain entanglement between the dodecyl groups and the polyol of PU due to a long hydrocarbon chain of the dodecyl group. *tert*-Butyl amine group is also expected to form the chain entanglement with the polyol of PU due to its short but branched structure. Whereas, the 2-naphthyl group is designed to forming an interaction among aromatic parts in the isocyanate of PU and the 2-naphthyl group. Therefore, the synthesized f-GO would be compared with GO in terms of overall properties as well as thermal stability. In addition, mechanical and anti-corrosion properties of the PU/f-GO nanocomposites would be thoroughly investigated in this chapter.

6.1 Introduction

For many years, graphene has been widely used as a new functional material for polymer composites based on its surprising intrinsic properties such as mechanical strength and thermal conductivity.[37, 132, 133, 160] To maximize the performance of the polymer-graphene composites, a single layer graphene dispersion within the polymer matrix has been ideal but it has been a challenge in terms of fabricating the composites. This challenge is due to the reason that

one atomic layer graphene would be thermodynamically unstable. Thus graphene cannot exist in the single planar layer within the polymer matrix.[134, 135] Furthermore, the hydrophobic surface of the graphene layers leads to weak interfacial interactions with the polymer matrix, especially for hydrophilic polymers.[153, 161] This inherent nature of graphene limits improving the performance of the composites. The multiple-layer graphene structure which is referred to as graphene nanoplatelets (GnP) has been studied for several years as a candidate to optimize the properties of the composites.[118, 128, 138] GnP has the potential to be cost-effective and high-performance polymer composites based on easier processing than single-layer graphene.[145, 147, 162] However, the interfacial incompatibility and a large number of graphene layers have remained as a problem of polymer composites with GnP. For this reason, a different approach to achieve satisfying polymer-graphene composites has spurred intensive interest to researchers.[163]

Graphene oxide (GO) has opened new pathways to form exfoliated graphene structure and allows building uniform dispersion of graphene in the polymer matrix.[71, 151, 164] This is because oxygen-containing groups such as hydroxyl (-OH), epoxy (C-O-C), and carboxyl groups (-COOH) are covalently attached to the surface of GO.[165] These functionalities are widely scattered on the graphene, however, –COOH groups are mostly positioned to the edges of the graphene planes, while the hydroxyl and epoxy groups are bond to the surface of the basal planes.[150, 166] Not only do these hydrophilic groups ensure the uniform dispersion of GO in water or hydrophilic organic solvents,[152] but also give rise to significant improvements in the polymer composites especially for elastic modulus and thermal stability. For instance, poly (vinyl alcohol) (PVA)/GO composite indicated 76% higher tensile strength and 62% higher elastic modulus than neat PVA at 0.7 wt% GO loading.[144] This improvement of the composite was attributed to uniform filler dispersion and interfacial hydrogen bonding between polymer and fillers. However, to fully utilize

the performance of GO, hydrophilic polymers should be used as the matrix. Therefore, an additional technique to control the surface of GO is required for applying GO to various polymeric materials.[130]

GO can be chemically modified with specific functional groups, including isocyanate and amine and the modified surface of GO can provide higher compatibility between the fillers and the polymer matrix.[3, 31, 136] For instance, Kim et al,[38] designed functionalized GO with isocyanate groups in which functionalization resulted in 80 to 90% improvement in tensile modulus of in-situ polymerized polyurethane composites. Furthermore, GO can form a grafted structure with polymer chains and the polymer-modified GO can lead to solubility enhancement of GO in organic solvents. For instance, polystyrene(PS)-grafted GO showed a higher solubility in PS/toluene solution. Thus, PS nanocomposites including 0.9 wt.% of PS-grafted GO improved 57% and 70% of modulus and strength of the composite, respectively. This is because the modified surface of GO dramatically reduces the total free energy of the composite system. Consequently, this thermodynamic change contributes to the interfacial property of the composites between the modified GO and the polymer matrix.[146]

Chemically functionalized GO has been studied theoretically and experimentally by several research groups. Particularly, solution processable graphene composites including the functionalized GO have been attractive to researchers because of its vast range of applications from photonics, optoelectronic devices to polymer composites.[49, 167] Along this line, the current interest of our research is designing and synthesizing polyurethane composites with the functionalized GO based on solution processing through the organic solvent such as tetrahydrofuran (THF). In particular, we designed three different types of amine functionalized GO via chlorinated graphene oxide by using two aliphatic (linear and branched) and aromatic amine

structures. Besides, the effects of the functional groups on mechanical properties and corrosion resistance of the polyurethane composites have been thoroughly investigated. The aromatic amine functionalized GO has significantly improved the anti-corrosion and mechanical properties of PU. Thus, it has been proved to be an excellent candidate for reinforcing PU used in pipelines for oil sand transportation and other areas.

6.2 Experimental

6.2.1 Materials

GnP was purchased from XG science (US) as the grade of xGnP M25 (M25) to synthesize the functionalized graphene oxide. According to the technical report provided by XG science, the M25 has 25 μm of the average diameter with 7 % of standard deviation, approximately 120 m^2/g of the surface area with a density of 2.2 g/cm^3. Commercially available polyurethane (Rencast 6401) was purchased from Huntsman (US) and Rencast 6401 consists of resin and hardener; the resin comprises oxyalkylene polymer (i.e. polyol) and the hardener comprises 4,4'-Methylene diphenyl diisocyanate (MDI). The resin and hardener could be mixed by 100:25 of mass ratio following the technical data from the manufacturer. Three types of amine groups, dodecyl amine (DA), *tert*-butyl amine (tBA), and 2-naphthyl amine (2NA), were purchased from Sigma-Aldrich to functionalize the surface of GO. The physical properties of the 3 types of the amine groups are summarized in Table 6.1. Anhydrous grade of thionyl chloride ($SOCl_2$), THF, and dimethylformamide (DMF) were purchased from Sigma-Aldrich for the functionalization and dispersion of GO.

Table 6.1. Physical propertes of the 3 different type of the amine functional groups.

Amine groups	Molecular weight (g/mol)	Density (g/cm^3)	Melting point (°C)	Boiling point (°C)
Dodecyl amine (DA)	185.35	0.806	29.0	249.0
tert-butyl amine (tBA)	73.14	0.696	-67.5	45.0
2-naphthyl amine (2NA)	143.19	1.061	112.0	306.0

6.2.2 Preparation of functionalized GO

A modified Hummer's method was used to synthesize GO, which is described elsewhere.[151] The prepared GO was dried for 5 days in a freeze dryer before chlorination. After freeze-drying, 50 mg of GO was refluxed in 20 mL of $SOCl_2$ with 1 mL of DMF for 24 hours at 70 °C under N_2 atmosphere in order to transform the carboxylic acid groups of GO to acyl chlorides (Cl-GO). The remaining solid after centrifugation of Cl-GO was washed with anhydrous THF and then they dried under vacuum at room temperature for 24 hours. The obtained Cl-GO and 1 g of the three types of amine-reagents were dispersed in 20 mL of DMF and the mixture was stirred vigorously for 65 h at 50 °C under N_2. The f-GO was separated by 0.5 μm PTFE membrane via reduced pressure and then washed with anhydrous THF. The f-GO series was described as DA-GO (dodecyl amine), tBA-GO (*tert*-butyl amine), and 2NA-GO (2-naphthyl amine) by the amine group. In order to qualitatively confirm the functionalization process, synthesized f-GO series were dispersed in water and hexane as a polar and non-polar solvent, respectively. The f-GO showed better dispersion in hexane with respect to M25 and GO, while GO was dispersed better than f-GO in water. Therefore, it seemed that the f-GO series were successfully synthesized by the dispersion appearance of the solutions. The appearance of f-GO dispersion in the two solvent is shown in

Figure A.4 of Appendix A.

6.2.3 Preparation of PU nanocomposites

The three types of f-GO were immediately dispersed in 20 mL of THF using ultra-sonication for 0.5 hours after the washing process. 8 g of resin was mixed with the f-GO/THF solution and stirred vigorously for 24 hours at room temperature. The mixture was dried under vacuum for 2 days at room temperature to remove THF. 2g of the hardener was added to the f-GO/resin mixture and then the total composite was mixed using a planetary centrifugal mixer (PCM) for 2 minutes. The final mixture was cast using the adjustable film applicator (GARDCO, US, width: 76 mm) as 100 μm of the film thickness. The cast film was procured at room temperature for 2 hours and then fully cured for 24 hours at 50 °C under vacuum. Electrochemical testing of the PU composites was performed with Cu plate; however, mechanical properties of the composites were tested after peeling off the film from Cu plate. The schematic of f-GO synthesis, sample preparation of the composites, and a photo of real free film samples of the composites are shown in Figure 6.1.

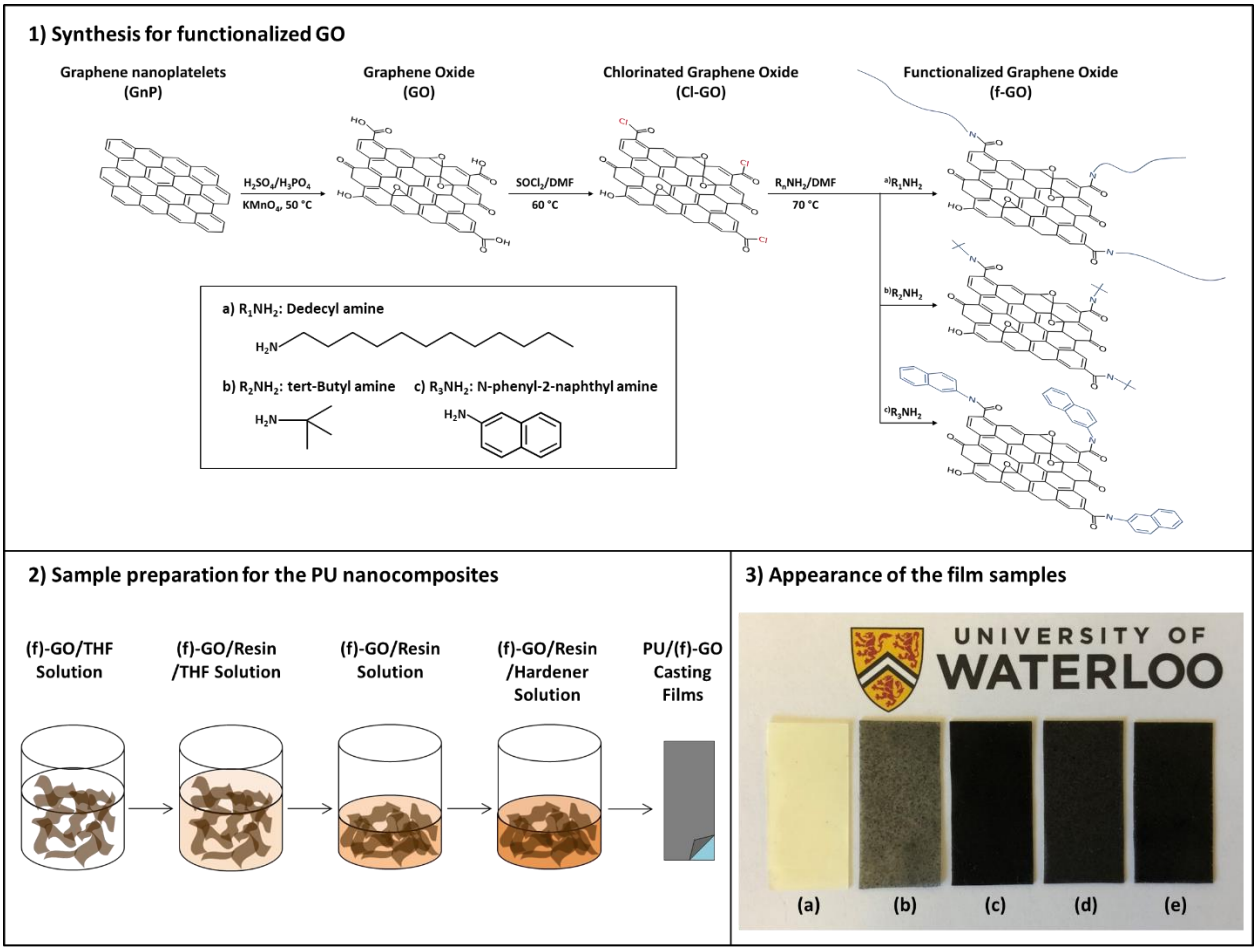

Figure 6.1. Schematic image; (1) the synthesis procedure of the functionalized GO preparation of PU/GO composites, (2) Film sample preparation for PU composites, (3) Appearance image for the film samples: (a) Neat PU, (b) PU/M25, (c) PU/DA-GO, (d) PU/tBA-GO, (e) PU/2NA-GO.

6.2.4 Characterizations

6.2.4.1 Morphology, functionalization, and structure analysis

The morphological properties of f-GO and the composites were analyzed by scanning electron microscopy (SEM, Leo 1550, Zeiss). The cryogenic rupture method with liquid nitrogen was used for cross-sectional SEM specimens. Additionally, gold sputtering was performed on the cross-

sectional specimens of f-GO and the composites samples. FT-IR (Nicolet 6300, Thermo-Fisher) was used to analyze functional groups of f-GO. Potassium bromide (KBr) fine powder was used to prepare KBr pellet with a small amount of f-GO, and the analysis done from wavenumber of 4000 to 400 cm^{-1} under nitrogen atmosphere. The structural integrity of f-GO series was analyzed by Raman spectroscopy (SENTERRA, Bruker) equipped with a microscope using 532 nm of 20 mW He–Ne laser. The structure of f-GO and the composite samples were characterized by X-ray diffraction (XRD, Rigaku, Miniflex 600) using Cu-Kα radiation (λ = 1.54184 nm). XRD was performed by the scan rate of 1 °/min from 2θ = 1° to 80°.

6.2.4.2 Thermal properties characterization

Thermal properties of f-GO and the composites were analyzed by thermogravimetric analysis (TGA, Q500, TA instrument). The samples were scanned from 30 °C to 800 °C at the rate of 10 °C/min under nitrogen and air.

6.2.4.3 Mechanical properties of the composites

Universal testing machine (UTM, ADMET, eXpert 7603, USA) was used to characterize the mechanical properties of the neat PU and the PU composites. UTM was performed as the crosshead rate of 100 mm/min at room temperature with 50 % humidity and five specimens were prepared for each sample. The specimens were prepared by ASTM D638 and Type V specimen size was selected for testing. The strain-stress curve was obtained by UTM testing and tensile modulus, tensile strength, and elongation at break were extracted from the strain-stress curve. Hardness property of the composites was characterized by Durometer following the scale of Shore D and five points per each sample were measured on the surface of the composites.

6.2.4.4 Electrochemical properties of the composites

Electrochemical properties such as corrosion resistance were measured by corrosion cell testing including a double-jacketed glass cell (300 mL) with a flat specimen. The corrosion resistance of the composites was evaluated by a three-electrode system with the saturated calomel reference electrode in 3.5wt% NaCl electrolyte solution at room temperature. Deionized water was used to wash the samples before mounting to the cell. Tafel plot was obtained by cyclic voltammetry (CV) using the cell under the conditions of 20 mV/min scan rate and -500 mV to 500 mV of potential range. The corrosion potential (E_{corr}) and corrosion current (I_{corr}) were extracted from Tafel plot to evaluate the corrosion resistance of the composites. I_{corr} was used to decide the corrosion rate (R_{corr}, MPY (mils per year)) based on the equation 4-2 in the chapter 4 following ASTM standard G102. Additionally, Nyquist plot was obtained by electrochemical impedance measurement (EIS) under the frequency range from 100 kHz to 200 Hz at room temperature.

6.3 Results and Discussion

6.3.1 Analysis of f-GO

Figure 6.2 shows SEM images of GnP, GO, and f-GO series. Flake like morphology of xGnP M25 is observed while M25-GO indicated a scattered paper-like morphology. That means the oxidation process of M25 led to the exfoliation of GnP due to the gallery space (i.e. interlayer distance among graphene layers) expansion induced by oxygen-containing functional groups. Conversely, f-GO series such as DA-GO, tBA-GO, and 2NA-GO show a partially exfoliated structure (Figure 6.2 (c) to (e)). It seems that the amine groups can mainly exist at the edge of GO layers due to a chemical reaction between acyl chloride and the amine groups. According to the Lerf-Klinowski model of GO,[43] most carboxylic acid is placed at the edge of GO. Thus, the acyl chloride, the product of

chlorination, can be also placed at the same position and then chemical reaction with the amine groups can also occur at the same edge. In this process, the amine groups can deform the layer structure of f-GO, consequently, the f-GO series can have a partially exfoliated layer structure. Moreover, tBA-GO shows a higher exfoliated structure than DA-GO and 2NA-GO. This was attributed to the lower molecular weight of tBA (73.14 g/mol) which allows the amine group to easily penetrate the GO layers. Furthermore, the relatively short structure of the hydrocarbon (*tert*-butyl) may contribute to the penetration. Thus, tBA-GO maintains the exfoliated GO structure due to the molecular weight and chain length of the hydrocarbon structure. For this reason, 2NA-GO shows a similar number of graphene layers to DA-GO in the SEM images. 2-naphthyl amine (2NA) and dodecyl amine (DA) have a molecular weight of 143.19 and 185.35 g/mol, respectively. Consequently, the factors, molecular weight and chain length of the amine group can play a key role in the structure of the functionalized graphene.

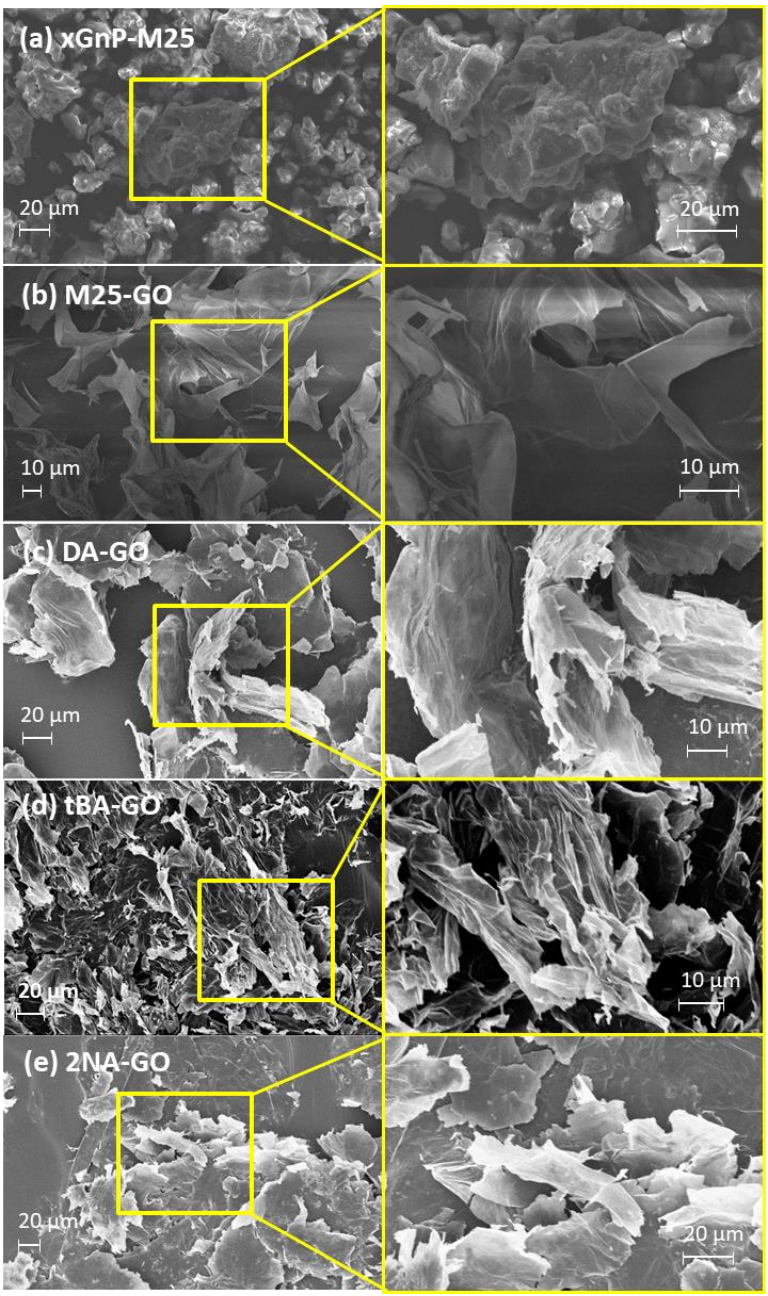

Figure 6.2. SEM images for the (a) xGnP M25, (b) M25-GO, and the three different types of functionalized GO such as (c) DA-GO, (d) tBA-GO, and (e) 2NA-GO. (The yellow boxes indicate magnified images for a specific area)

Figure 6.3 presents the XRD (Figure 6.3(1) and Raman (Figure 6.3(2)) spectra of GnP, GO and f-GO series. In XRD spectra of Figure 6.3(1), M25 shows typical diffraction peak at $2\theta = 26.4$ ° and

this value corresponds with an interlayer distance of 3.4 Å. However, M25-GO shows a broader peak at lower 2θ = 10.1 ° that corresponds with a larger interlayer distance of 8.8 Å due to the oxidation induced inter-gallery space (ie. interlayer distance between graphene layers) expansion process. That means the oxygen-containing functional groups on GO and the absorbed moisture due to the functional groups can influence the interlayer distance between graphene sheets of GO. Conversely, the f-GO series showed two diffraction peaks on their spectra in comparison with GnP and GO. The peaks are observed at 2θ = 12.0 ° and 23.4 ° on DA-GO, 2θ = 11.3 ° and 22.3 ° on tBA-GO, and 2θ = 12.8 ° and 25.9 ° on 2NA-GO, respectively. Based on the results, DA-GO has two different interlayer distance of 3.8 and 7.4 Å, tBA-GO has a distance of 4.0 and 7.8 Å, and 2NA-GO has a distance of 3.4 and 6.9 Å. This phenomenon can be explained by the reduction of M25-GO occurred during the functionalization process by the amine groups. Reduced graphene oxide (rGO) indicated a weak diffraction peak at around 2θ = 25.8 °, which corresponds with the (002) planes of rGO. This diffraction pattern is distinct to present the amorphous structure of rGO.[168] As a result, the amine groups led to the both of the reduction and functionalization of M25-GO. Furthermore, 2NA-GO shows slightly lower interlayer distance in comparison with DA-GO and tBA-GO. This lower inter-gallery space was attributed to the strong π- π interactions of 2NA molecules which give rise to the higher inter-molecular attraction and stacking of the phenyl groups on each other. [49, 146, 169, 170] Consequently, the XRD spectrum indicates the amine functionalization of GO would predominantly occur at the edge of Cl-GO due to the acyl chloride on the side. Thus, the amine groups can be also more likely to be placed on the edges than inside of Cl-GO by the reaction. This biased distribution of the amine groups seems to lead to the two different interlayer distances.

In Figure 6.3 (2), the Raman spectra of the samples indicated the specific peaks at 1350 and 1591

cm^{-1}, which correspond to the D and G band, respectively. The G band is associated with the first-order scattering of the E_{2g} mode due to the stretching of the C-C bond in graphitic carbon while the D band is associated with defects in the graphene structure.[171] The integrity of the graphene structure is evaluated by the I_D/I_G ratio of the samples. M25 presented strong G band and had the I_D/I_G ratio of 0.23 while M25-GO showed higher D band and I_D/I_G ratio of 0.98 than M25. This means that the oxidization process for M25-GO led to the formation of high amount of defects on the graphene structure. However, DA-GO, tBA-GO, and 2NA-GO indicated higher I_D/I_G ratio than M25-GO such as 1.25 (DA-GO), 1.21 (tBA-GO), and 1.23 (2NA-GO) respectively. This phenomenon means that the reduction of GO occurred on f-GO series during the functionalization process. These results of Raman correspond with the XRD results and are in accordance with various studies conducted on the difference between GO and rGO in terms of the I_D/I_G ratio. For instance, Guijing Liu et al,[168] reported that the I_D/I_G ratio of rGO increased in comparison with GO because the average size of the sp^2 domains decreased while the number of these domains increased. Furthermore, Hua Feng et al,[172] demonstrated that the I_D/I_G ratio of rGO increased up to 1.18 from 0.67 of the ratio of GO. They explained this fact by the formation of some degree of amorphous phase of rGO in the carbon lattice of GO during the reduction process. In fact, XRD and Raman spectra in Figure 6.3 might not fully explain that reduction of GO occurred during the functionalization process of f-GO. Nevertheless, the existence of the reduction that occurred on f-GO can be inferred by these results.

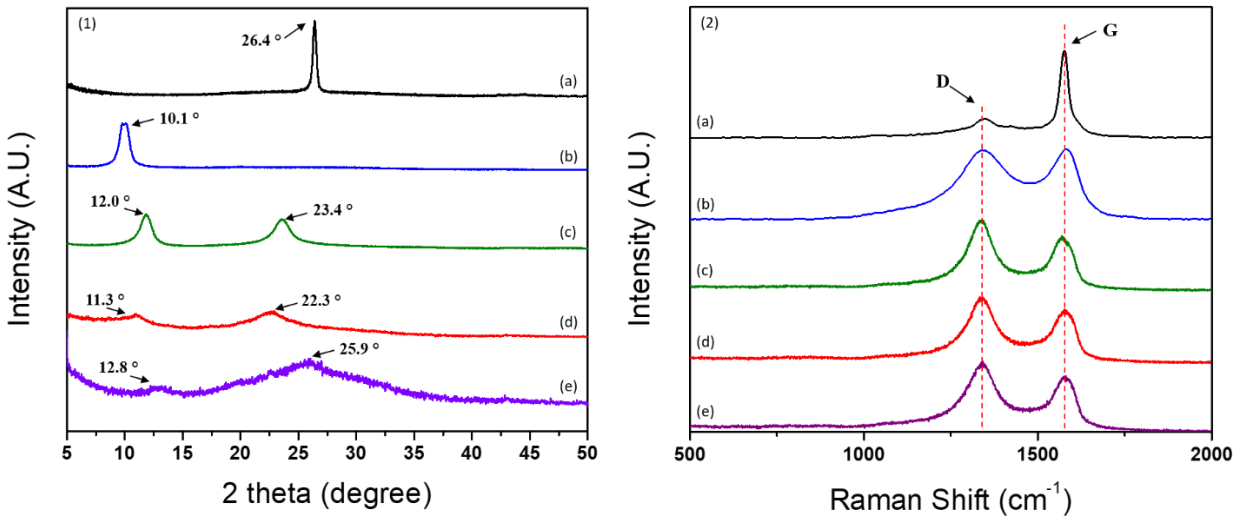

Figure 6.3. (1) XRD and (2) Raman spectra for the GnP, GO, and f-GO series; (a) M25, (b) M25-GO, (c) DA-GO, (d) tBA-GO, and (e) 2NA-GO.

The FT-IR spectra of GO and f-GO series are shown in Figure 6.4 (1) and magnified spectra for the range of 3050 to 2800 cm^{-1} and 1900 to 1400 cm^{-1} are shown in Figure 6.4 (2) and 6.4 (3), respectively. In Figure 6.4 (2), the peaks at 2954 cm^{-1}, 2923 cm^{-1}, and 2845 cm^{-1} were detected in the sample of DA-GO and tBA-GO. They are associated with the asymmetrical and symmetrical stretching vibrations of hydrocarbon groups. Conversely, the peaks at 2960 cm^{-1}, 2902 cm^{-1}, and 2869 cm^{-1} were slightly observed in the sample of 2NA-GO which are in regards to =C-H stretching band.[173] GO-M25 in Figure 6.4(3), (b) shows functional groups; 1720 ~1740 cm^{-1} regarding stretching band of carbonyl group (C=O), 3420 cm^{-1} indicating hydroxyl group (-OH), and 1590~1620 cm^{-1} associated with C=C, and 1250 cm^{-1} regarding C-O stretching vibrations,[150] while M25 shows no specific peaks in the FT-IR spectrum. On the spectrum of the f-GO series, the new peak was detected at 1650 cm^{-1} for the three f-GO and this peak is associated with C=O stretching band in the amide group. Besides, other new peaks were observed in the f-GO series at 1585 cm^{-1} and 1450 cm^{-1} regarding N-H stretching vibration and C-N stretching band,

respectively.[31, 32, 173] These peaks are representative of the result of the chemical reaction between GO and the three types of amine groups. Consequently, FT-IR results of GnP, GO, and f-GO series indicate that the amine functionalization of GO successfully occurred and the amine groups were covalently bonded to the edge of GO layers.

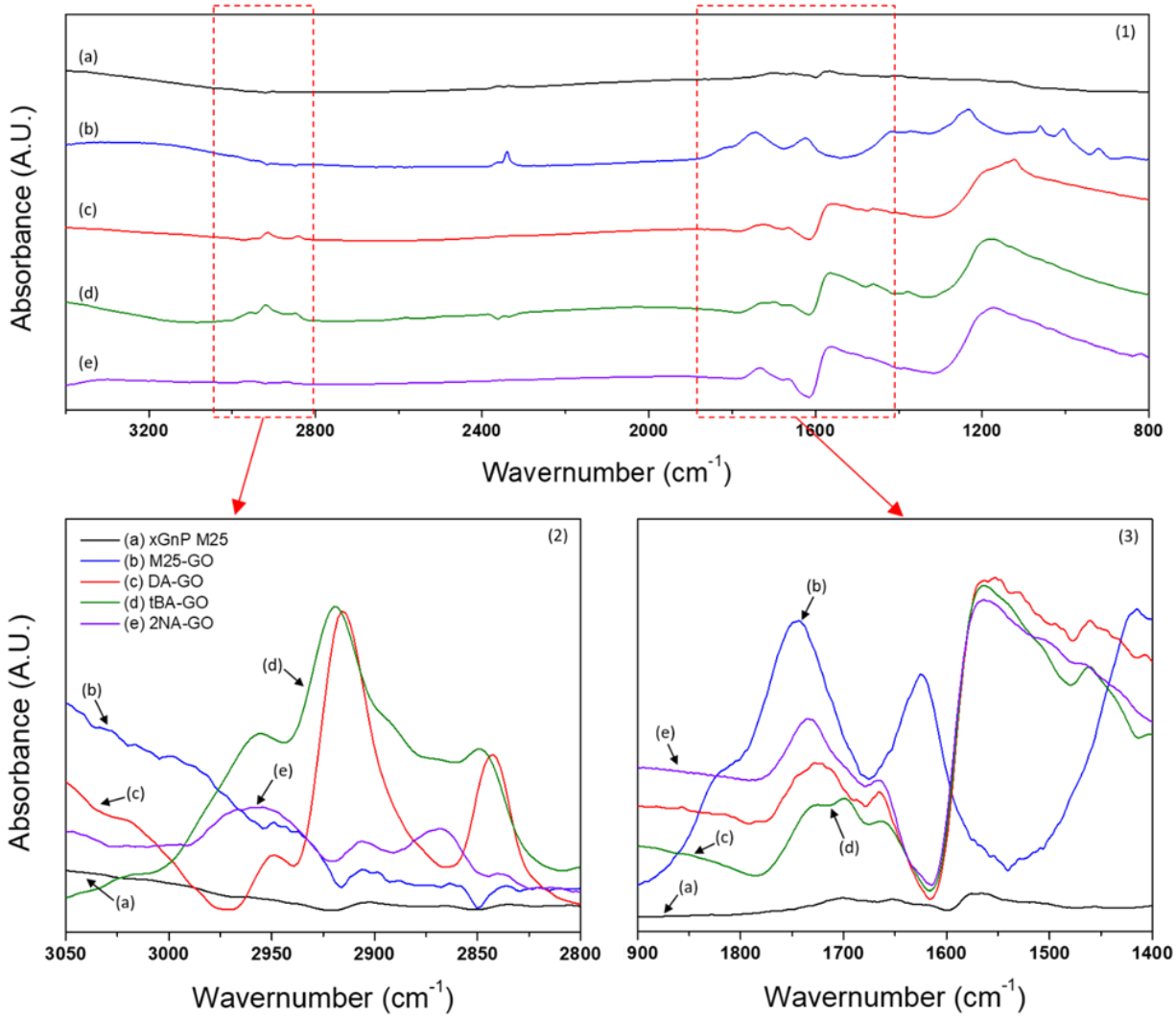

Figure 6.4. FT-IR spectra for the GnP, GO, and f-GO series; (a) M25, (b) M25-GO, (c) DA-GO, (d) tBA-GO, and (e) 2NA-GO.

Figure 6.5 presents the TGA and DTG results of all of the samples which were conducted in air

and nitrogen. f-GO series show the lower weight loss than GO at the whole temperature range regardless of the gas. This is because the oxygen-containing functional groups on GO are thermally weak, thus, their decomposition can start at the temperature around 150 °C.[125] DTG in Figure 6.5 (1-2) and 6.5 (2-2) clearly shows the decomposition temperature of M25-GO starting around 150 °C. Conversely, f-GO indicates a relatively lower and broader peaks than M25-GO. This means that f-GO is thermally stable due to the strong covalent bonding between the amine groups and graphene. In addition, the reduction of f-GO series by the functionalization process can also contribute to the improvement of the thermal stability. In TGA results of Figure 6.5 (1-1) and 6.5 (1-2), M25-GO has 88.42 % of weight at 100 °C in air condition while DA-GO, tBA-GO, and 2NA-GO have 98.9 %, 99.2, and 99.5 % of weight at the same condition, respectively. This high weight loss of M25-GO is attributed to the evaporation of the water molecules absorbed by the hydrophilic functional groups on GO. At 200 °C in air condition, the weight of GO was dramatically decreased to 55.7 % while the weight of DA-GO, tBA-GO, and 2NA-GO was slightly decreased to 92.6 %, 84.3 %, and 93.0 %, respectively. In addition, GO showed 52.4 % of weight while DA-GO, tBA-GO, and 2NA-GO indicated 95.0 %, 88.0 %, and 91.3 % of weight at 200 °C in N_2 condition. In these results, DA-GO and 2NA-GO showed relatively high thermal resistance than tBA-GO. Herein, it seems that the thermal stability of f-GO depends on the molecular structure and weight. tBA-GO indicates the highest weight loss because of its short chain length and small molecular weight. DA-GO showed a slightly higher weight of 95.0 % than 91.3 % of 2NA-GO in nitrogen while DA-GO indicated a similar weight of 92.6 % as 93.0 % of 2NA-GO in air condition. This is because the molecular weight is more dominant in the weight loss in the inert gas condition while DA group would be more vulnerable to oxidation in air condition than 2NA. Therefore, the molecular weight and structure of the amine functional groups would be a critical

design factor for the modification of GO. The specific results of TGA are shown in Table A.1 of Appendix A.

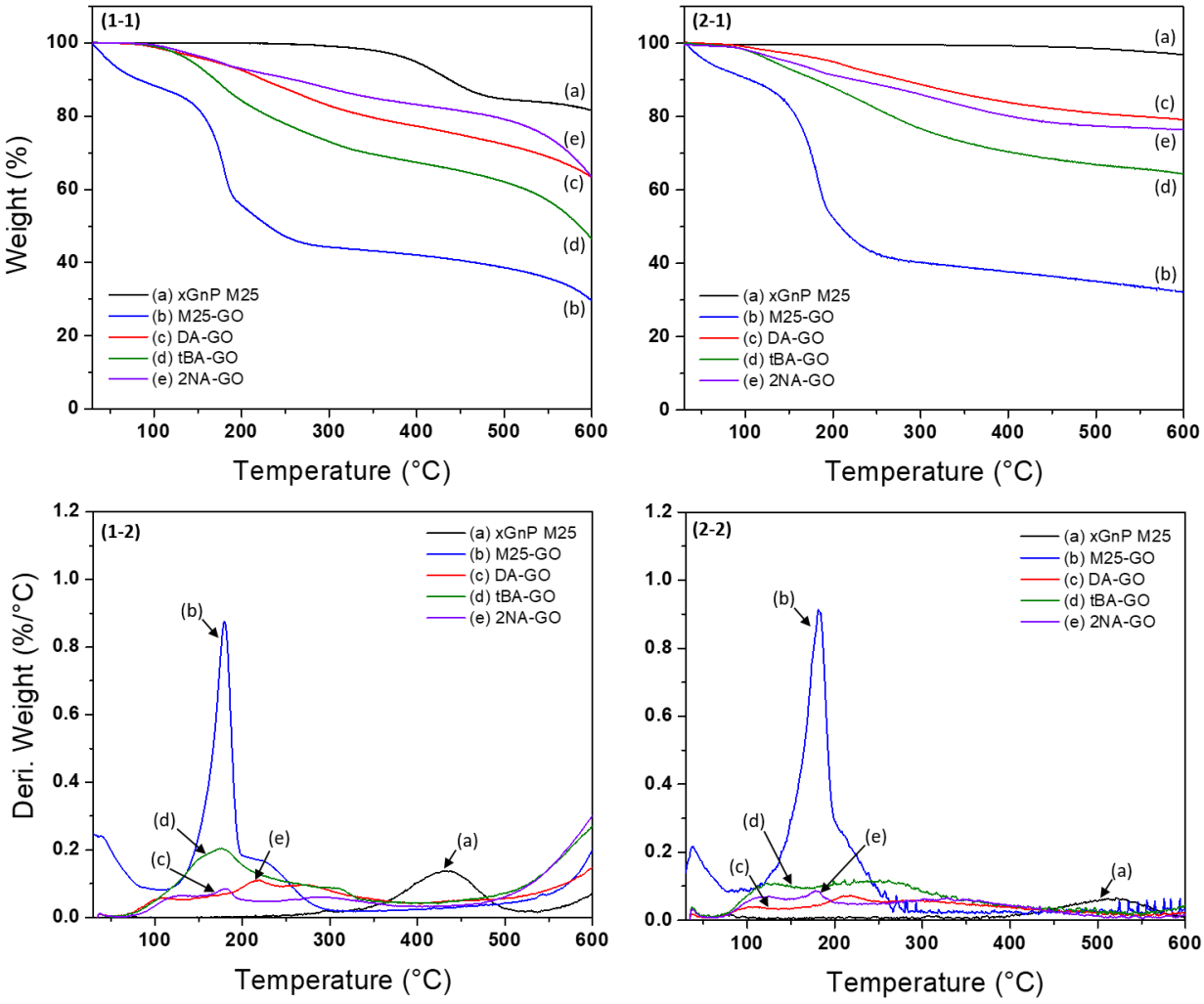

Figure 6.5. TGA and DTG results for the GnP, GO, and f-GO series; (1-1) TGA, (1-2) DTG in air condition and (2-1) TGA, (2-2) DTG in N_2 condition.

6.3.2 Morphology of PU/GnP and PU/GO composites

Figure 6.6 shows the morphologies of the cross-sectional area for PU nanocomposites incorporated with the GnP and f-GO series. In Figure 6.6 (b) the larger particle size of M25 in PU/M25

composite with respect to the primary particle size of M25 can be attributed to the coagulation and worse dispersion during the sample preparation process. Conversely, PU/f-GO nanocomposites (Figure 6.6 (c) to (e)) indicate the inherent size of M25 which means f-GO series was relatively well dispersed into the PU matrix than the pure GnP (M25) Moreover, in the PU/DA-GO and PU/tBA-GO nanocomposites, some spaces were found in the interface between the PU matrix and fillers. However, 2NA-GO was strongly attached to the PU matrix, thus, the crack was found on the PU matrix rather than the interface. It seems that the aromatic component of 2NA-GO is more attractive with the PU matrix than the hydrocarbon component of DA-GA and tBA-GO. This attraction can be explained by that the aromatic component of PU from MDI can build the π-π interaction.[174] This interaction force would be higher than the effect of the chain entanglement between the PU matrix and hydrocarbon chains of DA-GO and tBA-GO. For this reason, PU/DA-GO indicated a better interface than PU/tBA-GO nanocomposite based on the hydrocarbon length of the amine group. Nevertheless, the SEM image of the PU/2NA-GO nanocomposite is insufficient to provide direct proof of π-π interaction between 2NA and the PU matrix. However, this interaction can be an available candidate to explain the improved interfacial adhesion of the PU/2NA-GO nanocomposite.

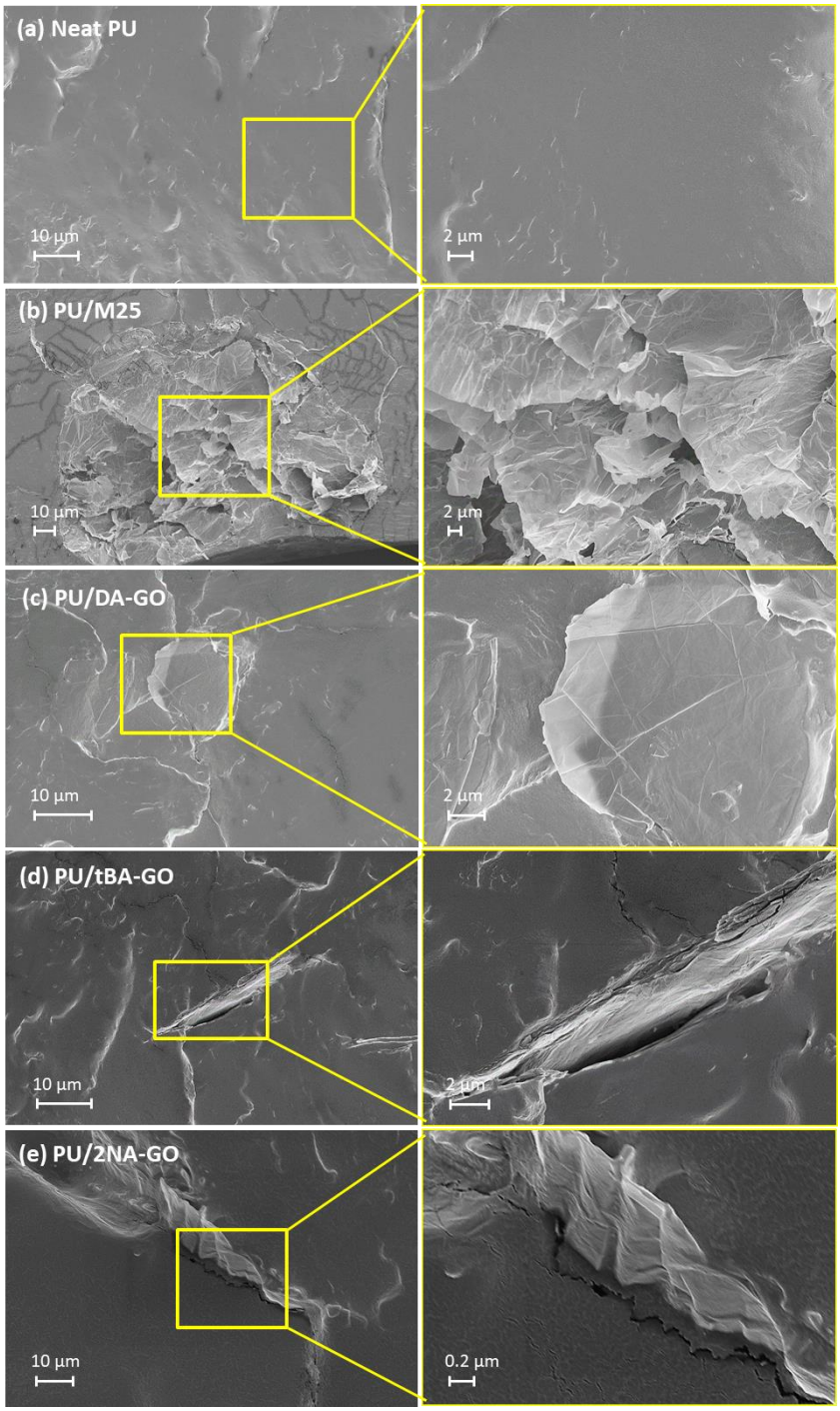

Figure 6.6. Cross-sectional SEM images for the (a) neat PU, (b) PU/M25, and the PU/f-GO nanocomposites such as (c) PU/DA-GO, (d) PU/tBA-GO, and (e) PU/2NA-GO. (The yellow boxes indicate magnified images for a specific area)

6.3.3 Mechanical properties of the nanocomposites

The mechanical properties of the PU nanocomposites are tabulated in Table 6.2. Figure 6.7 shows the comparison of the tensile modulus and hardness of the PU nanocomposites. The strain-stress curves for the nanocomposites are shown in Figure A.5 of Appendix A. The tensile modulus of neat PU was slightly improved from 1.87 MPa to 2.06 MPa with the incorporation of M25 in the PU matrix. Furthermore, the hardness of the nanocomposite was also slightly improved from 17.0 to 18.6 in Shore D. However, the tensile strength and elongation at break of PU/M25 decreased because the tensile stress is determined by the maximum strain in an elastic material. Thus, the low tensile strength was attributed to the low elongation at break. The tensile modulus of the PU/2NA-GO nanocomposite was significantly improved up to 4.17 MPa and this is about 2.2 times higher than the neat PU while the tensile stress was decreased as explained above. Moreover, the hardness of PU/2NA-GO was also improved around 1.5 times with respect to the neat PU. Herein, the tensile modulus trend of the nanocomposites is comparable with the hardness of the nanocomposites. This is because the tensile modulus of polymeric materials is associated with hardness or stiffness of the materials. Several empirical models have been suggested to explain this correlation between the tensile modulus and the hardness.[77, 78] According to equation 3-2 in chapter 3.2 that is generally used for the correlation, the tensile modulus is proportional to the hardness of Shore D. Therefore, the higher tensile modulus of the PU nanocomposites can lead to the higher hardness of the composites. Nevertheless, PU/DA-GO and PU/tBA-GO composites showed a decreased tensile modulus and hardness. This is because the mechanical properties of the nanocomposites strongly depend on interfacial interactions between the polymer matrix and the fillers.[158] PU consists of hard and soft segment in which the hard segment comprises to diphenyl groups from MDI. Thus, PU/2NA-GO nanocomposite has a better interfacial interaction

such as π-π interaction between the diphenyl groups and 2NA-GO.[29, 174, 175] The reinforcing effect due to the π-π interactions within the polymer nanocomposites has been proven by several studies. For instance, Jizhen Zhang et al.[176] reported that graphene sheets improved the mechanical properties of the di-pyrene terminated PEG (polyethylene glycol) due to the π-π interactions. They demonstrated that the aromatic structure of pyrene molecules formed the π-π interactions with graphene sheets. In addition, Bin Shen et al.[30] showed that the π-π interactions facilitated uniform dispersion of graphene in polystyrene (PS) matrix. The PS/graphene composite indicated higher molecular weight than PS because of the attached graphene by the π-π interactions. The high molecular weight of PS/graphene composite could lead to improved mechanical properties. Thus, polymers, which have aromatic-rich groups, can be physically enhanced by the π-π interactions due to graphene sheets. Furthermore, the 2-naphthyl amine group can form a conjugated structure with GO.[49] This conjugated functionalized 2NA-GO is capable to transfer external stress to the graphene sheets in the PU nanocomposites. Conversely, PU/DA-GO and PU/tBA-GO nanocomposites do not obtain a sufficient interfacial interaction between the PU matrix and the fillers. It can be attributed to the lower compatibility between the hydrocarbon component of DA-GO or tBA-GO with the PU matrix, which leads to the limited number of interlacing between polymer chains and the fillers. Besides, PU/DA-GO showed the lower mechanical properties than PU/tBA-GO, this is due to the fact that DA would not build the entanglement with PU matrix and only form its segregated phase on the GO surface since the longer chain length than tBA. In conclusion, the molecular structure and weight of the amine group on f-GO can influence the mechanical properties of the PU nanocomposites. Besides, interfacial interaction with the polymer matrix such as π-π interaction as explained above is required to improve the mechanical properties of the nanocomposites.

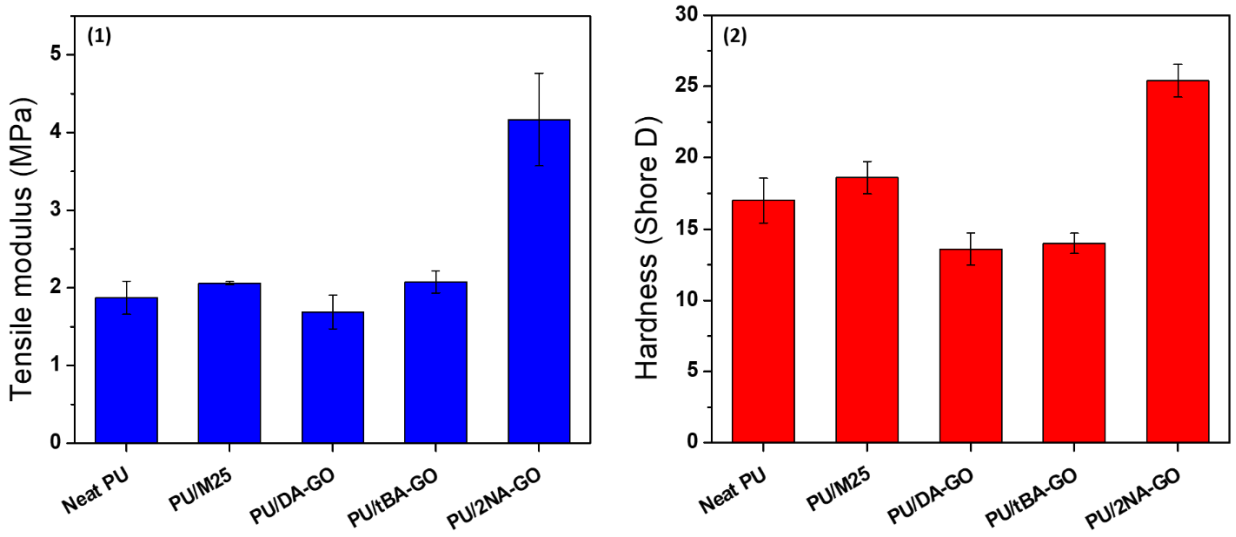

Figure 6.7. Comparison of tensile modulus (1) and hardness in Shore D (2) of the neat PU and PU nanocomposites. (The error bars present standard deviations (n=5))

Table 6.2. Mechanical properties of the neat PU, PU/GNP and PU/f-GO nanocomposites (STD*: Standard deviation for 5 samples)

Samples	Tensile modulus (MPa ± STD*)	Tensile strength (MPa ± STD*)	Elongation at break (%)	Hardness (Shore D ± STD*)
Neat PU	1.87 ± 0.21	6.12 ± 0.51	560	17.0 ±1.6
PU/M25	2.06 ± 0.02	3.75 ± 0.43	388	18.6 ± 1.1
PU/DA-GO	1.69 ± 0.22	1.91 ± 0.17	228	13.6 ± 1.1
PU/tBA-GO	2.08 ± 0.14	2.92 ± 0.63	445	14.0 ± 0.7
PU/2NA-GO	4.17 ± 0.60	4.28 ± 0.57	306	25.4 ± 1.1

6.3.4 Electrochemical properties of PU/GnP and PU/GO nanocomposites

Tafel polarization curve was obtained by cyclic voltammetry (CV) to evaluate the corrosion resistance of the neat PU and the PU nanocomposites. Corrosion potential (E_{corr}) and corrosion current (I_{corr}) can be extracted from the Tafel plot and the corrosion resistance of the samples can

be quantitatively compared by the parameters. For example, the anti-corrosion performance of the materials is explained by the increase and decrease in E_{corr} and I_{corr}, respectively.[126] E_{corr} and I_{corr} are obtained by the point of the intersection between the extrapolated cathodic and anodic curves from the plot. Tafel plots for the samples were shown in Figure 6.8 and the parameters from the plots were summarized in Table 6.3.

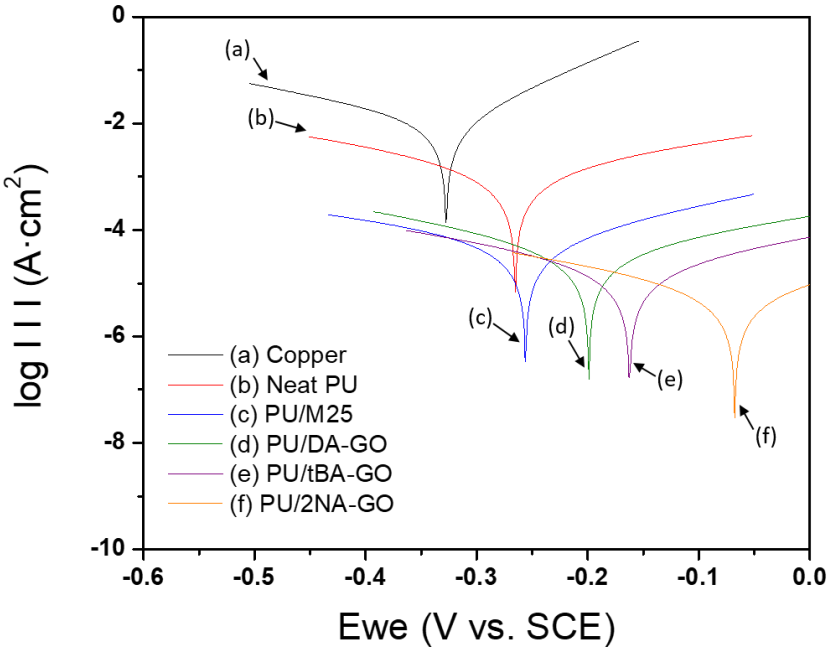

Figure 6.8. Tafel plots for the pristine Cu substrate and the neat PU, PU/M25, and PU/f-GO nanocomposites; PU/DA-GO, PU/tBA-GO, and PU/2NA-GO.

In Figure 6.8, PU/M25 nanocomposite indicated a slightly higher E_{corr} of 265.341 mV and a lower I_{corr} of 1.633 μA than the copper substrate (E_{corr}: 327.50 mV, I_{corr}: 10.89 μA). However, the PU nanocomposites with the f-GO series indicated the higher E_{corr} and lower I_{corr} than PU/M25 nanocomposite. This means PU/f-GO nanocomposites indicate better corrosion resistance than PU/M25. This is because the f-GO series was more uniformly dispersed in the polymer matrix because of the less agglomeration than M25. This fact was confirmed by the SEM results. Thus,

the better dispersion resulted in a high surface area. For this reason, the relative uniform dispersion of f-GO considerably contributes to building a filler arrangement efficiently and this effect can mitigate to diffuse a corrosive agent within the nanocomposite.[158] Besides, PU/2NA-GO composites indicated the highest E_{corr} and lowest I_{corr}. It seems that the aromatic component of 2NA can transfer the corrosive agent to graphene sheets based on the interfacial interaction. Therefore, PU/2NA-GO showed the highest corrosion resistance due to the two effects such as the filler dispersion and the interfacial interaction.

Polarization resistance (R_p) was used as another parameter to compare the corrosion resistance. R_p was determined by the Stern-Geary equation 3-3 in chapter 3.[126] Additionally, protection efficiency (P_{EF}) given by equation 4-4 in chapter 4 was also utilized to evaluate the anti-corrosion performance of a metal substrate coated with the polymeric materials.[126] In comparison to the neat PU, the PU/f-GO nanocomposites showed the greater value of R_p and P_{EF}. Specifically, PU/DA-GO and PU/tBA-GO nanocomposites indicated R_p of 2835.1 $\Omega \cdot cm^2$ and 2925.1 $\Omega \cdot cm^2$, respectively. Besides, PU/2NA-GA nanocomposite showed a considerably high R_p value of 7060.6 $\Omega \cdot cm^2$ in comparison to the value of the two nanocomposites. This high R_p of PU/2NA-GO can be due to not only the good compatibility between the PU matrix and 2NA-GO, but also due to the reduction of GO by 2NA, which leads to restore the conjugation structure of graphene resulting in higher electrochemical property of graphene than other nanocomposites. In addition, the P_{EF} value of PU/2NA-GO increased by up to 99.9 %. Based on these results, the 2NA component on 2NA-GO contributed to the more uniform dispersion within the PU matrix and resulted in the mitigation of the corrosion occurrence and improvement of mechanical properties.

Table 6.3. The parameters obtained from Tafel plots

Samples	E_{corr} (mV vs. SCE)	I_{corr} ($\mu A/cm^2$)	b_a (mV/dec)	b_c (mV/dec)	R_p ($\Omega \cdot cm^2$)	R_{corr} (MPY)	P_{EF} (%)
Cu	-327.5	10.890	114.6	248.0	3.1	4.957	-
Neat PU	-265.3	1.633	365.4	322.5	45.6	0.074	87.0
PU/M25	-200.4	0.040	334.5	294.8	1701.0	0.018	99.7
PU/DA-GO	-172.6	0.024	334.5	294.8	2835.1	0.011	99.8
PU/tBA-GO	-162.4	0.023	305.3	314.6	2925.1	0.011	99.8
PU/2NA-GO	-67.9	0.007	227.2	228.1	7060.6	0.003	99.9

Electrochemical impedance spectroscopy (EIS) was performed to characterize the corrosion resistance of materials for supporting the Tafel plot. EIS measurement was required an equivalent circuit model to fit with an acquired impedance data. The equivalent circuit models for Cu and coated Cu substrate are shown Figure 6.9.[177] This model in this chapter was more simple than the model, which was used in chapters 4 and 5. This is because the simple model is more useful for comparing the anti-corrosion performance of protective layers with high corrosion resistance.[178, 179] For this reason, the simple model without Warburg impedance (W) was used for the equivalent circuit model of Cu substrate with the PU protective layers. In Figure 6.9, R_s presents the solution resistance, R_{ct} presents the polarization resistance of Cu substrate which relates to the charge-transfer resistance, and R_{film} presents the charge-transfer resistance of the protective layer. Q_{dl} represents the capacitance of the interface between Cu and solution interface and Q_{film} represents the capacitance of the protective layer. Figure 6.10 illustrates the Nyquist plots for the bare Cu substrate and PU/GnP on Cu.

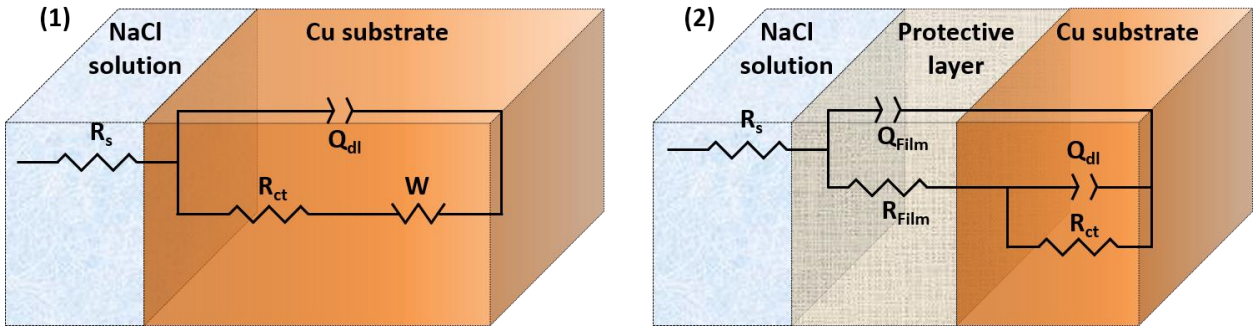

Figure 6.9. Equivalent circuit model: [1] neat Cu and [2] Cu substrate coated with protective layer using the PU nanocomposites.

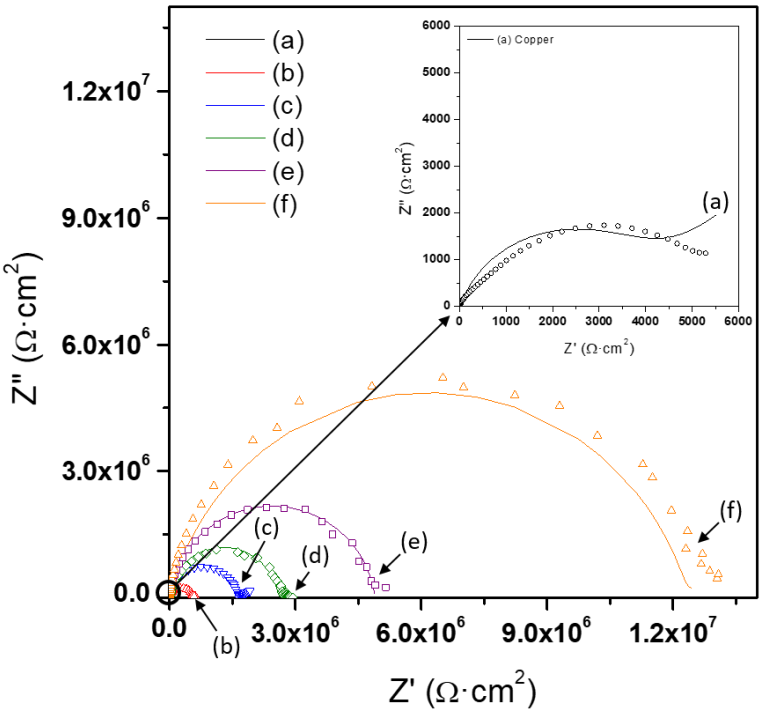

Figure 6.10. Nyquist plots (dotted lines: acquired data, solid lines; fitting curve with the equivalent circuit); (a) Cu substrate, (b) the neat PU, (c) PU/M25, (d) PU/DA-GO, (e) PU/tBA-GO, (f) PU/2NA-GO.

In the Nyquist plot, the corrosion resistance of materials is associated with the diameter of the semicircle. Herein, polarization resistance regarding charge-transfer resistance of the corrosive

agent is converted to the diameter of the plot, thus the charge-transfer resistance (R_{ct}) and the resistance of the protective layer (R_{film}) are attributed to the corrosion resistance. Therefore, a larger semicircle diameter corresponds with higher corrosion resistance. Subsequently, the pure Cu showed the typical plot and the R_{ct} presented 3720 kΩ·cm^2.[126, 177] The coated Cu with the neat PU showed R_{film} of 141,000 kΩ·cm^2 which means the PU coating layer protects the Cu substrate against the corrosive agents. Besides, PU/M25 composite layer indicated the higher value of R_{film} than the neat PU as 271,000 kΩ·cm^2, thus, the GnP within the PU matrix was effective in mitigating the corrosion on Cu substrate. Furthermore, PU composite layers, including the f-GO series, indicated the greater value of R_{film} than PU/M25 and PU/2NA-GO layer showed the highest value of R_{film} among the samples as 6,530,000 kΩ·cm^2. This is because f-GO was better dispersed in the PU matrix than M25 as confirmed by SEM. Thus, this dispersion led to the higher corrosion resistance. In addition, the interfacial interaction between 2NA and PU matrix in PU/2NA-GO seems to have a synergetic effect in terms of the corrosion resistance. As a result, the Nyquist plot showed similar results of the Tafel plot and the filler dispersion and the interface between the fillers and matrix could influence the corrosion resistance of the nanocomposite layer. Besides, the aromatic component on GO seems to be more effective in mitigating the corrosion that occurs due to the interfacial interaction such as π-π interactions. The schematic image in Figure 6.11 represents the interfacial interaction between 2NA-GO and the PU matrix within the nanocomposites. In addition, the parameters of the equivalent circuit extracted the Nyquist plot were shown in Table 6.4.

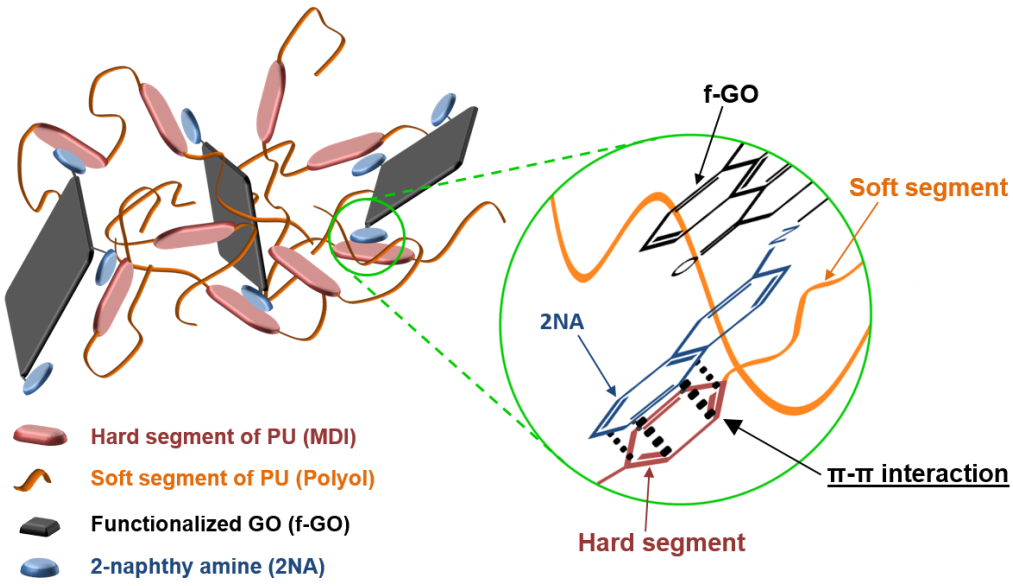

Figure 6.11. Schematic image of the development of interfacial interactions (π-π interactions) between 2NA-GO and the PU matrix within the composites.

Table 6.4. Acquired equivalent circuit parameters extracted from Nyquist plots

Samples	R_s ($\Omega \cdot cm^2$)	R_{ct} ($\Omega \cdot cm^2$)	Q_{dl} ($\Omega^{-1} \cdot S^{n1} \cdot cm^{-2}$)	n1	R_{film} ($\Omega \cdot cm^2$)	Q_{film} ($\Omega^{-1} \cdot S^{n2} \cdot cm^{-2}$)	n2	W ($\Omega^{-1} \cdot S^{n1} \cdot cm^{-2}$)
Cu	9.0	3.72E+03	4.29E-05	0.74	-	-	-	1016
Neat PU	8.7	4.35E+05	1.98E-09	0.91	1.41E+05	1.45E-10	0.72	-
PU/M25	9.2	1.40E+06	5.07E-10	0.96	2.71E+05	1.05E-10	0.71	-
PU/DA-GO	9.0	2.56E+06	6.12E-10	0.97	1.88E+05	2.73E-10	0.78	-
PU/tBA-GO	9.1	5.01E+06	1.05E-10	0.88	6.49E+05	5.10E-10	0.60	-
PU/2NA-GO	9.2	1.26E+07	1.71E-08	0.82	6.53E+06	1.48E-09	0.66	-

6.3.5 Structure and thermal analysis of the PU composites.

Figure 6.12 presents the XRD results of the neat PU and the PU nanocomposites. The neat PU in Figure 6.12(a) indicated a broad peak around 20 ° and this broadness of PU was due to the amorphous phase in PU based on the soft segment.[32, 38, 180] PU/M25 nanocomposite in Figure 6.12(b) showed a small peak at 2θ = 26.7 ° and this peak is coincident with the inherent peak of

M25. This is because the dispersion process of the fillers was insufficient to exfoliate M25 as confirmed by SEM. Thus, their original shape remained within the PU matrix. However, the XRD spectra of the PU/f-GO nanocomposites (Figure 6.12 (c) to (e)) showed no significant peaks and indicated a similar pattern of the neat PU. This is because the intrinsic peak of the f-GO series had lower intensities than the neat PU based on the low loading effect (0.5 wt%) which means the more exfoliated layer of the f-GO series than M25 has remained in PU matrix without coagulation of the fillers. Furthermore, DSC was used to observe the polymeric structure change of the PU nanocomposites on the temperature range from -30 °C to 250 °C. However, there was no significant difference between the neat PU and the PU nanocomposites with GnP and f-GO series. This means the fillers did not affect the PU structure consisting of hard and soft segments during the polymerization process. Besides, the TGA results in Table 6.5 indicated that the PU/f-GO nanocomposites showed a slightly lower temperature at the initial 5% weight loss ($T_{5\%}$) in air condition. In N_2 atmosphere, however, the PU/f-GO nanocomposites showed an identical temperature with the neat PU at the initial 5% weight loss. It seems that the amine groups on GO resulted in the oxygen-induced decomposition in the air condition. This is because the smaller molecular weight of the amine groups would be decomposed faster than the neat PU in the air condition. The DSC and TGA curves are shown in Figure A.6 and A.7 of Appendix A, respectively.

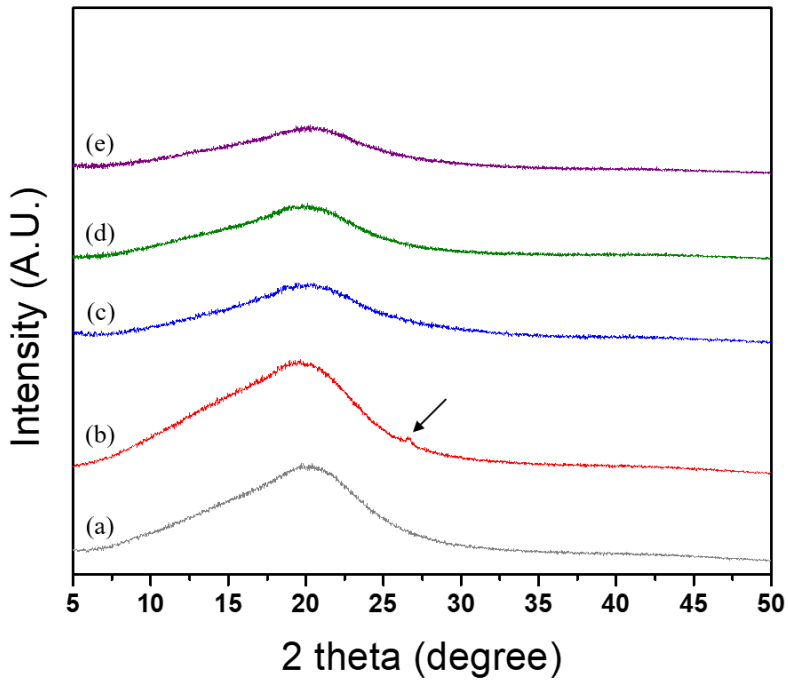

Figure 6.12. XRD spectra for (a) the neat PU, (b) PU/M25, and the PU/f-GO composites such as (c) PU/DA-GO, (d) PU/tBA-GO, and (e) PU/2NA-GO.

Table 6.5. TGA results of the neat PU, PU/GNP and PU/f-GO nanocomposites

Samples	**Neat PU**	**PU/M25**	**PU/DA-GO**	**PU/tBA-GO**	**PU/2NA-GO**
$T_{5\%}$ in Air (°C)	274	273	267	271	271
$T_{5\%}$ in N_2 (°C)	273	278	274	276	276
T_{max} in Air (°C)	330	312	322	330	311
T_{max} in N_2 (°C)	366	359	343	351	355

6.4 Conclusion

In this study, GO was successfully functionalized using amine functional groups with different molecular structure and weight. Two aliphatic (DA and tBA) and one aromatic (2NA) groups were used to functionalize GO and they have different molecular weights and structures. The functionalization was carried out via Cl-GO intermediate, and the effect of the functional groups

on the mechanical properties and corrosion resistance of the PU composites was analyzed. The PU/f-GO composites showed better dispersion in the PU matrix than PU/M25 due to the higher compatibility of functional groups on GO with the PU matrix. 2NA-GO indicated a significant improvement in the tensile modulus up to 123 % compared to neat PU. Besides, protection efficiency (P_{EF}) of PU/2NA-GO increased up to 99.9 % from 86.9 % of neat PU. This is because the diphenyl groups of 2NA-GO provided π-π interaction to improve the interfacial properties between the fillers and the PU matrix. Therefore, the interfacial interaction led to the synergistic effect on mechanical properties and the corrosion resistance of the nanocomposite. Conversely, PU composites with DA-GO and tBA-GO showed similar tensile modulus of neat PU (1.87 MPa). Moreover, they indicated lower hardness than the neat PU (17.0); 13.6 of PU/DA-GO and 14.0 of PU/tBA-GO. This is because DA-GO and tBA-GO had a low interfacial interaction with PU, and the aliphatic molecular structure was less compatible with the PU matrix than 2NA-GO. Furthermore, the high molecular weight of DA-GO in the aliphatic group resulted in more coagulation of the filler than the low molecular weight of tBA-GO. This fact was confirmed by SEM. In conclusion, this study revealed that the molecular structure and weight of functional groups on GO influenced compatibility with the PU matrix. In particular, these results can provide practical insight into the design of pipeliners in oil-sands transportation industries.

7. Conclusions and Recommendations

7.1 Conclusions

In this thesis, polyurethane (PU) nanocomposites containing graphene have been developed to enhance conventional PU pipeliners for oil sands transportation. The anti-corrosiveness and mechanical properties of PU pipeliners had to be reinforced to surmount corrosive and abrasive condition during the transportation of oil sands slurry. In this regards, graphene contributed to improving both properties of PU pipeliners due to its excellent mechanical and gas barrier properties. These enhanced properties of pipeliners utilizing the PU/graphene nanocomposites are very effective in terms of cost-effectiveness and management. Three research phases have been carried out for this research objective.

In phase 1, the size effect of graphene nanoplatelets (GnP) was studied in terms of the filler dispersion. In this study, the filler dispersion by the average diameter of GnP was investigated on the mechanical and anti-corrosion properties of PU/GnP nanocomposites. Four different types of GnP were used to fabricate the PU/GnP nanocomposites. The 4 GnP had a distinct average diameter; 100 μm for H100, 25 μm for M25, 5 μm for M5, and under 2 μm for C750. This research demonstrated that C750, which has the smallest diameter, significantly contributed to improving the anti-corrosion performance of PU nanocomposites. Protection efficiency (P_{EF}) of PU/C750 increased up to 99.6 % from 97.5 % of neat PU. This is because C750 was more uniformly dispersed within the PU matrix than other GnP. Therefore, the uniform dispersion of C750 in the PU matrix built a complicated pathway to suppress the diffusion of corrosive agents. However, C750 was not effective to reinforce mechanical properties of PU/GnP nanocomposites. This fact was due to the insufficient interfacial adhesion between GnP and the PU matrix. On the other hand,

PU/H100, which has the largest GnP, showed 28 % higher tensile modulus than neat PU. This is because the high aspect ratio of H100 contributed to the improvement of the tensile modulus, which is a small range of deformation. In this chapter, it was found that the size of GnP was a critical factor to influence the dispersion of GnP within the PU matrix. Besides, anti-corrosion performance of PU/GnP nanocomposites strongly depended on this effect. However, the interfacial adhesion between GnP and the PU matrix needs to be improved to enhance mechanical properties. In phase 2, graphene oxide (GO) was synthesized from GnP of phase 1 to improve the interfacial adhesion between GnP and the PU matrix. Various hydrophilic functional groups, such as hydroxyl (-OH), carbonyl (-C=O), and epoxy (-C-O-C-) groups, were found on GO. These functional groups contributed to reducing the number of graphene layers and forming interfacial interaction with the PU matrix, such as hydrogen bonding. These effects of GO led to the improvement in both mechanical and anti-corrosion properties of PU nanocomposites. Specifically, PU/GO indicated the higher tensile modulus of 53 % and hardness of 40 % than neat PU. Besides, P_{EF} of PU/GO increased up to 99.9 % from 98.9 % of neat PU. In this study, it was found that large GO (GO-M25) indicated the improvement of mechanical and anti-corrosion properties in comparison to PU/GO-C750 containing small GO. This result was associated with the formation of the hard-segment in PU/GO nanocomposites. This is because hydrophilic functional groups on GO could provide a nucleation site for forming the hard segment. Thus, the extremely high surface area of GO-C750 could also provide numerous nucleation sites for the hard segment. The hard segment size was decreased by this effect result, inducing the insufficient elasticity of PU nanocomposites. Consequently, GO improved both the mechanical and anti-corrosion properties of PU/GO while the large size was more effective. However, GO was thermally unstable rather than GnP due to the decomposition of the hydrophilic functional groups. Therefore, this challenge of GO needs to be

improved for the application of pipeliners based on the hot oil sands slurry (~80 °C). In phase 3, amine functionalized GO (f-GO) was synthesized from GO in phase 2 to improve the thermal stability of GO by maintaining high interfacial interaction with the PU matrix. 3 different amine groups were used to synthesize f-GO; docecyl (DA) and *tert*-butyl (tBA) groups as aliphatic amine groups, and 2-naphthyl group (2NA) as an aromatic amine group. TGA results confirmed that 3 f-GO indicated higher thermal stability than GO regardless gas conditions (air and N_2). Among the PU/f-GO nanocomposites, PU/2NA-GO indicated the most improved mechanical properties and anti-corrosion performance. Specifically, the tensile modulus and hardness of PU/2NA-GO increased up to 123 % and 49 % from neat PU. P_{EF} of PU/2NA-GO improved up to 99.9 % from 86.9 % of neat PU. This improvement was attributed to π-π interaction between the PU matrix and 2NA. π-π interaction resulted in stacking aromatic groups between 2NA and phenyl groups from isocyanate part of the PU matrix. This interaction led to a synergetic effect on both mechanical and anti-corrosion properties of the nanocomposite. In consequence, this study demonstrated that the PU/f-GO nanocomposites including aromatic components on f-GO can contribute to improvement in both mechanical and anti-corrosion properties. This fact is due to the π-π interaction among the aromatic components of f-GO and the PU matrix.

In conclusion, the 3 research phases demonstrated critical factors in the development of PU pipeliners for transporting oil sand slurries utilizing PU/GnP nanocomposites. It was found that the filler dispersion and interfacial interaction are crucial factors to improve mechanical and anti-corrosion properties of PU/GnP nanocomposites. Among the crucial factors, the aromatic component significantly contributed to improving both properties of nanocomposites due to uniform filler dispersion and interfacial interaction, such as π-π interaction. Therefore, these studies in this thesis can particularly provide a practical insight into the development of PU

pipeliners in industries of oil sands transportation. In subsequent, a plan for scale-up is required as further research for the practical application of PU pipeliners. Moreover, material research on PU and fillers is continuously needed to improve the performance of nanocomposites.

7.2 Recommendations

For further research on this thesis, two recommendations can be conducted in terms of material (PU and fillers) and scale-up plans. The first recommendation is for the development of a new filler including an extremely high aspect ratio, and the application of PU prepared by prepolymer method (PU prepolymer). This recommendation is for further improving the overall properties of the PU/GnP nanocomposites. The second recommendation is for the development of a scalable production method for synthesizing fillers and casting PU/GnP pipeliners on the pipe inside. This recommendation is for the practical usage of PU/GnP in the view of industries. The recommended future works will be more discussed in the next session.

7.2.1 Material research

In chapter 4, it was found that the mechanical and anti-corrosion properties of the PU/GnP nanocomposites was associated with the aspect ratio and the diameter of GnP, respectively. GnP, which has a higher aspect ratio, indicated a higher tensile modulus while the small GnP contributed to improving the anti-corrosion performance of the nanocomposites. In this regard, graphene nanoribbon (GNR) can be a good candidate to further improve both mechanical and anti-corrosion properties of the PU nanocomposites. GNR can provide a small size but an extremely high aspect ratio because GNR is derived by opening carbon nanotubes (CNT). This high aspect ratio of GNR is different to the aspect ratio of GnP. GNR provides a length to width aspect ratio while GnP provides a diameter to thickness aspect ratio due to the disk shape of GnP. Specifically, GNR has

the length to width aspect ratio of 380 with a thickness of ~4 nm while GnP has around 1 for the length to width aspect ratio with a thickness of 40 ~ 60 nm.[181, 182] Therefore, the PU/GNR nanocomposites can be expected to indicate a further enhancement of both mechanical and anti-corrosion properties. Besides, functionalization of GNR with aromatic amine groups will significantly improve both properties of the nanocomposites based on the study in chapter 6. For this reason, GNR would be an excellent design factor for the next version of PU nanocomposites. For PU research, PU prepolymer can provide a higher mechanical and anti-corrosion properties than PU prepared by one-step method, which is used in this thesis. As mentioned in chapter 2, the overall properties of PU prepolymer are greater than PU by one-step method. This is because moistures and unreacted isocyanates are few remained in PU prepolymer. Consequently, the combination of PU prepolymer and GNR is capable of further enhancing the overall properties of the PU nanocomposites. Several research topics for the two recommendations are suggested as below;

- For the study of the PU/GNR nanocomposites, it is needed to investigate a method of GNR synthesis; CNT is usually used as a starting material for GNR synthesis, and modified Hummer's method is typically used to open the CNT wall. Specific experimental conditions for opening CNT are required to set up.

- For the study of PU prepolymer, it is needed to contact PU prepolymer manufacturers and compare their products; physical properties of the products are needed to compare based on technical data sheets provided from the manufacturers. After selection of several PU prepolymers, the PU/GNR nanocomposites will be fabricated and compared with the PU/GnP composites in terms of mechanical and anti-corrosion properties.

7.2.2 Scale-up plan

In chapter 6, the synthesis method of f-GO via the Cl-GO intermediate is a suitable method for the lab scale. Under certain conditions, GO can be directly converted to f-GO.[183] However, the direct reaction of f-GO requires precise control and a limited number of functional groups, which is applicable to this reaction. Therefore, simple control for processing and available functional groups is critical to scale-up plan for f-GO synthesis. For this objective, it is necessary to design a continuous process from GO synthesis to the f-GO synthesis. In addition, a practical coating process for pipeliners utilizing the PU/f-GO nanocomposites is necessary to consider in the view of industries. In chapter 2, pipeliners are formed by centrifugal casting method inside the pipe. Therefore, it needs to investigate rheological properties such as viscosity of the PU/f-GO mixture before casting. This research will be useful to prevent a coating problem such as thickness variations or pinholes. There are specific suggestions to achieve these research topics as below:

- It is necessary to establish a re-circulation system for continuous f-GO synthesis. In general, the synthesis process of GO consists of several steps, such as mixing, conversion, and cooling/slurry control. In these processes, the final GO slurry can be re-circulated to the conversion step for the functionalization of GO, rendering f-GO products to be scalable and practical.

- The in-situ ATR-IR method can be utilized during the functionalization of GO to observe the f-GO reaction process. This method is useful for real-time monitoring of GO functionalization. The final f-GO products would be reliable on their properties.

- It is necessary to investigate rheological properties of the PU/f-GO nanocomposites for a flawless coating layer. This is because the coating quality strongly depends on rheological

properties of the nanocomposites such as viscosity variations and viscoelasticity. These rheological properties are very important in industries and they can be characterized by rheometers such as capillary, rotational, and extensional rheometers. Among the rheometers, rotational rheometer is suitable for the initial study because it can provide viscosity variations in a wide range of shear rate.

References

[1] Liu, J., Gao, Y., Cao, D., Zhang, L., Guo, Z., Nanoparticle dispersion and aggregation in polymer nanocomposites: insights from molecular dynamics simulation, Langmuir, **27**, 7926-7933, (2011).

[2] Friedrich, K., Fakirov, S., Zhang, Z., Polymer composites: from nano-to macro-scale, Springer Science & Business Media (2005).

[3] Kuilla, T., Bhadra, S., Yao, D., Kim, N. H., Bose, S., Lee, J. H., Recent advances in graphene based polymer composites, Progress in Polymer Science, **35**, 1350-1375, (2010).

[4] Theng, B., Polymer–clay nanocomposites, Developments in clay science, Elsevier (2012).

[5] Mikitaev, A. K., Ligidov, M. K., Zaikov, G. E., Polymers, polymer blends, polymer composites and filled polymers: Synthesis, properties and applications, Nova Publishers (2006).

[6] Mittal, V., Polymer-graphene nanocomposites, Royal Society of Chemistry (2012).

[7] Zhu, Y., Murali, S., Cai, W., Li, X., Suk, J. W., Potts, J. R., Ruoff, R. S., Graphene and graphene oxide: synthesis, properties, and applications, Adv Mater, **22**, 3906-3924, (2010).

[8] Potts, J. R., Dreyer, D. R., Bielawski, C. W., Ruoff, R. S., Graphene-based polymer nanocomposites, Polymer, **52**, 5-25, (2011).

[9] Song, W.-L., Wang, W., Veca, L. M., Kong, C. Y., Cao, M.-S., Wang, P., Meziani, M. J., Qian, H., LeCroy, G. E., Cao, L., Sun, Y.-P., Polymer/carbon nanocomposites for enhanced thermal transport properties – carbon nanotubes versus graphene sheets as nanoscale fillers, Journal of Materials Chemistry, **22**, 17133, (2012).

[10] Li, X., Deng, H., Li, Z., Xiu, H., Qi, X., Zhang, Q., Wang, K., Chen, F., Fu, Q., Graphene/thermoplastic polyurethane nanocomposites: Surface modification of graphene through oxidation, polyvinyl pyrrolidone coating and reduction, Compos Part A Appl Sci

Manuf, **68**, 264-275, (2015).

[11] Nguyen, D. A., Lee, Y. R., Raghu, A. V., Jeong, H. M., Shin, C. M., Kim, B. K., Morphological and physical properties of a thermoplastic polyurethane reinforced with functionalized graphene sheet, Polym. Int., **58**, 412-417, (2009).

[12] Xu, Y., Hong, W., Bai, H., Li, C., Shi, G., Strong and ductile poly(vinyl alcohol)/graphene oxide composite films with a layered structure, Carbon, **47**, 3538-3543, (2009).

[13] Cooper, D. R., D'Anjou, B., Ghattamaneni, N., Harack, B., Hilke, M., Horth, A., Majlis, N., Massicotte, M., Vandsburger, L., Whiteway, E., Experimental review of graphene, ISRN Condensed Matter Physics, (2012).

[14] Choi, W., Lahiri, I., Seelaboyina, R., Kang, Y. S., Synthesis of Graphene and Its Applications: A Review, Critical Reviews in Solid State and Materials Sciences, **35**, 52-71, (2010).

[15] Lerf, A., He, H., Forster, M., Klinowski, J., Structure of graphite oxide revisited, The Journal of Physical Chemistry B, **102**, 4477-4482, (1998).

[16] Cai, D., Jin, J., Yusoh, K., Rafiq, R., Song, M., High performance polyurethane/functionalized graphene nanocomposites with improved mechanical and thermal properties, Compos. Sci. Technol., **72**, 702-707, (2012).

[17] Kumar, S. K., Castro, M., Saiter, A., Delbreilh, L., Feller, J. F., Thomas, S., Grohens, Y., Development of poly(isobutylene-co-isoprene)/reduced graphene oxide nanocomposites for barrier, dielectric and sensingapplications, Materials Letters, **96**, 109-112, (2013).

[18] Martin-Gallego, M., Verdejo, R., Lopez-Manchado, M. A., Sangermano, M., Epoxy-Graphene UV-cured nanocomposites, Polymer, **52**, 4664-4669, (2011).

[19] Sadasivuni, K. K., Ponnamma, D., Kumar, B., Strankowski, M., Cardinaels, R., Moldenaers, P., Thomas, S., Grohens, Y., Dielectric properties of modified graphene oxide filled

polyurethane nanocomposites and its correlation with rheology, Compos. Sci. Technol., **104**, 18-25, (2014).

[20] Tripathi, S. N., Saini, P., Gupta, D., Choudhary, V., Electrical and mechanical properties of PMMA/reduced graphene oxide nanocomposites prepared via in situ polymerization, Journal of materials science, **48**, 6223-6232, (2013).

[21] Wang, J., Wang, X., Xu, C., Zhang, M., Shang, X., Preparation of graphene/poly(vinyl alcohol) nanocomposites with enhanced mechanical properties and water resistance, Polym. Int., **60**, 816-822, (2011).

[22] Hu, J., Ji, Y., Shi, Y., Hui, F., Duan, H., Lanza, M., A review on the use of graphene as a protective coating against corrosion, Ann. J. Mater. Sci. Eng, **1**, 16, (2014).

[23] Liu, S., Gu, L., Zhao, H., Chen, J., Yu, H., Corrosion resistance of graphene-reinforced waterborne epoxy coatings, Journal of Materials Science & Technology, **32**, 425-431, (2016).

[24] Giesy, J. P., Anderson, J. C., Wiseman, S. B., Alberta oil sands development, Proceedings of the National Academy of Sciences, **107**, 951-952, (2010).

[25] Papavinasam, S., Corrosion control in the oil and gas industry, Elsevier (2013).

[26] Perez, T. E., Corrosion in the oil and gas industry: an increasing challenge for materials, Jom, **65**, 1033-1042, (2013).

[27] Pourhashem, S., Vaezi, M. R., Rashidi, A., Bagherzadeh, M. R., Exploring corrosion protection properties of solvent based epoxy-graphene oxide nanocomposite coatings on mild steel, Corrosion Science, **115**, 78-92, (2017).

[28] Qi, K., Sun, Y., Duan, H., Guo, X., A corrosion-protective coating based on a solution-processable polymer-grafted graphene oxide nanocomposite, Corrosion Science, **98**, 500-506, (2015).

[29] Rochefort, A., Wuest, J. D., Interaction of substituted aromatic compounds with graphene, Langmuir, **25**, 210-215, (2008).

[30] Shen, B., Zhai, W., Chen, C., Lu, D., Wang, J., Zheng, W., Melt Blending In situ Enhances the Interaction between Polystyrene and Graphene through π–π Stacking, ACS Applied Materials & Interfaces, **3**, 3103-3109, (2011).

[31] Jing, Q., Liu, W., Pan, Y., Silberschmidt, V. V., Li, L., Dong, Z., Chemical functionalization of graphene oxide for improving mechanical and thermal properties of polyurethane composites, Materials & Design, **85**, 808-814, (2015).

[32] Bandyopadhyay, P., Park, W. B., Layek, R. K., Uddin, M. E., Kim, N. H., Kim, H.-G., Lee, J. H., Hexylamine functionalized reduced graphene oxide/polyurethane nanocomposite-coated nylon for enhanced hydrogen gas barrier film, J. Membr. Sci., **500**, 106-114, (2016).

[33] Jordan, J., Jacob, K. I., Tannenbaum, R., Sharaf, M. A., Jasiuk, I., Experimental trends in polymer nanocomposites—a review, Materials Science and Engineering: A, **393**, 1-11, (2005).

[34] Anwar, Z., Kausar, A., Rafique, I., Muhammad, B., Advances in Epoxy/Graphene Nanoplatelet Composite with Enhanced Physical Properties: A Review, Polymer-Plastics Technology and Engineering, **55**, 643-662, (2015).

[35] Chatterjee, S., Nafezarefi, F., Tai, N. H., Schlagenhauf, L., Nüesch, F. A., Chu, B. T. T., Size and synergy effects of nanofiller hybrids including graphene nanoplatelets and carbon nanotubes in mechanical properties of epoxy composites, Carbon, **50**, 5380-5386, (2012).

[36] Geim, A. K., Novoselov, K. S., The rise of graphene, Nature materials, **6**, 183-191, (2007).

[37] Kim, H., Abdala, A. A., Macosko, C. W., Graphene/Polymer Nanocomposites, Macromolecules, **43**, 6515-6530, (2010).

[38] Kim, H., Miura, Y., Macosko, C. W., Graphene/Polyurethane Nanocomposites for Improved

Gas Barrier and Electrical Conductivity, Chemistry of Materials, **22**, 3441-3450, (2010).

[39] Kitipornchai, S., He, X., Liew, K., Continuum model for the vibration of multilayered graphene sheets, Physical Review B, **72**, 075443, (2005).

[40] Pinto, A. M., Cabral, J., Tanaka, D. A. P., Mendes, A. M., Magalhães, F. D., Effect of incorporation of graphene oxide and graphene nanoplatelets on mechanical and gas permeability properties of poly (lactic acid) films, Polym. Int., **62**, 33-40, (2013).

[41] Wu, H., Drzal, L. T., Graphene nanoplatelet paper as a light-weight composite with excellent electrical and thermal conductivity and good gas barrier properties, Carbon, **50**, 1135-1145, (2012).

[42] Sciences, X., Overview of XG Sciences and Our Materials, 1-33, (2012).

[43] Dreyer, D. R., Park, S., Bielawski, C. W., Ruoff, R. S., The chemistry of graphene oxide, Chem Soc Rev, **39**, 228-40, (2010).

[44] Medhekar, N. V., Ramasubramaniam, A., Ruoff, R. S., Shenoy, V. B., Hydrogen bond networks in graphene oxide composite paper: structure and mechanical properties, Acs Nano, **4**, 2300-2306, (2010).

[45] Yousefi, N., Lin, X., Zheng, Q., Shen, X., Pothnis, J. R., Jia, J., Zussman, E., Kim, J.-K., Simultaneous in situ reduction, self-alignment and covalent bonding in graphene oxide/epoxy composites, Carbon, **59**, 406-417, (2013).

[46] Song, X., Yang, Y., Liu, J., Zhao, H., PS colloidal particles stabilized by graphene oxide, Langmuir, **27**, 1186-1191, (2011).

[47] Shen, B., Zhai, W., Tao, M., Lu, D., Zheng, W., Chemical functionalization of graphene oxide toward the tailoring of the interface in polymer composites, Compos. Sci. Technol., **77**, 87-94, (2013).

[48] Wassei, J. K., Cha, K. C., Tung, V. C., Yang, Y., Kaner, R. B., The effects of thionyl chloride on the properties of graphene and graphene–carbon nanotube composites, Journal of Materials Chemistry, **21**, 3391, (2011).

[49] Zhuang, X. D., Chen, Y., Liu, G., Li, P. P., Zhu, C. X., Kang, E. T., Noeh, K. G., Zhang, B., Zhu, J. H., Li, Y. X., Conjugated-polymer-functionalized graphene oxide: synthesis and nonvolatile rewritable memory effect, Adv Mater, **22**, 1731-5, (2010).

[50] Akindoyo, J. O., Beg, M. D. H., Ghazali, S., Islam, M. R., Jeyaratnam, N., Yuvaraj, A. R., Polyurethane types, synthesis and applications – a review, RSC Adv., **6**, 114453-114482, (2016).

[51] Zokay, S., Fergusont. J. Polyurethane elastomers, Prog. Polym. Sci, **16**, 695-836, (1991).

[52] Mertiny, P., Juss, K., Bell, T., Corrosion and erosion resistant polymer composite pipe for oil sands hydrotransport, CORROSION 2008, NACE International, (2008).

[53] Clemitson, I., Castable polyurethane elastomers, CRC Press (2015).

[54] Prisacariu, C., Scortanu, E., Agapie, B., New insights into polyurethane elastomers obtained by changing the polyaddition procedures, Proceedings of the World Congress on Engineering, (2011).

[55] Calebrese, C., Hui, L., Schadler, L. S., Nelson, J. K., A review on the importance of nanocomposite processing to enhance electrical insulation, IEEE Transactions on Dielectrics and Electrical Insulation, **18**, 938-945, (2011).

[56] Tadmor, Z., Gogos, C. G., Principles of polymer processing, John Wiley & Sons (2013).

[57] Talbot, D. E., Talbot, J. D., Corrosion science and technology, CRC press (2007).

[58] Forsgren, A., Corrosion control through organic coatings, CRC Press (2006).

[59] Ahmad, Z., Principles of corrosion engineering and corrosion control, Elsevier (2006).

[60] Sato, N., Basics of corrosion chemistry, Jonh Wiley & Sons, New York, (2012).

[61] Landolt, D., Corrosion and surface chemistry of metals, EPFL press (2007).

[62] Davis, J. R., Corrosion: Understanding the basics, Asm International (2000).

[63] Burkes, D. O., Rubber polyurethane liner, US Patents, US14066908 (2016).

[64] Jelinek, J., Watkinson, C., Cold Wall Effect Testing of an Internal Pipeline Coating for In-situ Application, CORROSION-NATIONAL ASSOCIATION OF CORROSION ENGINEERS ANNUAL CONFERENCE-, NACE, (1999).

[65] Weiss, M. D., Christoffersen, S. W., Corrosion test assembly, US Patents, US4563427, (1986).

[66] Veleva, L., Protective coatings and inorganic anti-corrosion pigments, Paint coat. Test. Manual, ASTM International, (2012).

[67] Smith, T., A review of carbon black pigments, Pigment & Resin Technology, **12**, 14-16, (1983).

[68] Lloyd, G. E., Atomic number and crystallographic contrast images with the SEM: a review of backscattered electron techniques, Mineralogical Magazine, **51**, 3-19, (1987).

[69] Guinier, A., X-ray diffraction in crystals, imperfect crystals, and amorphous bodies, Courier Corporation (1994).

[70] Malard, L., Pimenta, M., Dresselhaus, G., Dresselhaus, M., Raman spectroscopy in graphene, Physics reports, **473**, 51-87, (2009).

[71] Krishnamoorthy, K., Veerapandian, M., Yun, K., Kim, S. J., The chemical and structural analysis of graphene oxide with different degrees of oxidation, Carbon, **53**, 38-49, (2013).

[72] Perumbilavil, S., Sankar, P., Priya Rose, T., Philip, R., White light Z-scan measurements of ultrafast optical nonlinearity in reduced graphene oxide nanosheets in the 400–700 nm region, Applied Physics Letters, **107**, 051104, (2015).

[73] Gabbott, P., Principles and applications of thermal analysis, John Wiley & Sons (2008).

[74] Pavia, D. L., Lampman, G. M., Kriz, G. S., Vyvyan, J. A., Introduction to spectroscopy, Cengage Learning (2008).

[75] Campbell, J., Nicole, N., Stein, O., Liu, Y., Lu, Y., Jiang, L. J., Three-dimensional printing and deformation behavior of low-density target structures by two-photon polymerization, (2017).

[76] Young, R. J., Lovell, P. A., Introduction to polymers, CRC press (2011).

[77] Flores, A. e., Calleja, F. B., Attenburrow, G., Bassett, D., Microhardness studies of chain-extended PE: III. Correlation with yield stress and elastic modulus, Polymer, **41**, 5431-5435, (2000).

[78] Mix, A., Giacomin, A., Standardized polymer durometry, Journal of Testing and evaluation, **39**, 696-705, (2011).

[79] Meththananda, I. M., Parker, S., Patel, M. P., Braden, M., The relationship between Shore hardness of elastomeric dental materials and Young's modulus, Dent Mater, **25**, 956-9, (2009).

[80] Bard, A. J., Faulkner, L. R., Leddy, J., Zoski, C. G., Electrochemical methods: fundamentals and applications, wiley New York (1980).

[81] Kakaei, K., Esrafili, M. D., Ehsani, A., Graphene and Anticorrosive Properties, in: K. Kakaei, M.D. Esrafili, A. Ehsani (Eds.), Interface Science and Technology, Elsevier (2019).

[82] Stern, M., Discussion of Electrochemical Polarization, Journal of The Electrochemical Society, **104**, 751-752, (1957).

[83] Randviir, E. P., Banks, C. E., Electrochemical impedance spectroscopy: an overview of bioanalytical applications, Analytical Methods, **5**, 1098-1115, (2013).

[84] Christopher, G., Anbu Kulandainathan, M., Harichandran, G., Comparative study of effect of corrosion on mild steel with waterborne polyurethane dispersion containing graphene oxide

versus carbon black nanocomposites, Progress in Organic Coatings, **89**, 199-211, (2015).

[85] Montemor, M. F., Introduction_Functional and smart coatings for corrosion protection: A review of recent advances, Surface and Coatings Technology, **258**, 17-37, (2014).

[86] Wei, H., Ding, D., Wei, S., Guo, Z., Anticorrosive conductive polyurethane multiwalled carbon nanotube nanocomposites, Journal of Materials Chemistry A, **1**, 10805-10813, (2013).

[87] Davis, J. R., Corrosion: Understanding the basics, ASM International (2000).

[88] Stratmann, M., Feser, R., Leng, A., Introduction_Corrosion protection by organic films, Electrochimica Acta, **39**, 1207-1214, (1994).

[89] Singh, B. P., Jena, B. K., Bhattacharjee, S., Besra, L., Introduction_Development of oxidation and corrosion resistance hydrophobic graphene oxide-polymer composite coating on copper, Surface and Coatings Technology, **232**, 475-481, (2013).

[90] Sørensen, P. A., Kiil, S., Dam-Johansen, K., Weinell, C. E., Introduction_Anticorrosive coatings: a review, Journal of Coatings Technology and Research, **6**, 135-176, (2009).

[91] Chang, C.-H., Huang, T.-C., Peng, C.-W., Yeh, T.-C., Lu, H.-I., Hung, W.-I., Weng, C.-J., Yang, T.-I., Yeh, J.-M., Novel anticorrosion coatings prepared from polyaniline/graphene composites, Carbon, **50**, 5044-5051, (2012).

[92] Cai, K., Zuo, S., Luo, S., Yao, C., Liu, W., Ma, J., Mao, H., Li, Z., Preparation of polyaniline/graphene composites with excellent anti-corrosion properties and their application in waterborne polyurethane anticorrosive coatings, RSC Adv., **6**, 95965-95972, (2016).

[93] Lyon, S. B., Bingham, R., Mills, D. J., Introduction_Advances in corrosion protection by organic coatings, Progress in Organic Coatings, **102**, 2-7, (2017).

[94] Yeh, J.-M., Liou, S.-J., Lin, C.-Y., Cheng, C.-Y., Chang, Y.-W., Lee, K.-R., Introduction_Anticorrosively enhanced PMMA− clay nanocomposite, Chemistry of materials,

14, 154-161, (2002).

[95] Grundmeier, G., Schmidt, W., Stratmann, M., Introduction_Corrosion protection by organic coatings, Electrochimica Acta, **45**, 2515-2533, (2000).

[96] Ahmad, S., Ashraf, S. M., Sharmin, E., Mohomad, A., Alam, M., Synthesis, formulation, and characterization of siloxane-modified epoxy-based anticorrosive paints, Journal of Applied Polymer Science, **100**, 4981-4991, (2006).

[97] Lu, W.-K., Elsenbaumer, R. L., Wessling, B., Corrosion protection of mild steel by coatings containing polyaniline, Synthetic Metals, **71**, 2163-2166, (1995).

[98] Armelin, E., Alemán, C., Iribarren, J. I., Anticorrosion performances of epoxy coatings modified with polyaniline: A comparison between the emeraldine base and salt forms, Progress in Organic Coatings, **65**, 88-93, (2009).

[99] Talo, A., Forsen, O., Yläsaari, S., Corrosion protective polyaniline epoxy blend coatings on mild steel, Synthetic Metals, **102**, 1394-1395, (1999).

[100] Rostami, M., Rasouli, S., Ramezanzadeh, B., Askari, A., Electrochemical investigation of the properties of Co doped ZnO nanoparticle as a corrosion inhibitive pigment for modifying corrosion resistance of the epoxy coating, Corrosion Science, **88**, 387-399, (2014).

[101] Shi, X., Nguyen, T. A., Suo, Z., Liu, Y., Avci, R., Effect of nanoparticles on the anticorrosion and mechanical properties of epoxy coating, Surface and Coatings Technology, **204**, 237-245, (2009).

[102] Rahman, O. u., Kashif, M., Ahmad, S., Nanoferrite dispersed waterborne epoxy-acrylate: Anticorrosive nanocomposite coatings, Progress in Organic Coatings, **80**, 77-86, (2015).

[103] Heidarian, M., Shishesaz, M. R., Kassiriha, S. M., Nematollahi, M., Characterization of structure and corrosion resistivity of polyurethane/organoclay nanocomposite coatings

prepared through an ultrasonication assisted process, Progress in Organic Coatings, **68**, 180-188, (2010).

[104] Verma, G., Kaushik, A., Ghosh, A. K., Comparative assessment of nano-morphology and properties of spray coated clear polyurethane coatings reinforced with different organoclays, Progress in Organic Coatings, **76**, 1046-1056, (2013).

[105] Vajihinejad, V., Soares, J. B. P., Can We Make Better Polyurethane Composite Foams with Oil Sands Mature Fine Tailing?, Macromolecular Materials and Engineering, **301**, 383-389, (2016).

[106] Ashrafizadeh, H., Mertiny, P., McDonald, A., Evaluation of the effect of temperature on mechanical properties and wear resistance of polyurethane elastomers, Wear, **368**, 26-38, (2016).

[107] Mo, M., Zhao, W., Chen, Z., Yu, Q., Zeng, Z., Wu, X., Xue, Q., Excellent tribological and anti-corrosion performance of polyurethane composite coatings reinforced with functionalized graphene and graphene oxide nanosheets, RSC Adv., **5**, 56486-56497, (2015).

[108] Tian, B. R., Cheng, Y. F., Electrolytic deposition of Ni–Co–Al2O3 composite coating on pipe steel for corrosion/erosion resistance in oil sand slurry, Electrochimica Acta, **53**, 511-517, (2007).

[109] Ray, S. S., Okamoto, M., New polylactide/layered silicate nanocomposites, 6 melt rheology and foam processing, Macromolecular materials and engineering, **12**, 936-944, (2003).

[110] Jun, Y.-S., Sy, S., Ahn, W., Zarrin, H., Rasen, L., Tjandra, R., Amoli, B. M., Zhao, B., Chiu, G., Yu, A., Highly conductive interconnected graphene foam based polymer composite, Carbon, **95**, 653-658, (2015).

[111] Yu, Y.-H., Lin, Y.-Y., Lin, C.-H., Chan, C.-C., Huang, Y.-C., High-performance

polystyrene/graphene-based nanocomposites with excellent anti-corrosion properties, Polym. Chem., **5**, 535-550, (2014).

[112] Geim, A. K., Novoselov, K. S., The rise of graphene, Nature materials, **6**, 183-191, (2007).

[113] Lee, C., Wei, X., Kysar, J. W., Hone, J., Measurement of the elastic properties and intrinsic strength of monolayer graphene, science, **321**, 385-388, (2008).

[114] Du, X., Skachko, I., Barker, A., Andrei, E. Y., Approaching ballistic transport in suspended graphene, Nature nanotechnology, **3**, 491-495, (2008).

[115] Balandin, A. A., Ghosh, S., Bao, W., Calizo, I., Teweldebrhan, D., Miao, F., Lau, C. N., Superior thermal conductivity of single-layer graphene, Nano letters, **8**, 902-907, (2008).

[116] Schriver, M., Regan, W., Gannett, W. J., Zaniewski, A. M., Crommie, M. F., Zettl, A., Graphene as a long-term metal oxidation barrier: worse than nothing, ACS nano, **7**, 5763-5768, (2013).

[117] Raza, M. A., Westwood, A. V. K., Brown, A. P., Stirling, C., Texture, transport and mechanical properties of graphite nanoplatelet/silicone composites produced by three roll mill, Compos. Sci. Technol., **72**, 467-475, (2012).

[118] Yadav, S. K., Cho, J. W., Functionalized graphene nanoplatelets for enhanced mechanical and thermal properties of polyurethane nanocomposites, Applied Surface Science, **266**, 360-367, (2013).

[119] Glover, C. F., Richards, C., Baker, J., Williams, G., McMurray, H. N., Introduction_In-coating graphene nano-platelets for environmentally-friendly corrosion protection of iron, Corrosion Science, **114**, 169-172, (2017).

[120] Jang, B. Z., Zhamu, A., Processing of nanographene platelets (NGPs) and NGP nanocomposites: a review, Journal of Materials Science, **43**, 5092-5101, (2008).

[121] Nieto, A., Lahiri, D., Agarwal, A., Synthesis and properties of bulk graphene nanoplatelets consolidated by spark plasma sintering, Carbon, **50**, 4068-4077, (2012).

[122] Sangaj, N. S., Malshe, V. C., Introduction_Permeability of polymers in protective organic coatings, Progress in Organic Coatings, **50**, 28-39, (2004).

[123] Pinto, A. M., Cabral, J., Tanaka, D. A. P., Mendes, A. M., Magalhães, F. D., Effect of incorporation of graphene oxide and graphene nanoplatelets on mechanical and gas permeability properties of poly(lactic acid) films, Polym. Int., **62**, 33-40, (2013).

[124] King, J. A., Klimek, D. R., Miskioglu, I., Odegard, G. M., Mechanical properties of graphene nanoplatelet/epoxy composites, Journal of Applied Polymer Science, **128**, 4217-4223, (2013).

[125] Li, Y., Zhu, J., Wei, S., Ryu, J., Wang, Q., Sun, L., Guo, Z., Poly(propylene) Nanocomposites Containing Various Carbon Nanostructures, Macromolecular Chemistry and Physics, **212**, 2429-2438, (2011).

[126] Alhumade, H., Abdala, A., Yu, A., Elkamel, A., Simon, L., Corrosion inhibition of copper in sodium chloride solution using polyetherimide/graphene composites, The Canadian Journal of Chemical Engineering, **94**, 896-904, (2016).

[127] Khaled, K. F., Studies of the corrosion inhibition of copper in sodium chloride solutions using chemical and electrochemical measurements, Materials Chemistry and Physics, **125**, 427-433, (2011).

[128] King, J. A., Klimek, D. R., Miskioglu, I., Odegard, G. M., Mechanical properties of graphene nanoplatelet/epoxy composites, Journal of Composite Materials, **49**, 659-668, (2015).

[129] Yue, L., Pircheraghi, G., Monemian, S. A., Manas-Zloczower, I., Epoxy composites with carbon nanotubes and graphene nanoplatelets – Dispersion and synergy effects, Carbon, **78**, 268-278, (2014).

[130] Gonçalves, G., Marques, P. A. A. P., Barros-Timmons, A., Bdkin, I., Singh, M. K., Emami, N., Grácio, J., Graphene oxide modified with PMMA via ATRP as a reinforcement filler, Journal of Materials Chemistry, **20**, 9927, (2010).

[131] Jeong, J. S., Moon, J. S., Jeon, S. Y., Park, J. H., Alegaonkar, P. S., Yoo, J. B., Mechanical properties of electrospun PVA/MWNTs composite nanofibers, Thin Solid Films, **515**, 5136-5141, (2007).

[132] Huang, X., Qi, X., Boey, F., Zhang, H., Graphene-based composites, Chem Soc Rev, **41**, 666-686, (2012).

[133] Du, J., Cheng, H.-M., The Fabrication, Properties, and Uses of Graphene/Polymer Composites, Macromolecular Chemistry and Physics, **213**, 1060-1077, (2012).

[134] Das, T. K., Prusty, S., Graphene-Based Polymer Composites and Their Applications, Polymer-Plastics Technology and Engineering, **52**, 319-331, (2013).

[135] Stankovich, S., Dikin, D. A., Dommett, G. H., Kohlhaas, K. M., Zimney, E. J., Stach, E. A., Piner, R. D., Nguyen, S. T., Ruoff, R. S., Graphene-based composite materials, Nature, **442**, 282-286, (2006).

[136] Young, R. J., Kinloch, I. A., Gong, L., Novoselov, K. S., The mechanics of graphene nanocomposites: A review, Compos. Sci. Technol., **72**, 1459-1476, (2012).

[137] Layek, R. K., Nandi, A. K., A review on synthesis and properties of polymer functionalized graphene, Polymer, **54**, 5087-5103, (2013).

[138] Papageorgiou, D. G., Kinloch, I. A., Young, R. J., Mechanical properties of graphene and graphene-based nanocomposites, Progress in Materials Science, **90**, 75-127, (2017).

[139] Balandin, A. A., Ghosh, S., Bao, W., Calizo, I., Teweldebrhan, D., Miao, F., Lau, C. N., Superior Thermal Conductivity of Single-Layer Graphene, Nano Letters, **8**, 902-907, (2008).

[140] Tjong, S. C., Polymer Composites with Graphene Nanofillers: Electrical Properties and Applications, J. Nanosci. Nanotechnol., **14**, 1154-1168, (2014).

[141] Rafiee, M. A., Rafiee, J., Wang, Z., Song, H., Yu, Z.-Z., Koratkar, N., Enhanced Mechanical Properties of Nanocomposites at Low Graphene Content, ACS Nano, **3**, 3884-3890, (2009).

[142] Verdejo, R., Bernal, M. M., Romasanta, L. J., Lopez-Manchado, M. A., Graphene filled polymer nanocomposites, J. Mater. Chem., **21**, 3301-3310, (2011).

[143] Liu, J., Tao, L., Yang, W., Li, D., Boyer, C., Wuhrer, R., Braet, F., Davis, T. P., Synthesis, characterization, and multilayer assembly of pH sensitive graphene-polymer nanocomposites, Langmuir, **26**, 10068-75, (2010).

[144] Liang, J., Huang, Y., Zhang, L., Wang, Y., Ma, Y., Guo, T., Chen, Y., Molecular-Level Dispersion of Graphene into Poly(vinyl alcohol) and Effective Reinforcement of their Nanocomposites, Advanced Functional Materials, **19**, 2297-2302, (2009).

[145] Jun, Y. S., Um, J. G., Jiang, G., Yu, A., A study on the effects of graphene nano-platelets (GnPs) sheet sizes from a few to hundred microns on the thermal, mechanical, and electrical properties of polypropylene (PP)/GnPs composites, Express Polymer Letters, **12**, 885-897, (2018).

[146] Fang, M., Wang, K., Lu, H., Yang, Y., Nutt, S., Covalent polymer functionalization of graphene nanosheets and mechanical properties of composites, Journal of Materials Chemistry, **19**, 7098, (2009).

[147] Jun, Y.-S., Um, J. G., Jiang, G., Lui, G., Yu, A., Ultra-large sized graphene nano-platelets (GnPs) incorporated polypropylene (PP)/GnPs composites engineered by melt compounding and its thermal, mechanical, and electrical properties, Composites Part B: Engineering, **133**, 218-225, (2018).

[148] Zhao, Y. F., Xiao, M., Wang, S. J., Ge, X. C., Meng, Y. Z., Preparation and properties of electrically conductive PPS/expanded graphite nanocomposites, Compos. Sci. Technol., **67**, 2528-2534, (2007).

[149] Hu, K., Kulkarni, D. D., Choi, I., Tsukruk, V. V., Graphene-polymer nanocomposites for structural and functional applications, Progress in Polymer Science, **39**, 1934-1972, (2014).

[150] Marcano, D. C., Kosynkin, D. V., Berlin, J. M., Sinitskii, A., Sun, Z., Slesarev, A., Alemany, L. B., Lu, W., Tour, J. M., Improved Synthesis of Graphene Oxide, ACS Nano, **4**, 4806-4814, (2010).

[151] Dimiev, A. M., Tour, J. M., Mechanism of Graphene Oxide Formation, ACS Nano, **8**, 3060-3068, (2014).

[152] Paredes, J. I., Villar-Rodil, S., Martínez-Alonso, A., Tascón, J. M. D., Graphene Oxide Dispersions in Organic Solvents, Langmuir, **24**, 10560-10564, (2008).

[153] Zhao, X., Zhang, Q., Chen, D., Lu, P., Enhanced Mechanical Properties of Graphene-Based Poly(vinyl alcohol) Composites, Macromolecules, **43**, 2357-2363, (2010).

[154] Putz, K. W., Compton, O. C., Palmeri, M. J., Nguyen, S. T., Brinson, L. C., High-Nanofiller-Content Graphene Oxide-Polymer Nanocomposites via Vacuum-Assisted Self-Assembly, Advanced Functional Materials, **20**, 3322-3329, (2010).

[155] Razeghi, M., Pircheraghi, G., TPU/graphene nanocomposites: Effect of graphene functionality on the morphology of separated hard domains in thermoplastic polyurethane, Polymer, **148**, 169-180, (2018).

[156] Fernández-d'Arlas, B., Khan, U., Rueda, L., Coleman, J. N., Mondragon, I., Corcuera, M. A., Eceiza, A., Influence of hard segment content and nature on polyurethane/multiwalled carbon nanotube composites, Compos. Sci. Technol., **71**, 1030-1038, (2011).

[157] Lai, Y. S., Tsai, C. W., Yang, H. W., Wang, G. P., Wu, K. H., Structural and electrochemical properties of polyurethanes/polyhedral oligomeric silsesquioxanes (PU/POSS) hybrid coatings on aluminum alloys, Materials Chemistry and Physics, **117**, 91-98, (2009).

[158] Um, J. G., Jun, Y.-S., Alhumade, H., Krithivasan, H., Lui, G., Yu, A., Investigation of the size effect of graphene nano-platelets (GnPs) on the anti-corrosion performance of polyurethane/GnP composites, RSC Adv., **8**, 17091-17100, (2018).

[159] Alhumade, H., Yu, A., Elkamel, A., Simon, L., Abdala, A., Enhanced protective properties and UV stability of epoxy/graphene nanocomposite coating on stainless steel, Express Polymer Letters, **10**, 1034-1046 (2016).

[160] Xu, T., Zhou, S., Cui, S., Song, N., Shi, L., Ding, P., Three-dimensional carbon fiber-graphene network for improved thermal conductive properties of polyamide-imide composites, Composites Part B: Engineering, **178**, 107495, (2019).

[161] Bao, C., Guo, Y., Song, L., Hu, Y., Poly (vinyl alcohol) nanocomposites based on graphene and graphite oxide: a comparative investigation of property and mechanism, Journal of Materials Chemistry, **21**, 13942-13950, (2011).

[162] Han, S., Meng, Q., Qiu, Z., Osman, A., Cai, R., Yu, Y., Liu, T., Araby, S., Mechanical, toughness and thermal properties of 2D material- reinforced epoxy composites, Polymer, **184**, 121884, (2019).

[163] Li, P., Chen, X., Zeng, J.-B., Gan, L., Wang, M., Enhancement of the interfacial interaction between poly(vinyl chloride) and zinc oxide modified reduced graphene oxide, RSC Adv., **6**, 5784-5791, (2016).

[164] Krishnan, D., Kim, F., Luo, J., Cruz-Silva, R., Cote, L. J., Jang, H. D., Huang, J., Energetic graphene oxide: Challenges and opportunities, Nano Today, **7**, 137-152, (2012).

[165] Hu, H., Wang, X., Wang, J., Wan, L., Liu, F., Zheng, H., Chen, R., Xu, C., Preparation and properties of graphene nanosheets–polystyrene nanocomposites via in situ emulsion polymerization, Chemical Physics Letters, **484**, 247-253, (2010).

[166] Dreyer, D. R., Todd, A. D., Bielawski, C. W., Harnessing the chemistry of graphene oxide, Chem Soc Rev, **43**, 5288-301, (2014).

[167] Wen, J. G., Geng, W., Geng, H. Z., Zhao, H., Jing, L. C., Yuan, X. T., Tian, Y., Wang, T., Ning, Y. J., Wu, L., Improvement of Corrosion Resistance of Waterborne Polyurethane Coatings by Covalent and Noncovalent Grafted Graphene Oxide Nanosheets, ACS Omega, **4**, 20265-20274, (2019).

[168] Liu, G., Wang, L., Wang, B., Gao, T., Wang, D., A reduced graphene oxide modified metallic cobalt composite with superior electrochemical performance for supercapacitors, RSC Adv., **5**, 63553-63560, (2015).

[169] Habibpour, S., Zabihirad, J., Mohammadi, N., Mohammadi, H., Modeling of polystyrenic nanoparticles driven β-trans-crystalline efficiency in isotactic polypropylene, RSC Adv., **6**, 72500-72509, (2016).

[170] Yang, Z., Shi, X., Yuan, J., Pu, H., Liu, Y., Preparation of poly (3-hexylthiophene)/graphene nanocomposite via in situ reduction of modified graphite oxide sheets, Applied Surface Science, **257**, 138-142, (2010).

[171] Al Shboul, A. M., Siaj, M., Claverie, J. P., Selective Process To Extract High-Quality Reduced Graphene Oxide Leaflets, ACS Applied Nano Materials, **1**, 5920-5926, (2018).

[172] Feng, H., Wang, X., Wu, D., Fabrication of Spirocyclic Phosphazene Epoxy-Based Nanocomposites with Graphene via Exfoliation of Graphite Platelets and Thermal Curing for Enhancement of Mechanical and Conductive Properties, Industrial & Engineering Chemistry

Research, **52**, 10160-10171, (2013).

[173] Panahi, F., Fareghi-Alamdari, R., Khajeh Dangolani, S., Khalafi-Nezhad, A., Golestanzadeh, M., Graphene GraftedN-Methyl-4-pyridinamine (G-NMPA): An Efficient Heterogeneous Organocatalyst for Acetylation of Alcohols, ChemistrySelect, **2**, 474-479, (2017).

[174] Zhang, Z., Huang, H., Yang, X., Zang, L., Tailoring Electronic Properties of Graphene by π–π Stacking with Aromatic Molecules, The Journal of Physical Chemistry Letters, **2**, 2897-2905, (2011).

[175] Wang, W., Zhang, Y., Wang, Y. B., Noncovalent pipi interaction between graphene and aromatic molecule: structure, energy, and nature, J Chem Phys, **140**, 094302, (2014).

[176] Zhang, J., Xu, Y., Cui, L., Fu, A., Yang, W., Barrow, C., Liu, J., Mechanical properties of graphene films enhanced by homo-telechelic functionalized polymer fillers via π–π stacking interactions, Compos Part A Appl Sci Manuf, **71**, 1-8, (2015).

[177] Peng, S., Zeng, Z., Zhao, W., Li, H., Chen, J., Han, J., Wu, X., Novel functional hybrid silica sol–gel coating for copper protection via in situ thiol–ene click reaction, RSC Adv., **4**, 15776-15781, (2014).

[178] Song, G., Equivalent circuit model for AC electrochemical impedance spectroscopy of concrete, Cement and Concrete Research, **30**, 1723-1730, (2000).

[179] Frankel, G., Electrochemical Techniques in Corrosion: Status, Limitations, and Needs, Journal of Testing and Evaluation, **42**, 517-538, (2014).

[180] Ramezanzadeh, B., Ghasemi, E., Mahdavian, M., Changizi, E., Mohamadzadeh Moghadam, M. H., Covalently-grafted graphene oxide nanosheets to improve barrier and corrosion protection properties of polyurethane coatings, Carbon, **93**, 555-573, (2015).

[181] Esawi, A. M. K., Morsi, K., Sayed, A., Taher, M., Lanka, S., Effect of carbon nanotube (CNT)

content on the mechanical properties of CNT-reinforced aluminium composites, Compos. Sci. Technol., **70**, 2237-2241, (2010).

[182] Ramirez, C., Osendi, M. I., Miranzo, P., Belmonte, M., Figueiredo, F., Castro-Beltrán, A., Terrones, M., Graphene nanoribbon ceramic composites, Carbon, **90**, 207-214, (2015).

[183] McGrail, B. T., Rodier, B. J., Pentzer, E., Rapid Functionalization of Graphene Oxide in Water, Chemistry of Materials, **26**, 5806-5811, (2014).

Appendix A

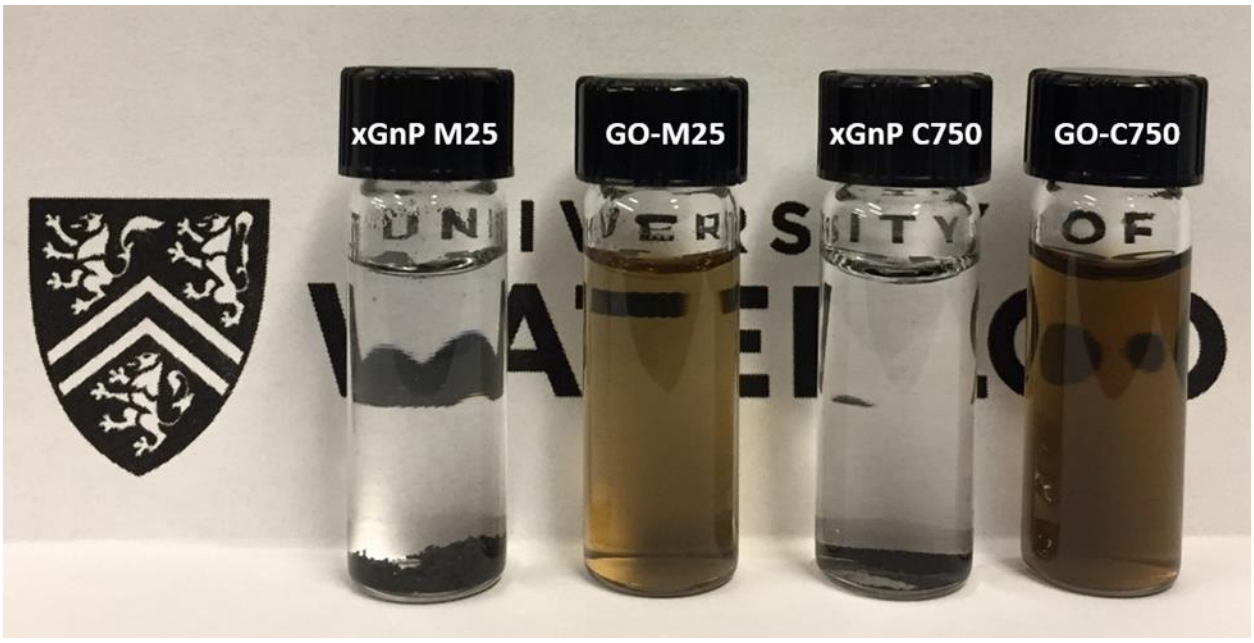

Figure A-1. Images for GnP and GO solution in water at 0.05 wt%.

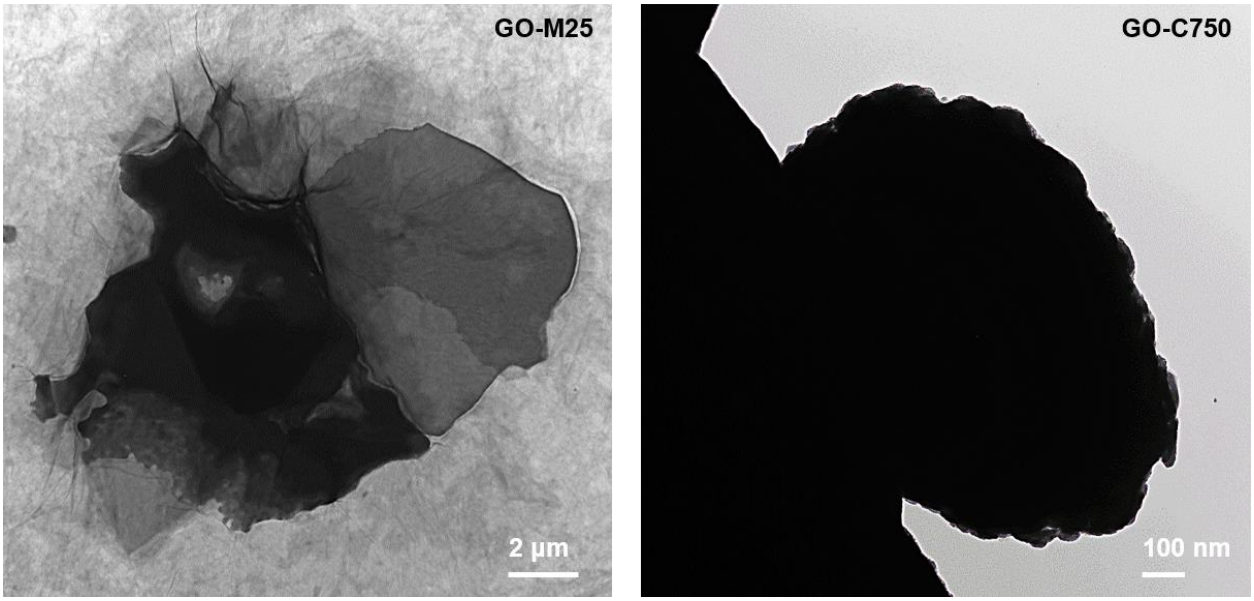

Figure A-2. TEM images for two types of GO; GO-M25 (right) and GO-C750 (left).

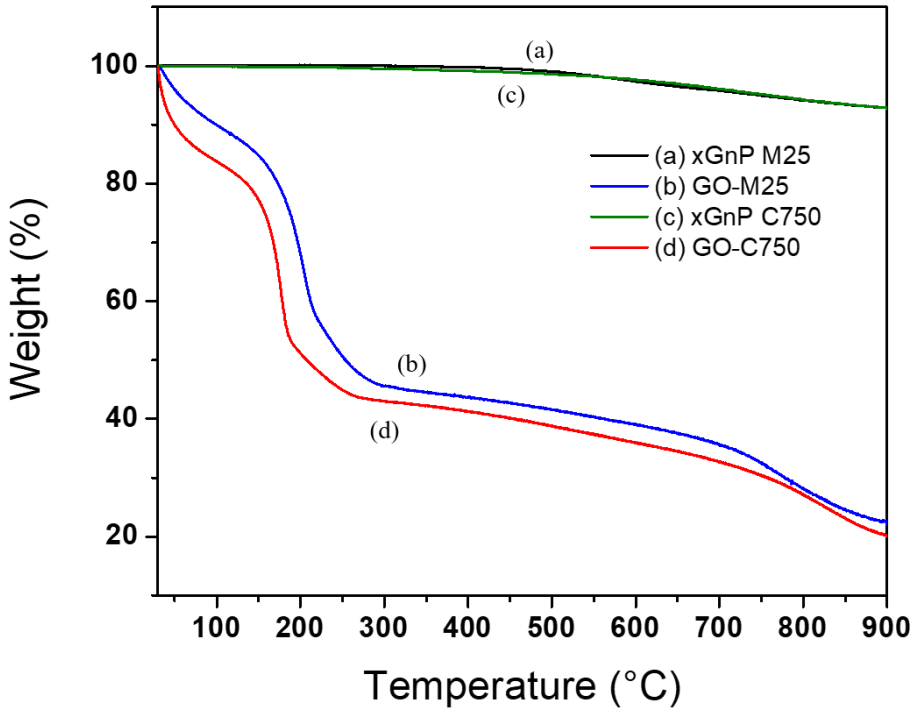

Figure A-3. TGA results of two different type of GnP and GO in N_2 atmosphere.

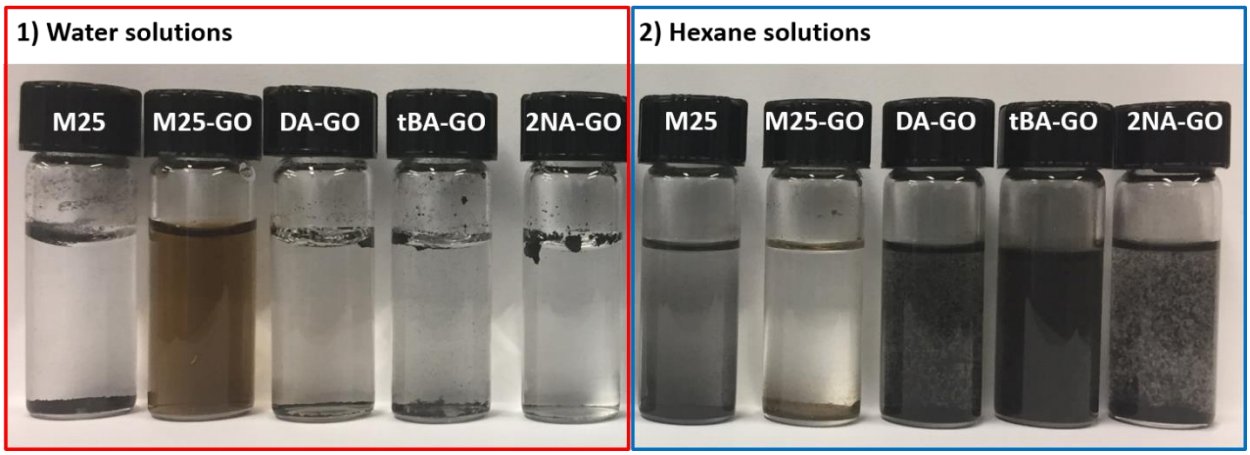

Figure A-4. Images for GnP, GO, and f-GO solution in water (1) and hexane (2) at 0.05 wt%.

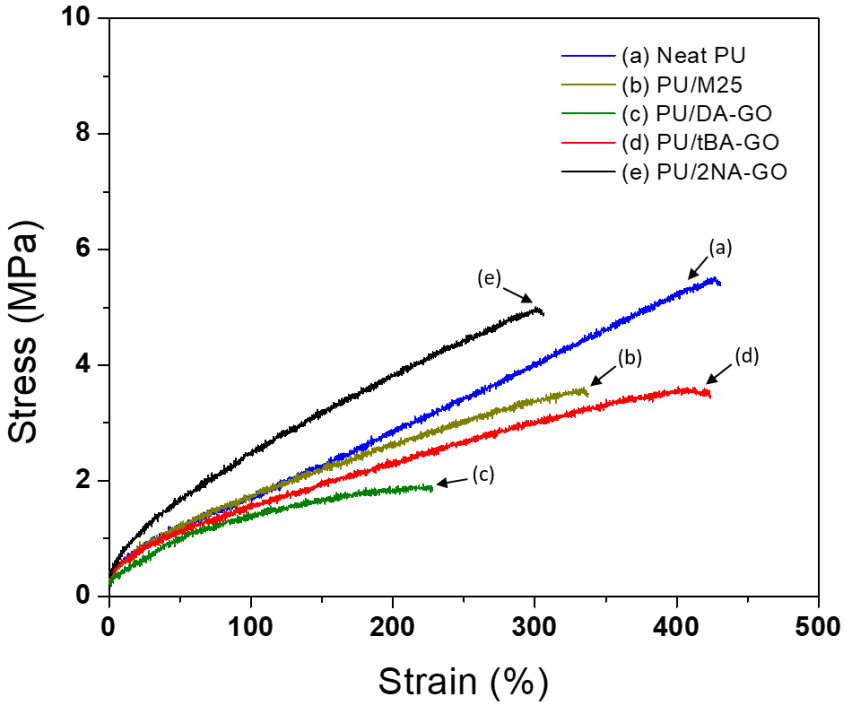

Figure A-5. Strain-Stress curve for (a) GnP, (b) GO, and f-GO; (c) DA-GO, (d) tBA-GO, and (e) 2NA-GO.